Spectral Radiative Properties of Cirrus Clouds Deduced from Interferometric Measurements

by
Gordon H. Beck and Stephen K. Cox

Department of Atmospheric Science
Colorado State University
Fort Collins, Colorado

Funding Agencies:
National Aeronautics and Space Administration (Grant NAG 1-1145)
Office of Naval Research (Contract No. N00014-91-J-1422)
Department of Energy (Contract No. DE-FG02-90ER60970)

Colorado
State
University

Department of
Atmospheric Science

Paper No. 562

SPECTRAL RADIATIVE PROPERTIES OF CIRRUS CLOUDS DEDUCED FROM INTERFEROMETRIC MEASUREMENTS

Gordon H. Beck and Stephen K. Cox

Department of Atmospheric Science
Colorado State University
Fort Collins, CO 80523

Research Supported By

National Aeronautics and Space Administration (Grant NAG 1-1146)
Office of Naval Research (Contract No. N00014-91-J-1422)
Department of Energy (Contract No. DE-FG02-90ER60970)

July, 1994

Atmospheric Science Paper No. 562

ABSTRACT

The infrared spectral window emittances of mid-latitude and sub-tropical cirrus clouds are inferred from surface-based interferometric measurements obtained during the FIRE II and ASTEX. The emittance values are derived at 1 cm^{-1} resolution over the 800 cm^{-1} to 1200 cm^{-1} bandpass. A nested iteration technique which includes cirrus cloud reflectance in the derivation of the cirrus emittances is described. The impact of including the reflectance properties of the cirrus layer in the inference of the emittances is shown to be significant.

For this set of observations, it is shown that the emittances of sub-tropical cirrus are generally higher than those of mid-latitude cirrus (0.006-0.749 as compared to 0.029-0.926, respectively). A comparison between the surface radiative forcings for the two classes of clouds showed that the absolute surface radiance changes due to the onset of cirrus were similar although the relative impact of the mid-latitude cirrus was larger than that of the sub-tropical cirrus. The roles of the subcloud layer and the layer above the cloud in modifying heating rates within the cirrus cloud layer and in the subcloud layer are examined.

ACKNOWLEDGEMENTS

Special thanks go to Dr. John M. Davis for his extensive guidance and both technical and emotional support. Melissa Tucker, Jane Wilkins, Paul Hein, Chris Cornwall and Dave Wood's help along the way is greatly appreciated.

Gordon Beck:

I would also like to thank my professors at Cayuga Community College in Auburn, New York and at SUNY at Oswego whose superior teaching skills and sincere caring helped to propel me into a top-notch graduate program. Also, all of my friends both here in Colorado and back home in New York who have helped to make the daily grind a bit easier.

I must give a very special thank you to my wife, Heather for her prayers and for putting up with me for the last three years and especially for her patience in the last year during which she put her own academic career on hold while I completed my course of study. I would also like to extend a special thank you to my parents who have always stood behind me and especially to my mother for her spiritual guidance throughout my formative years which laid a solid foundation for me to build upon. Finally, I would like to thank Heather's parents for their prayers and enthusiasm over the past few years.

This research was supported by the National Aeronautics and Space Administration under grant NAG-1-1146, the Office of Naval Research under contract No. N00014-91-J-1422, P00004, and the Department of Energy contract number DE-FG02-90ER60970.

TABLE OF CONTENTS

LIST OF FIGURES

LIST OF TABLES

1. INTRODUCTION

Radiative transfer accounts for virtually all of the energy exchange that occurs between the earth and the rest of the universe. Stephens and Webster (1979) showed that the accurate determination of the cirrus cloud properties was very important to the calculation of the net radiative fluxes at the boundaries of the atmosphere. According to Bretherton and Suomi (1983), cirrus clouds typically cover between 20% and 30% of the globe and show no preference to either latitude or time of day. Cirrus clouds are very good reflectors of incoming solar radiation and well as being good absorbers of outgoing terrestrial longwave radiation. This basic knowledge of the radiative properties of cirrus clouds along with the large areal extent points to the vital need for a quantification of cirrus cloud properties in the determination of radiation budgets and in global climate studies. The understanding of cirrus cloud properties is important in other scientific applications as well such as in remote sensing techniques and oceanic studies from satellites. Cirrus clouds may play a role in military and domestic systems such as in the passive detection of targets or air traffic hazards.

Because of the recent growing concerns about global climate change, there is now a much larger focus on cirrus cloud properties. The study of cirrus clouds was a major component of the FIRE (First ISCCP Regional Experiment) field operations during 1986 and 1987. The FIRE II field deployments of 1991 and 1992 had similiar objectives.

This study is concerned with the inference of infrared emittances of cirrus clouds which is considered to be an important parameter for climate modelling (Stephens 1984, Fu and Liou 1992). The emittance is the fraction of the blackbody radiance (determined by the object's given temperature) that an object actually emits. A blackbody radiator is an object which absorbs all incident radiation and emits the maximum possible radiation at every wavelength at its given temperature. In simplest terms, the emittance states the efficiency at which an object absorbs and emits radiation.

For this study, two main techniques are developed for inferring the infrared emittance of cirrus layers from surface-based interferometer measurements. The first technique is called the observational technique and requires interferometric clear sky and cirrus sky spectra, lidar or radar returns and radiosonde data.

The second method is called the semi-empirical technique. This method requires spectral radiance calculations, cirrus sky and clear sky interferometer spectra, lidar or radar returns and radiosonde data. The interferometer measurements indicate the effect of the cirrus cloud layer on the surface measurements of infrared radiation in the atmospheric window from 800 cm^{-1} to 1200 cm^{-1}. The radiances were calculated using FASCODE III which is a line-by-line radiance/transmittance model developed at the Air Force Geophysics Laboratory and is used to calculate atmospheric layer radiances for a clear sky. The lidar or radar returns are used to locate the cloud height and thickness and the sounding data are used to determine cloud layer temperatures and, for the semi-empirical technique, are also used in initializing the FASCODE model.

The importance of including the effects of reflection for the inference of cirrus cloud properties has been discussed in previous literature. Stephens (1980) stated that although the reflectance is small, the reflected radiance is large accounting for 25% of the total flux at cloud base in calculations which simulated cloud particles as cylinders, and 15% for spheres. Most of the cirrus radiative studies which have inferred emittances, however, have tended to ignore the contribution of the reflected radiance leaving a cirrus layer. This study includes reflectance for the inference of cirrus layer properties. Also, the inferred emittances and transmittances presented in this study are calculated independent of one another unlike most previous studies which simply infer one cirrus cloud property and then subtract its value from 100% to obtain a value for the other property. The inclusion of reflectance made the independent calculation of emittance and transmittance a necessary requirement for inferring cirrus cloud properties.

Data collected during the FIRE II project at the Parsons, Kansas site in November and December of 1991 and at the Porto Santo, Madeira site in the eastern Atlantic ocean in June of 1992 are used for this study. Interferometer, radiosonde and either lidar or radar data were taken throughout these events. Lidar data are used to determine cloud heights for the Parsons, Kansas cases; radar data are used for the Porto Santo cases. The details of the interferometric measurement techniques may be found in Appendix A.

2. TECHNIQUES FOR INFERRING RADIATIVE PROPERTIES OF CIRRUS

Two techniques were developed to infer the radiative properties of cirrus layers. One method relies exclusively upon observed data and is referred to as the observational technique. The second method utilizes a combination of observed data and a radiation transfer model and is referred to as the semi-empirical technique. The two methods are described in this section.

2.1. The observational technique and the 3 layer model

If one were to divide the atmosphere into 3 layers (see figure 2.1), the equations for the cirrus sky radiance and the clear sky radiance respectively, may be written as follows:

$$N_{meascld} = N_l + N_{cld}T_l + N_u T_{cld} T_l \tag{2.1}$$

$$N_{measclr} = N_l + N_{clr}T_l + N_u T_{clr} T_l, \tag{2.2}$$

where $N_{meascld}$: the measured spectral radiance at the surface with the cirrus present
$N_{measclr}$: the measured spectral radiance at the surface under clear sky conditions
N_l : the radiance from the atmospheric layer below the cirrus layer
T_l : the transmittance of the atmospheric layer below the cirrus layer
N_{cld} : the radiance from the cirrus layer with the cloud present
N_{clr} : the radiance from the cirrus layer if it were clear
T_{cld} : the transmittance from the cirrus layer with the cloud present
T_{clr} : the transmittance from the cirrus layer if it were clear
N_u : the radiance from the atmosphere above the cirrus layer

These layer radiances are what the interferometer would see by looking upward into the layer

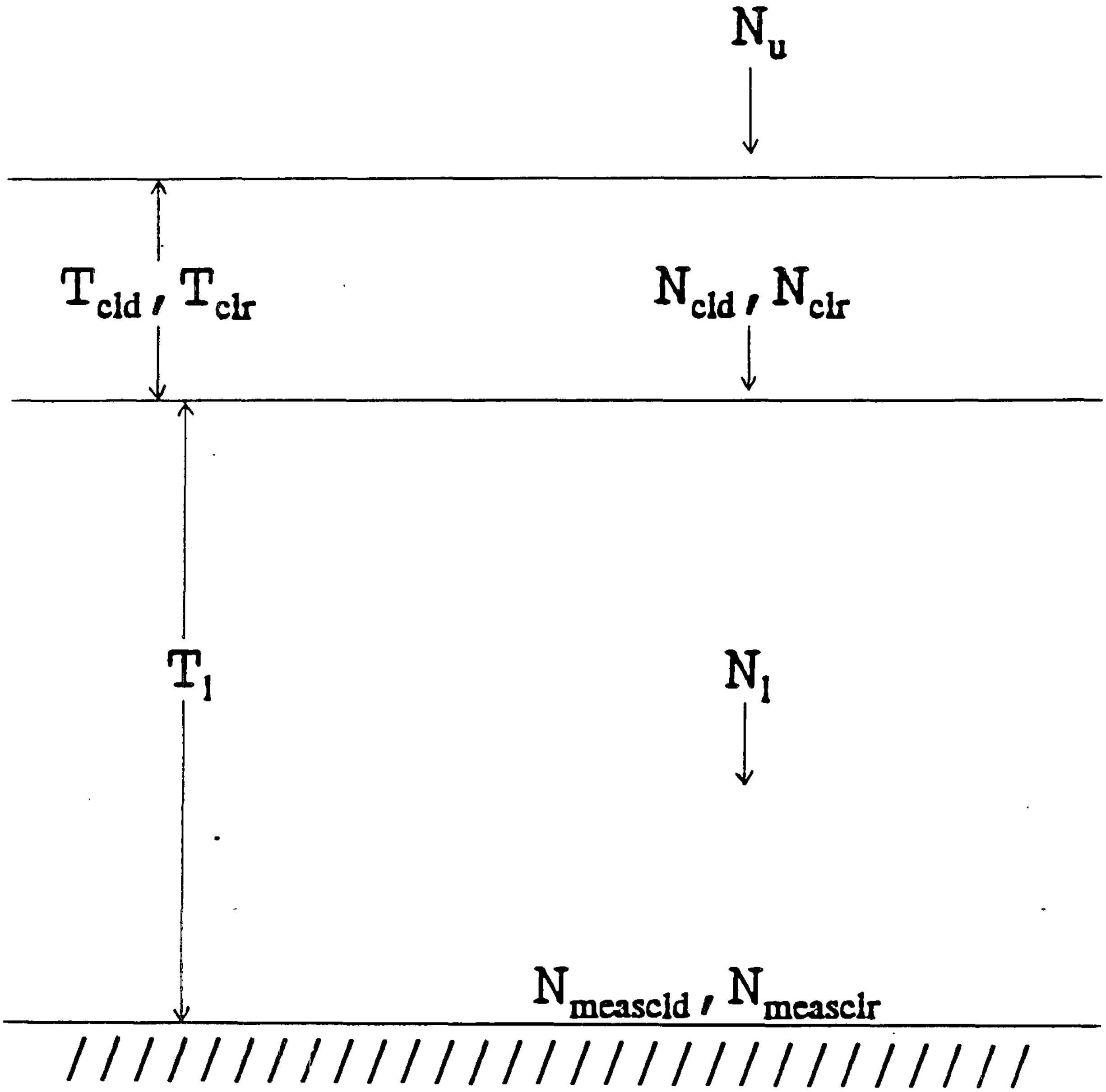

Figure 2.1. The three layer model.

from its lower boundary with no effects from outside of the respective layer.

In the observational technique, there are two possible scenarios for the acquisition of the measured data. An interferometric clear sky spectrum, $N_{measclr}$, obtained just before the onset of the cirrus could be used with the spectrum obtained with the cirrus shield overhead, $N_{meascld}$, or a clear sky spectrum acquired following the retreat of a cirrus shield could be used in conjunction with the cirrus sky spectrum taken previously.

An effective radiance from the cirrus cloud is found by a simple spectral differencing, i.e. the clear sky radiance is subtracted from the cirrus sky radiance at each wavenumber. Subtracting equation (2.2) from equation (2.1) to obtain the effective downward radiance from the cirrus cloud gives a more intuitive understanding of what actually causes the difference between the two spectra. This result is shown in equation (2.3):

$$N_{eff} = N_{meascld} - N_{measclr} = [(N_{cld} - N_{clr}) - N_u (T_{clr} - T_{cld})] T_l . \tag{2.3}$$

The effective downward radiance N_{eff} is the composite of two terms multiplied by the transmittance (T_l) of the sub-cloud layer. The (N_{cld}-N_{clr}) term represents the actual increase which would occur in the downward radiance from the cirrus layer itself as the sky cover changed from clear to cloudy. The $N_u(T_{clr}-T_{cld})$ term represents the decrease in the downward radiance (N_u) from the layer above the cirrus layer. This decrease in the downward radiance is due to the decrease in the transmittance of the cirrus layer as the sky cover changed from clear to cloudy, again, as seen from the base of the cloud layer. Finally, the increase in the downward radiance from cirrus layer and the decrease in the downward radiance from the layer above the cirrus layer as seen from the lower boundary of the cirrus layer are multiplied by the transmittance of the sub-cloud layer (T_l) yielding the decrease in downward radiance that is seen at the surface.

An effective emittance may be defined where B_{cld} is the Planck function of the cirrus layer temperature. The cloud base temperature was determined from sounding using either lidar or radar data to determine the height of the cloud boundaries.

$$E_{eff} = \frac{N_{eff}}{B_{cld}} \qquad (2.4)$$

Note the effective emittance (E_{eff}) implicitly contains the effects of reflection by the cirrus layer and therefore is greater than the true emittance.

2.2. The semi-empirical technique

The semi-empirical technique requires FASCODE III calculations, cirrus sky and clear sky interferometer spectra, lidar or radar returns and radiosonde data. The effects of scattering were ignored for the FASCODE calculations. The scattering of IR radiation by air molecules is negligible although the scattering caused by aerosols falls into the Rayleigh regime and for cloud droplets or ice crystals it enters the Mie regime. However, the absorption and emission by these larger particles is far more significant than any effect of scattering.

This technique can accommodate the effects of the reflection from the cloud of the radiation emitted by both the surface and the sub-cirrus atmospheric layer. The method described here relies far less upon FASCODE calculations than other methods such as the one used by Smith (1993) where the measurements are "adjusted" to better correspond to model calculations. For this study, the FASCODE calculations are used merely to normalize the measured spectra.

2.2.1. Derivation

The two 3-layer model equations for the cirrus sky and clear sky (see the 3-layer model diagram) are now written as:

$$N_{measclr} = N_l + N_{clr}T_l + N_u T_{clr} T_l \tag{2.5}$$

$$N_{meascld} = N_l + N_{cldlayer}T_l + N_u T_{cld} T_l, \tag{2.6}$$

where $N_{cldlayer}$ is the *total* radiance seen coming from the cirrus layer and is defined as:

$$N_{cldlayer} = N_{cld} + F_{cld}. \tag{2.7}$$

N_{cld} is the emitted radiance from the layer and F_{cld} is the upwelling radiance that is reflected by the layer. Again, these layer radiances are what the interferometer would see by looking upward into the layer from its lower boundary with no effects from outside of the respective layer.

By subtracting equation (2.6) from equation (2.5) we obtain:

$$N_{meascld} = N_{measclr} + (N_{cldlayer} - N_{clr})\,T_l + N_u(T_{cld} - T_{clr})\,T_l. \qquad (2.8)$$

Note that the radiance of the entire atmospheric layer below the cirrus cloud has dropped out of the equation. Of course, this assumes that the radiance from the sub-cirrus layer is the same during both measurements although it may change from the time at which the first measurement was made to the time of the second measurement. A normalization is made in the following equations via FASCODE to attempt to compensate for this change.

Cirrus clouds are high, cold and usually optically thin. In the most transparent regions of the infrared spectrum (which is the only part that we are concerned with here), the gaseous emission from a clear atmospheric layer with these characteristic temperatures and thicknesses is 2 to 3 orders of magnitude less than if there were a cirrus cloud in the same location. This can be seen from the results of FASCODE calculations which are shown in table 2.1. Listed in the three columns are the 800 cm^{-1} to 1200 cm^{-1} integrated layer radiances for the sub-cloud layer, and for the cloud layer and the layer above the cloud layer following transmission to the surface, respectively; calculated for *clear sky* conditions (no cloud in the cloud layer). The layer boundaries are given for each data set along with the location and the date and time.

The test results in table 2.1 show the clear sky emission to be almost totally dominated by the lowest 5 to 6 km. The radiance from the cloud layer if no cloud were present only accounted for 0.7% to 0.8% of the total radiance arriving at the surface. On this basis we

	radiance $[Wm^{-2}sr^{-1}]$		
	subcloud	cloud	abovecld
Parsons 11/26/91 2030Z	4.274	.032	.025
cloud layer: 5.5-9.8 km	98.7%	0.7%	0.6%
Porto Santo 6/23/92 1250Z	7.701	.127	.063
cloud layer: 6.0-9.0 km	98.8%	0.8%	0.4%

Table 2.1. Results of FASCODE III radiance calculations for the cirrus cloud layer and the layers above and below the cirrus layer from one Parsons sounding and one Porto Santo sounding.

ignore this emission. Equation (2.8) can now be written with $N_{clr}=0$ as:

$$N_{meascld} = N_{measclr} + N_{cldlayer}T_l + N_u(T_{cld}-T_{clr})\,T_l. \tag{2.9}$$

The same argument also holds true for the $[N_u(T_{cld}-T_{clr})T_l]$ term which has values which are 2 to 3 orders of magnitude smaller than the other terms in the equation (see table 2.1). Its inclusion would involve further FASCODE calculations which might result in more error than if it were ignored completely. The obvious exception is the ozone absorption region, but, again, we are only concerned with the most transparent regions of the window since these areas contain the most information about the cirrus cloud layer. Re-writing equation (2.9) with the stated assumption yields equation (2.10):

$$N_{meascld} = N_{measclr} + N_{cldlayer}T_l. \tag{2.10}$$

This equation requires both the cirrus sky and clear sky measurements and only one FASCODE calculation (T_l). It does, however, have two major problems. This equation was derived under the assumption that the sub-cirrus atmospheric layer radiance was the same at the times which both measurements were made. The other major problem is that there tend to be large discrepancies between the interferometric radiance measurements and the FASCODE calculations of radiance. Given this fact, one may conclude that the FASCODE calculations of transmittance values would also differ from those found with the inteferometer if the instrument were able to measure transmittance directly.

First, a normalization to the measured clear sky spectrum was made in an attempt to compensate for the change in both the temperature and water vapor profiles in the sub-cirrus layer of the atmosphere. Comparisons between model runs and measurements have shown that there was a direct correlation between the magnitude of the emitted radiance of the clear spectra and the magnitude of the difference between the interferometer measurements and the FASCODE measurements. That is, the larger the atmospheric clear sky radiance values, the larger the difference between the instrument and the model.

Figure 2.2 shows the 800 cm^{-1} to 1200 cm^{-1} integrated differences between the measured clear sky radiances and the FASCODE calculated radiances versus the magnitude of the integrated measured clear sky radiances. Previous studies such as Smith, et al. (1987,1988), Smith, et al. (1993) and Revercomb, et al. (1989) have dealt with this discrepancy between radiometric measurements and FASCODE calculations using various methods. For this study, a linear relation was assumed and so the measured clear sky radiances were normalized using equation (2.11).

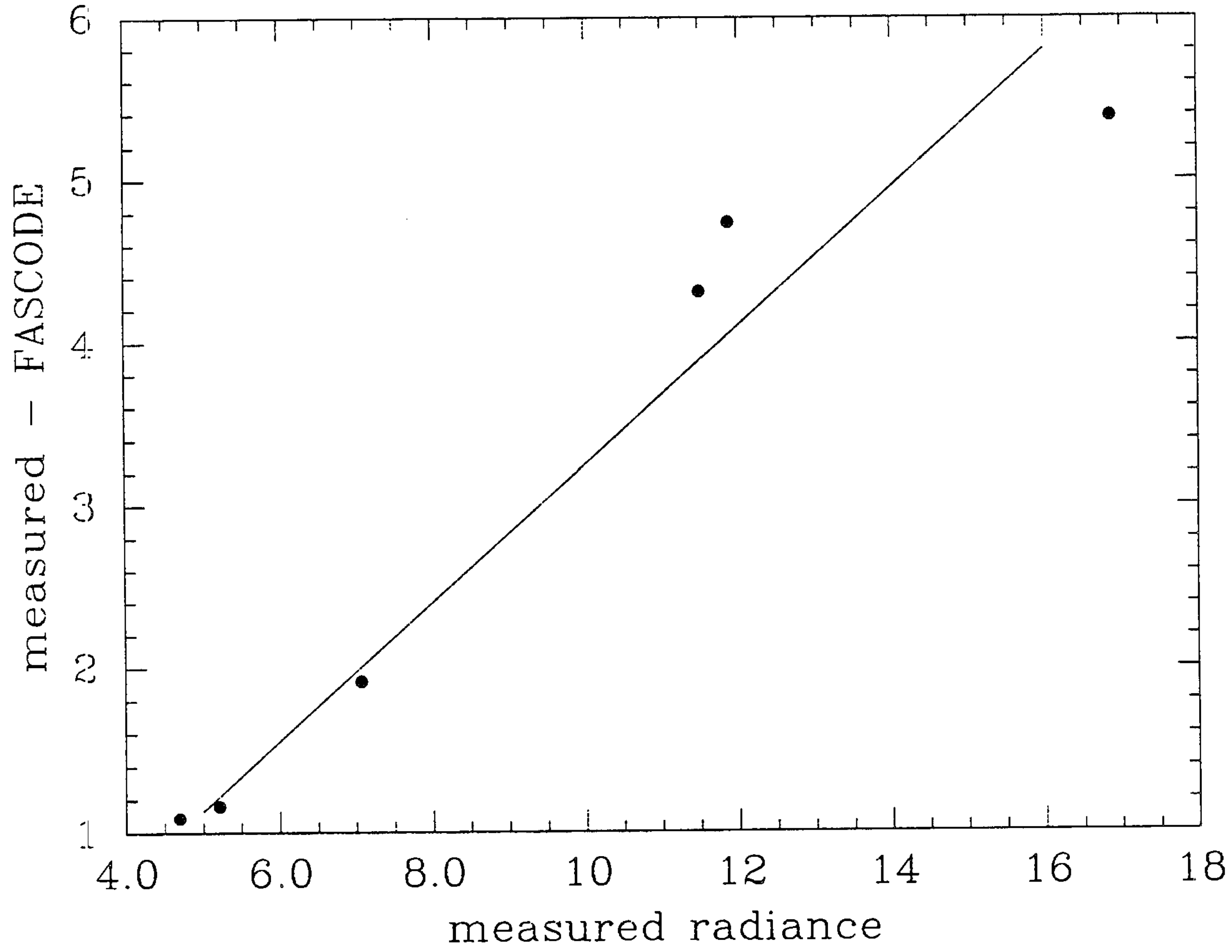

Figure 2.2. The 800 cm-1 to 1200 cm-1 integrated radiance difference between the interferometer measurements and FASCODE calculations versus the integrated measured radiance.

$$N_{adjmeasclr} = N_{measclr}\left(\frac{N_{calccld}}{N_{calcclr}}\right) \tag{2.11}$$

$N_{calccld}$ is total atmospheric downwelling radiance calculated by FASCODE using data from a sounding launched near the time of the cirrus measurement and $N_{calcclr}$ is total atmospheric downwelling radiance calculated by FASCODE using data from a sounding launched near the time of the clear sky measurement. Note that the values calculated from FASCODE are in ratio form which effectively removes the discrepancy between FASCODE and the measurements. $N_{adjmeasclr}$ is the radiance the interferometer would have measured with the temperature and water vapor profiles present at the time of the cirrus sky measurement, if the sky were clear. This normalization, in effect, compensates for the effects of changes in the sub-cirrus layer temperature and water vapor profiles that occurred during the time interval between the clear sky and the cirrus sky measurements. This normalization is made in order to be consistent with the constant N_l assumption that was used in deriving equation (2.8). Rewriting equation (2.10) as a function of $N_{adjmeasclr}$:

$$N_{meascld} = N_{adjmeasclr} + N_{cldlayer}T_l. \tag{2.12}$$

Next we need to determine T_l, noting that the disagreement between FASCODE and the interferometer may be quite large.

For the sub-cirrus atmospheric layer, the following expression may be written:

$$N_l = B_{effl}(1-T_l) \,. \qquad (2.13)$$

B_{effl} is the Planck function evaluated at an equivalent radiating temperature for the sub-cirrus layer as a whole.

From table 2.1, we learned that more than 98% of the clear sky radiance incident at the surface comes from the atmospheric layer beneath the cirrus cloud layer. If we assume that the entire discrepancy between radiance values from FASCODE calculations and the interferometer measurements comes from the sub-cirrus layer, then the following normalization can be made to the calculated radiance of the sub-cirrus layer, N_{calcl}, by employing the ratio equality given in equations (2.11) and (2.13):

$$N_{adjl} = N_{adjmeasclr}\left(\frac{N_{calcl}}{N_{calccld}}\right) . \qquad (2.14)$$

Note that the FASCODE calculated values are in ratio form once again in an attempt to minimize the effects of model versus measurement differences.

Using the definition above for N_{adjl}, equation (2.13) may now be rewritten as:

$$T_l = 1 - \left(\frac{N_{adjl}}{B_{effl}}\right) . \qquad (2.15)$$

A simple iterative technique presented by Ackerman (1990), may be applied to the sub-cloud layer to determine T_l and B_{effl} for downwelling radiation. This iterative scheme assumes that the emission is linear in optical depth throughout the layer. With this assumption, the integrated Planck radiance for the sub-cirrus atmospheric layer can be expressed as follows:

$$\int_{sfc}^{cldbase} B_l(z)\,\frac{dT}{dz}dz = B_{sfc} - B_{cldbase}T_l + \frac{(T_l - 1)\,(B_{cldbase} - B_{sfc})}{\ln(T_l)}. \qquad (2.16)$$

T_l is found from equation (2.15) and the values for the cloudbase temperature and surface temperature Planck functions, $B_{cldbase}$ and B_{sfc}, respectively, are calculated using rawinsonde and lidar or radar data. A mean Planck radiance value for the sub-cirrus atmospheric layer may be found with the help of the mean value theorem. This is expressed as:

$$B_{effl} = \frac{\int_{sfc}^{cldbase} B_l(z)\,\frac{dT}{dz}dz}{(1 - T_l)}. \qquad (2.17)$$

Now, with an initial input value for B_{effl} taken from the relation $B_{effl} = N_{calcl}/(1 - T_{calcl})$, the iterative process to determine the value of T_l can begin.

Finally, in order to determine the magnitude of the reflected radiation from a cirrus layer, we need to know a value for the upwelling radiation which is incident upon the cirrus layer. The variable $N_{adjupwardl}$ represents the upwelling radiance which is emitted from both the sub-cirrus layer and the surface. It is a normalized value which is found from the following equation.

$$N_{adjupwardl} = N_{adjmeasclr} \left(\frac{N_{calcupwardl}}{N_{calccld}} \right) \qquad (2.18)$$

The value for $N_{calcupwardl}$ is calculated from FASCODE and is then normalized in a manner nearly identical to that made on the sub-cirrus layer radiance (see equation (2.14) for comparison).

Equation (2.12) is the crux of the semi-empirical technique. From this equation, $N_{meascld}$ is determined by a measurement, and it was shown in this section how the values for $N_{adjmeasclr}$ and T_l were determined. This leaves one unknown, $N_{cldlayer}$. As defined by equation (2.7), it includes both the radiation which is emitted by the cirrus cloud and that which is reflected by the layer. The components of this variable must be found via an iterative process due to the fact that we have one equation and two unknowns which, in turn, are dependent upon three more unknowns, i.e., the transmittance, emittance and the reflectance of the cirrus cloud layer. The method used for determining all of these unknowns is outlined in the following section.

2.2.2. The nested iteration scheme

The complete solution for the cirrus cloud emittance involves two iteration schemes which are nested. The first iterative set is an extension of the work by Ackerman (1990) which determines the transmittance of the cirrus cloud layer and the effective Planck radiance. The second iterative set of equations determines the emittance and the reflectance of the cirrus cloud layer and also determines the values for both the emitted and the reflected radiances. Each set iterates until the change in the values for the solutions becomes very small. There is an iterative step between the two sets of equations. Thus the process may be thought of as nested iterative equation sets.

The first iterative set contains the following equations:

$$T_{cld} = 1 - R_{cld} - \frac{\left(\frac{N_{meascld} - N_{adjmeasclr}}{T_l}\right) - F_{cld}}{B_{cld}} \qquad \text{(a)}$$

$$\int_{cldtop}^{cldbase} B_{cld}(z) \frac{dT}{dz} dz = B_{cldbase} - B_{cldtop} T_{cld} + \frac{(T_{cld} - 1)\,(B_{cldtop} - B_{cldbase})}{\ln T_{cld}} \qquad \text{(b)}$$

$$B_{cld} = \frac{\int_{cldtop}^{cldbase} B_{cld}(z) \frac{dT}{dz} dz}{(1 - T_{cld})} . \qquad \text{(c)}$$

Here, the values for $N_{meascld}$, $N_{adjmeasclr}$, and T_l for equation (a) and values for $B_{cldbase}$ and B_{cldtop} for equation (b) have already been found.

To begin the iterative process, the values for F_{cld} and R_{cld} are initially assumed to be zero and an initial value for B_{cld} is assumed to be equal to the average of the values for $B_{cldbase}$ and B_{cldtop}. Values for R_{cld} and F_{cld} are later passed back into this set after working through the second iterative set outlined below. T_{cld} is calculated and then a new value for B_{cld} is determined which is then passed back into the first equation. After the solutions converge, the value of B_{cld} is then passed to the second iterative set which contains the following equations:

$$N_{cld} = N_{cldlayer} - F_{cld} \tag{d}$$

$$E_{cld} = \frac{N_{cld}}{B_{cld}} \tag{e}$$

$$R_{cld} = \frac{E_{cld}}{m\,E_{cld} + b} \tag{f}$$

$$F_{cld} = R_{cld}\,N_{adjupwardl}\,. \tag{g}$$

For this second equation set, only the values for $N_{cldlayer}$ and $N_{adjupwardl}$ are known.

The initialization of the second iterative set requires a value for B_{cld}, which was determined by the first iterative set, and a value of F_{cld} which is assumed to be zero. After finding a value for N_{cld} in equation (d), E_{cld} is found in equation (e) using the value for B_{cld} that was passed to this iterative set from the first set. From a study by Yamamoto (1970), R_{cld} is empirically related to E_{cld} in equation (f) and is used in the calculation of F_{cld} in equation (g). Now, there is a calculated value for F_{cld} which is then passed back into the first equation (d).

After these equations merge, a new value for R_{cld} is then passed to the first iterative set outlined above where a new value for B_{cld} is again found. These two values are passed back and forth between the two iterative sets until the solutions to all of the equations merge. See Appendix B for a more detailed description.

3. SENSITIVITY TESTS

The techniques derived for inferring the spectral emittance of cirrus clouds contain a number of assumptions. This chapter is devoted to an assessment of the impact of these assumptions. Specifically, the effects of reflectance, sub-cloud layer extinction and emission, and a normalization of the measurements using model results are explored. The values presented both here and in the following chapter result from the analysis of six cirrus events during the field deployment phase of the FIRE II project. There are three cases from the Parsons, Kansas data set acquired during November and December of 1991 and three from the Porto Santo data set taken during the June 1992 field deployment. For simplicity, the cases have been numbered as Parsons1, 2 and 3 and Portsan1, 2 and 3.

When examining the data presented here and in the following chapter, the 975 cm-1 to 1075 cm-1 ozone absorption band should be ignored and it is demarcated on all of the spectral plots. All of the integrated values presented in the tables are calculated in the following manner. The range of integration extends from 800 cm^{-1} to 1200 cm^{-1}. The area of strong ozone emission from 975 cm^{-1} to 1075 cm^{-1} is not included because of its large variability in the lower troposphere and also because of the fact that the atmospheric layer above the cirrus layer where O_3 emission is important was not included in the calculations for the semi-empirical technique. Secondly, the highest and the lowest 5% of the remaining values are not counted towards the integrated values. This helps to reduce the effects of noise caused by some of the less transparent wavenumbers in the window. These omissions leave a total of 270 wavenumbers that are included in a given integration. This value is then multiplied by 400/270 to obtain the filtered 800 cm^{-1} to 1200 cm^{-1} integrated values which are found in all the integration tables which follow. This method of integrating the data results in more meaningful values for use in comparative analysis.

3.1. Reflectance by the cirrus layer

This section will demonstrate how important it is to include the reflectance of longwave radiation in the calculation of cirrus cloud properties. Feigel'son (1970) noted that reflectance can cause the amount of downwelling infrared radiation to actually be greater than the amount of radiation that would be emitted by a blackbody at the cloud temperature. This may occur when a cirrus cloud layer is very highly emissive (near black) since the temperature at which cirrus clouds emit radiation is usually much colder than the radiating temperature of the reflected surface radiance.

There are six examples of spectra that are used in this chapter (see Appendix C for a complete listing). The vertical extent of the cirrus layer, the cloudbase and cloudtop temperatures (in K) and the surface temperatures are listed in table 3.1.

The following figures show the differences in the calculated radiances and emittance spectra between when reflection is and is not included in the calculation of the cirrus emission. Shown are one low emittance case and for one high emittance case from the Parsons data set. The differences in the derived cirrus layer radiances as seen from the bottom of the cirrus layer are shown in figures 3.1a and b.

The deduced cirrus emission decreased in every case, as expected, when the reflected

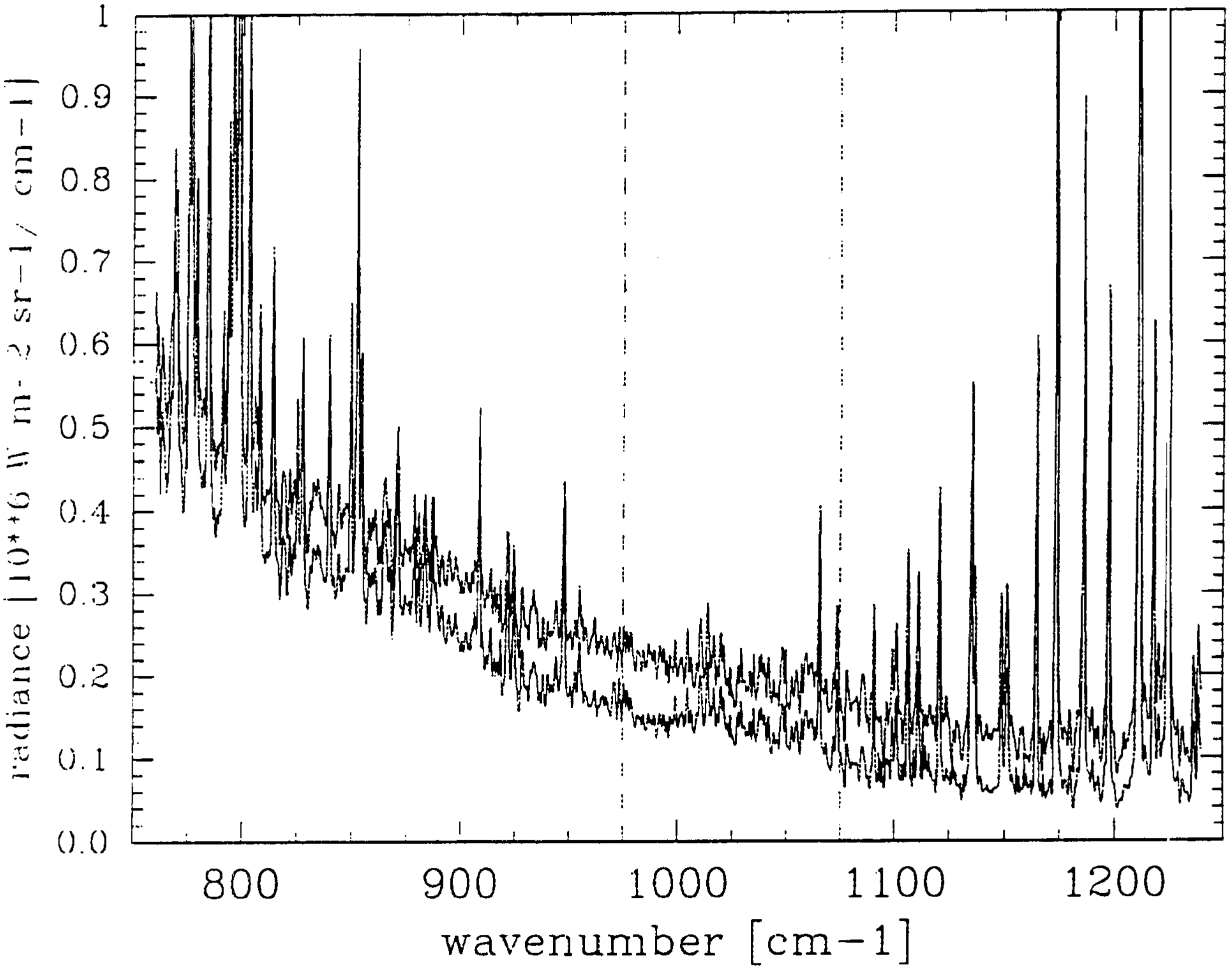

Figure 3.1a. Comparison between the derived cirrus layer emitted radiances for the Parsons1 #60 spectrum ignoring reflectance (upper curve) and with reflectance included in the calculations (lower curve).

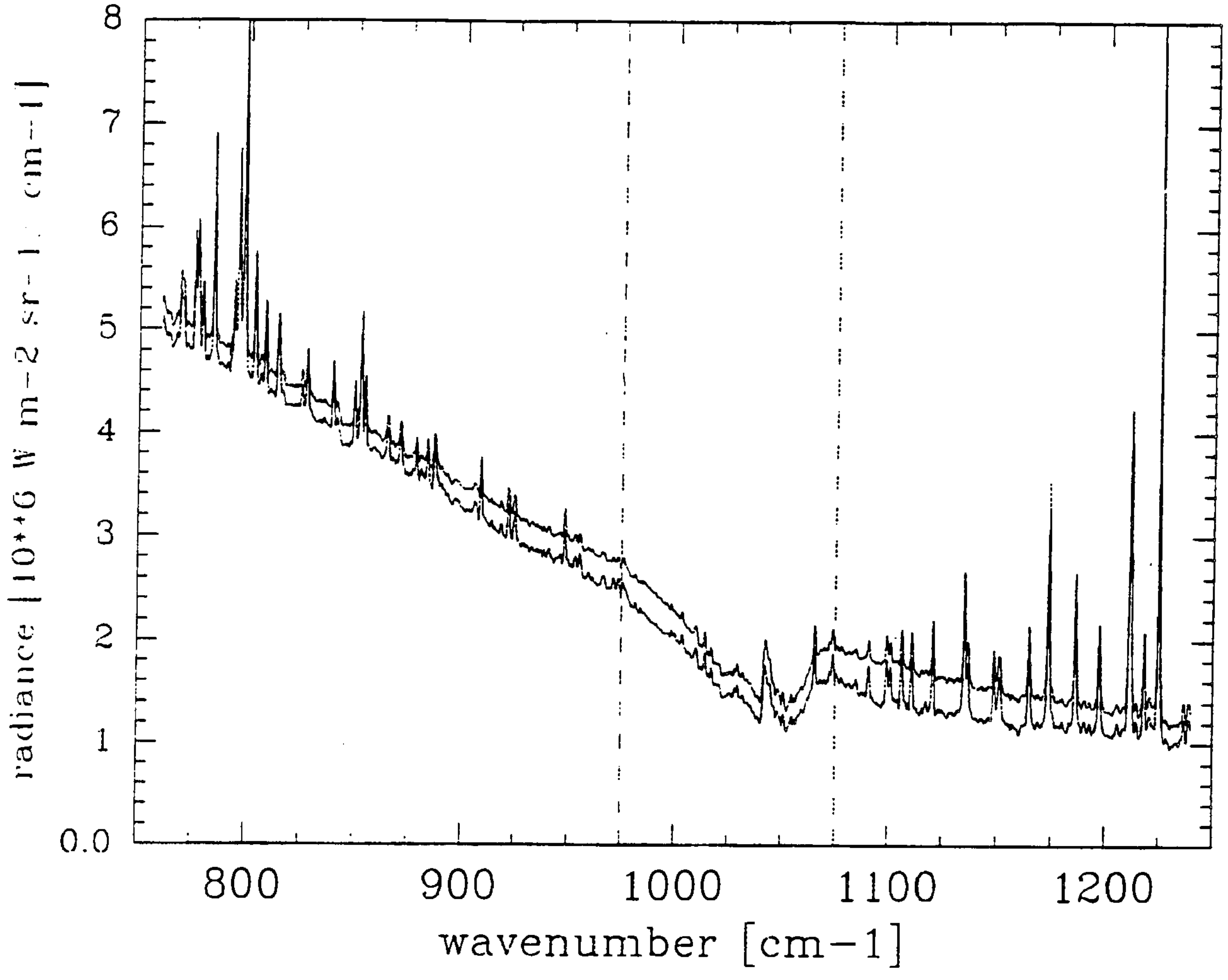

Figure 3.1b. Comparison between the derived cirrus layer emitted radiances for the Parsons2 #06 spectrum ignoring reflectance (upper curve) and with reflectance included in the calculations (lower curve).

	layer hgt[km]	cldbase	cldtop	surface
Parsons1 Nov 22 #30	9.0-10.0	232	224	286
Parsons1 Nov 22 #60	8.0-10.0	240	223	283
Parsons2 Nov 26 #06	5.8-9.0	251	225	286
Portsan2 Jun 23 #39	6.0-9.0	257	236	290
Portsan2 Jun 23 #75	8.0-8.3	243	242	292
Portsan3 Jun 27 #45	7.5-9.5	253	237	295

Table 3.1. Data from six cirrus events used for this study.

radiance was taken into account. The slope of the cirrus emission from 760 cm^{-1} to 975 cm^{-1} became slightly larger while the slope decreased from 1075 cm^{-1} to 1240 cm^{-1}. With the decrease in the derived cirrus emission, the corresponding derived emittance values also must decrease. Figures 3.2a and b show the emittances associated with the above spectra. Because of the relationship of the reflectance to the emittance, the larger the emission value, the larger was the influence of the inclusion of reflectance in the calculation of the cirrus emission, especially in the higher wavenumber region of the atmospheric window.

Table 3.2 shows a comparison between the integrated values of the spectra shown in

	emit	tran	refl
Parsons1 #60	.072	.922	.007
	.102	.898	ignored
Parsons2 #06	.749	.227	.024
	.823	.177	ignored

Table 3.2. Emittance and transmittance values found for two cirrus cases with and without reflection included.

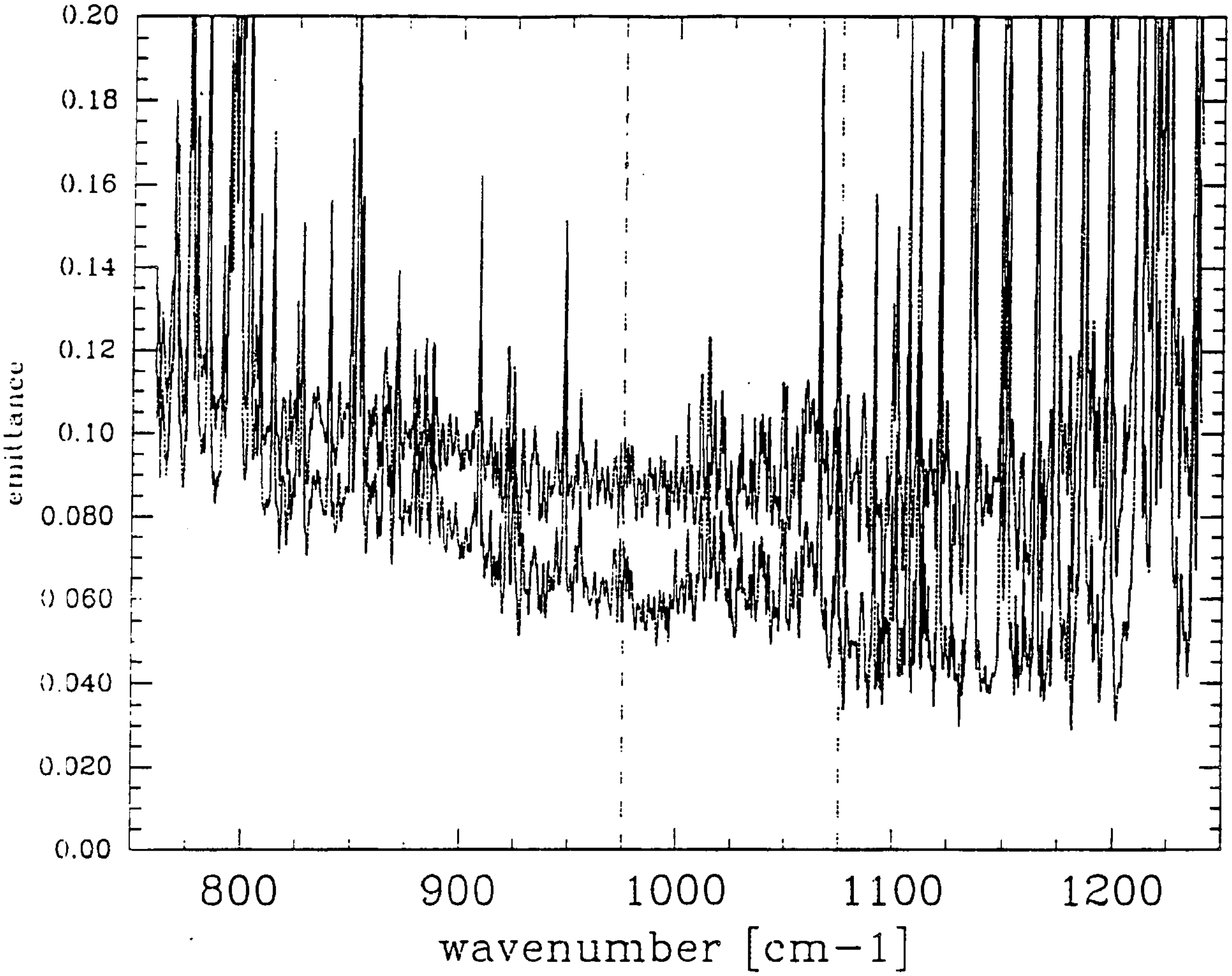

Figure 3.2a. Comparison between the derived cirrus layer emittances for the Parsons1 #60 spectrum ignoring reflectance (upper curve) and with reflectance included in the calculations (lower curve).

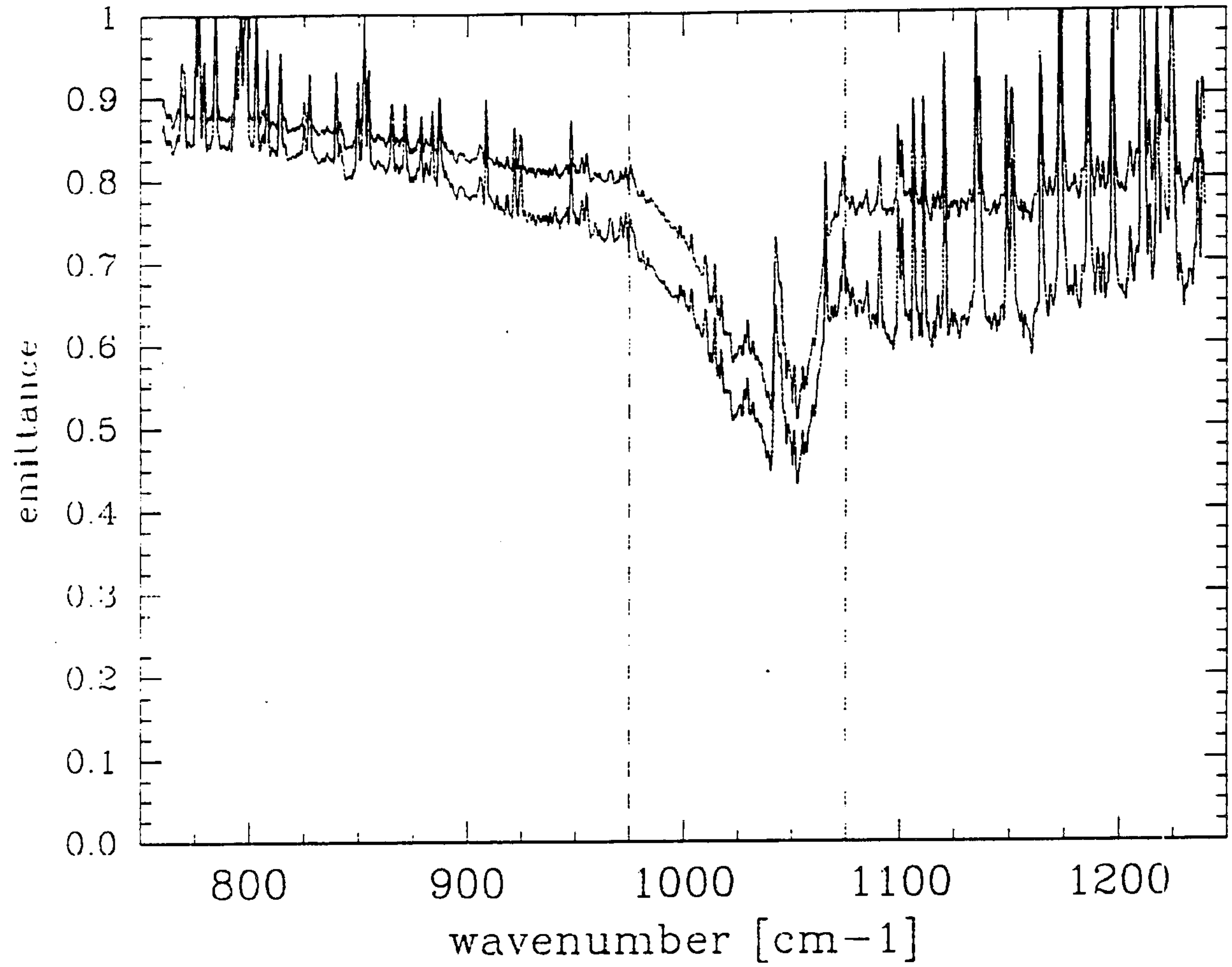

Figure 3.2b. Comparison between the derived cirrus layer emittances for the Parsons2 #06 spectrum ignoring reflectance (upper curve) and with reflectance included in the calculations (lower curve).

figures 3.1 and 3.2 for when reflection is included in the calculations of the cirrus layer parameters and for when it is not included.

The changes in the emittance and transmittance values shown above occur with the inclusion of reflection because only a small reflectance results in a large amount of reflected radiance since there is a large temperature difference between the surface and the cirrus layer. When this is properly accounted for, the value for the emittance decreases significantly since the cirrus is emitting at a much colder temperature than the surface and underlying atmosphere and thus the values generated for the transmittance will increase. The inclusion of reflectance in the diagnosis of cirrus parameters has a large impact upon the value for the deduced emittance as well as the value for the emitted radiance. Knowledge of the cloud reflectance is most important when considering the magnitude of the cloud layer emission in the tropics and the sub-tropics where more incoming solar radiation received on an annual basis and the surface temperatures are the highest.

The spectra in figures 3.3a and b correspond to those shown in figures 3.1a and b from the Parsons data set. Each shows both the emitted radiance and the reflected radiance from the cirrus layer as seen from the bottom of the layer. These further demonstrate the importance of accounting for the reflected radiance when observing cirrus clouds.

The region of the window around 1100 cm^{-1} consistently showed the highest values of reflected radiance throughout all of the cases while the 760 cm^{-1} to 850 cm^{-1} region consistently yielded the smallest spectral values. For the low emittance case in figure 3.3a, the importance of reflected radiation is very apparent. The values of the reflected radiance divided by the emitted radiance for the low emittance spectrum vary spectrally from around 20% near 800 cm^{-1}

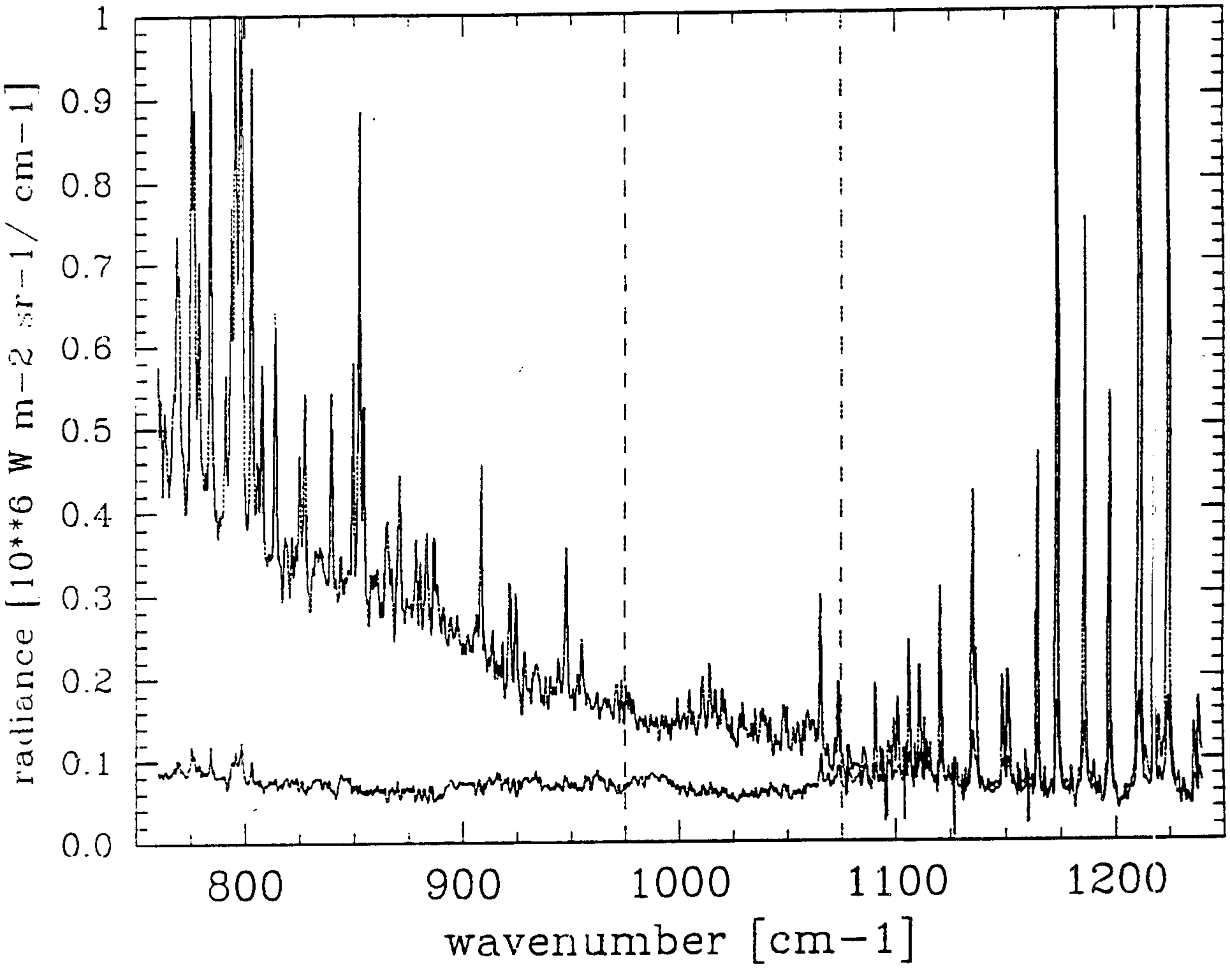

Figure 3.3a. The cirrus layer emitted radiance (upper curve) and reflected radiance (lower curve) for the Parsons1 #60 spectrum.

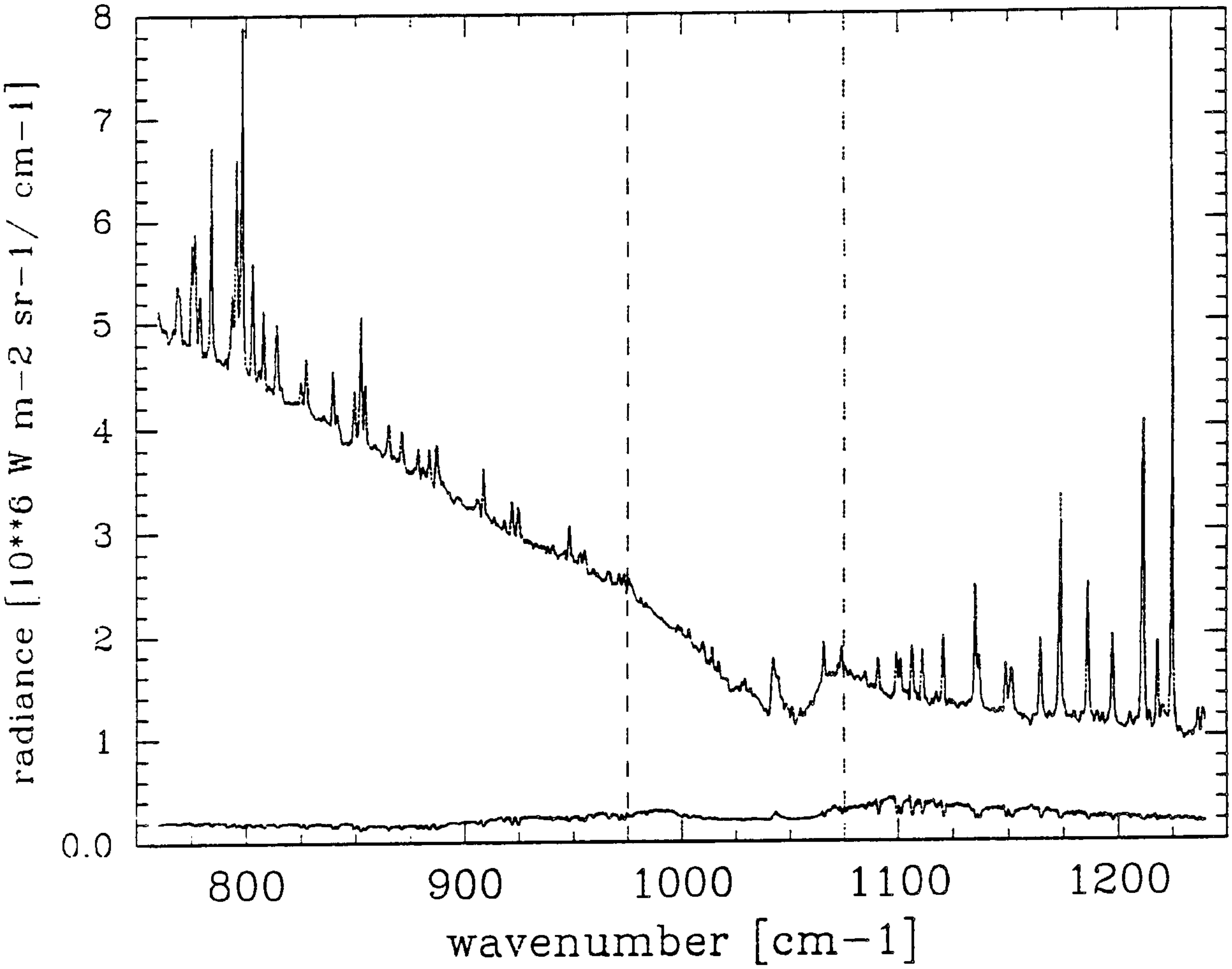

Figure 3.3b. The cirrus layer emitted radiance (upper curve) and reflected radiance (lower curve) for the Parsons2 #06 spectrum.

to over 120% at around 1100 cm^{-1} and remain above 100% from 1090 cm^{-1} to 1160 cm^{-1}.

The reflected/emitted radiance values for the high emittance spectrum shown in figure 3.3b vary spectrally from only to 3 or 4 percent near 800 cm^{-1} to over 25 percent around 1100 cm^{-1}. This again shows that the inclusion of reflectance is important even for a thick cirrus layer.

The relationship between the emittance and the reflectance of cirrus is shown in figure 3.4 for all of the data used for this study. The similarity between the Parsons curve and the Porto Santo curve is no surprise since it was stated in chapter two that a second order relation between the emittance and the reflectance was used in the model. The fact that the curves in this figure are not identical is due mainly to calculation and rounding errors.

A comparison between the emittance and the reflected radiances for the Parsons data set and the Porto Santo data set in figure 3.5 however, yields a departure between the two curves. Throughout the entire emittance range, the reflected radiance was consistently larger for the Porto Santo data set than for the Parsons data set. This is due to the warmer temperatures at the surface and for the sub-cirrus atmospheric layer for Porto Santo. This further demonstrates the importance of the role the reflection in the calculation of cirrus layer parameters as seen from the bottom of the cirrus cloud layer for the mid-latitudes and even more so for the tropics and sub-tropics.

It should be recalled that these results are found with the use of the emittance-reflectance relationship derived from a study by Yamamoto, et. al., 1970 for water clouds. The reflectance and the reflected radiance of cirrus clouds have been discussed in scientific literature. However, there seems to be an absence of any spectral reflectance information for ice clouds. In Hunt

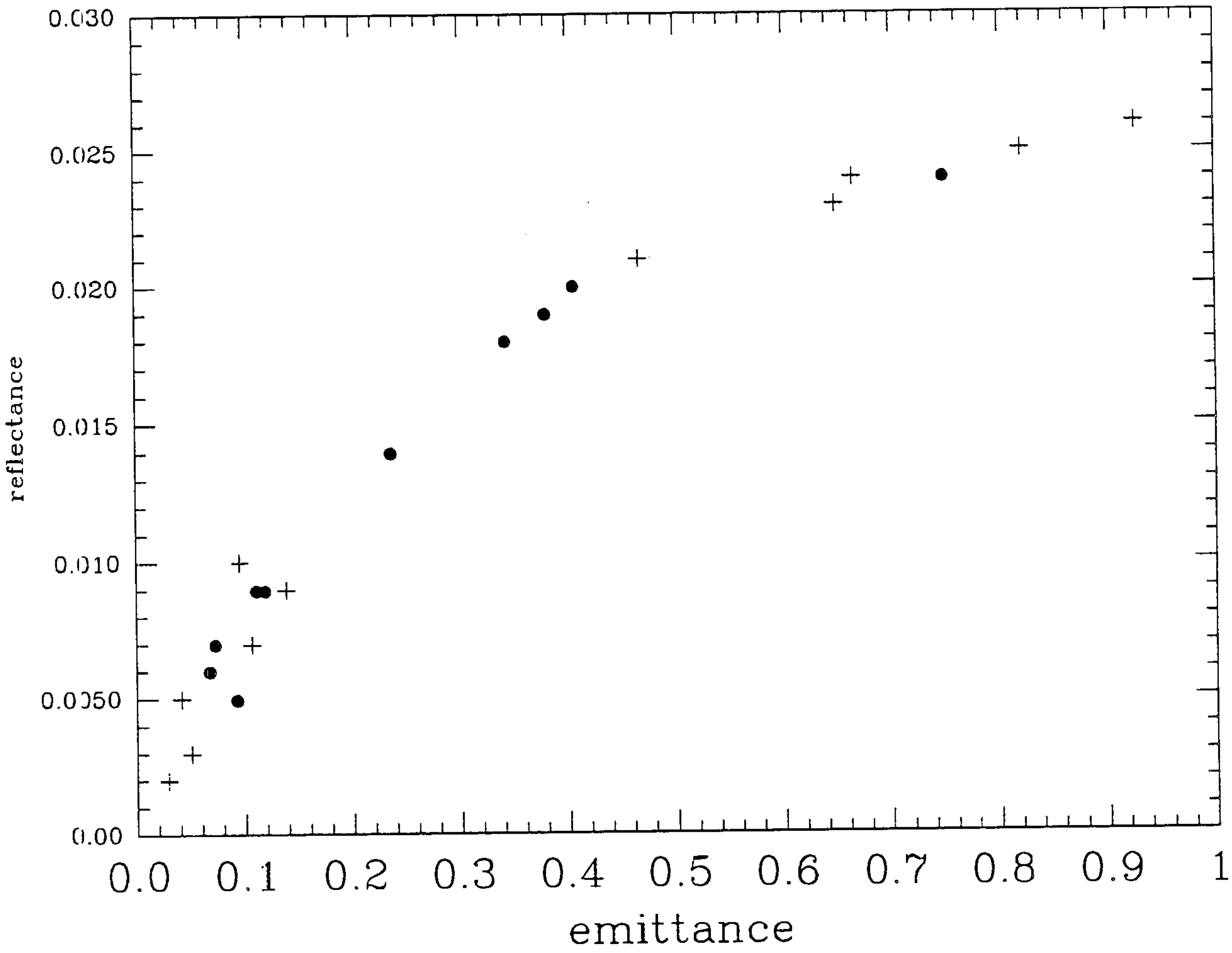

Figure 3.4. The derived 800 cm^{-1} to 1200 cm^{-1} spectrally averaged reflectance versus emittance for all of the Parsons (circles) and Porto Santo (crosses) cirrus spectra used for this study.

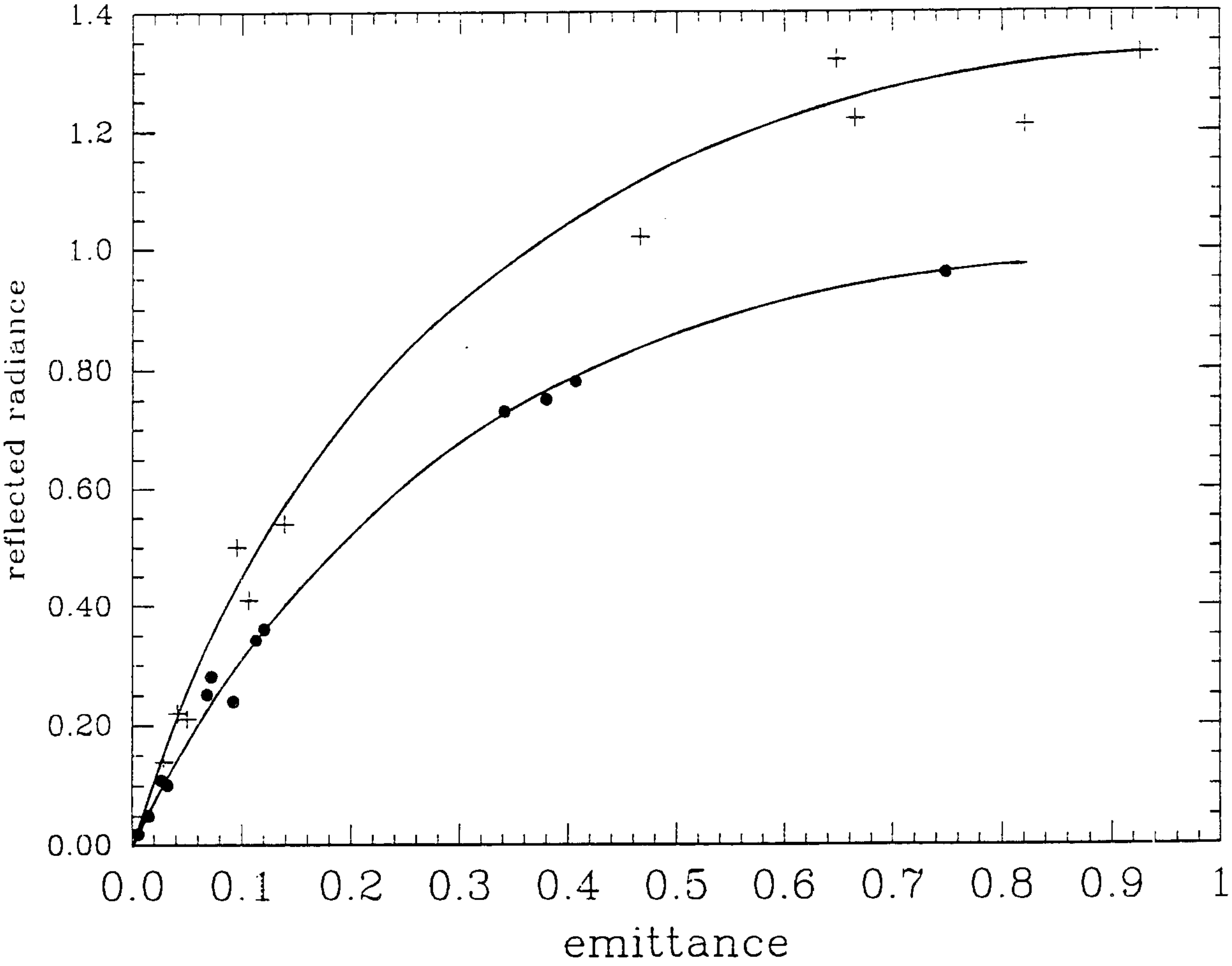

Figure 3.5. The derived 800 cm^{-1} to 1200 cm^{-1} integrated reflected radiance versus emittance for all of the Parsons (circles) and Porto Santo (crosses) cirrus spectra used for this study.

(1973), the emittances and transmittances of both water and ice clouds at 5 different wavelengths were presented in which it was shown that the reflectance of the ice clouds was about 75% greater than for water clouds at 11 μm.

Table 3.3 shows the additional impact that the inclusion of reflectance would have upon the results shown here if there was a 75 percent increase in the reflectance to emittance relationship that was employed in this study.

	rad	emit	tran	refl	reflrad%
ignoring reflectance	11.40	.823	.177	.000	0.0
including reflectance	10.44	.749	.227	.024	8.2
+ 75% increase	9.77	.695	.264	.041	14.3

Table 3.3. The derived emittance and transmittance values for the Parsons2 #06 case ignoring reflectance, with the inclusion of reflectance and with the inclusion of a 75% greater reflectance than was used for this study.

Stephens (1980) discussed the importance of the inclusion of reflectance in the calculation of cloud emittance values. Using a multiple-scattering radiative transfer model, he determined that the contribution to the downward emittance due to reflection was as high as 25% for a model tropical atmosphere. The reflected radiance contribution values derived for this study varied from 7 or 8% to as high as 33% (see Appendix C) for both the subtropical and the mid-latitude data sets.

3.2. Role of the sub-cloud layer

3.2.1. Surface radiance values

This section will first deal with surface measurements and secondly with FASCODE calculated surface values so that a comparison may then be made at the end of the section. Table 3.4 lists the total radiance at the surface from the cirrus layer, the total radiance as seen at the bottom of the cirrus layer and the percentage of the layer radiance that reached the surface calculated as the ratio of the first two values.

	radiance [$Wm^{-2}sr^{-1}$] surface	layer	ratio
Parsons1 #60	.87	1.10	.79
Portsan3 #45	3.22	8.29	.39

Table 3.4. 800 cm^{-1} to 1200 cm^{-1} integrated downwelling radiances emitted from the cirrus layer present at the bottom of the cirrus layer and the fraction of that which reaches the surface.

These numbers clearly indicate that there is a large difference in the impact of the sub-cirrus layer upon the cirrus radiances measured at the surface between the mid-latitude and the subtropical observations. This is, of course, principally due to the difference in the sub-cirrus layer transmittance values. Figure 3.6 shows the FASCODE II calculated sub-cirrus layer spectral transmittances associated with the Parsons1 #60 spectrum and with the Portsan3 #45 spectrum.

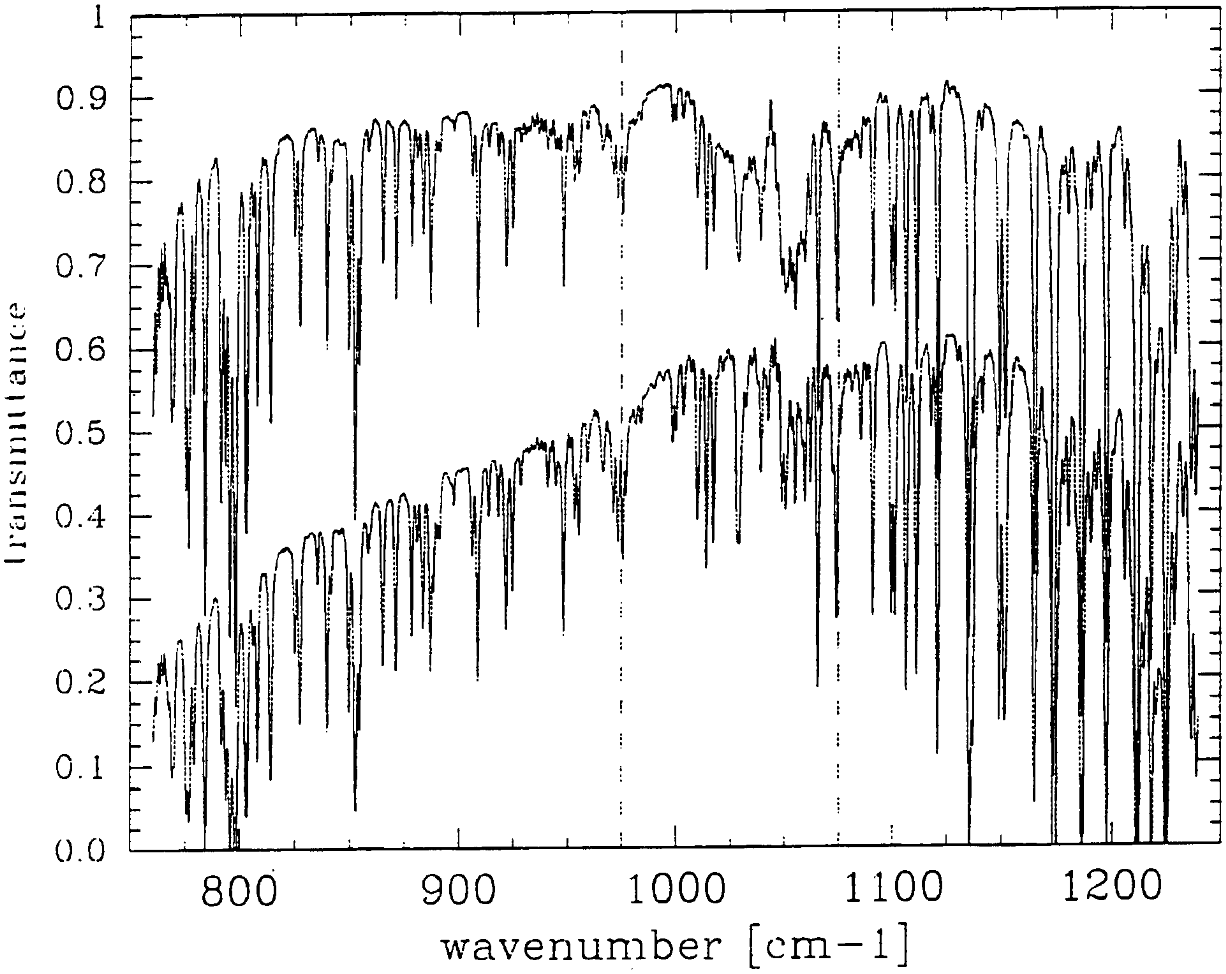

Figure 3.6. A comparison between transmittances for the most transparent (Parsons1, upper curve) and the most opaque (Portsan3, lower curve) subcirrus layers.

The integrated values for the Parsons and Porto Santo transmittances shown in figure 3.6 are .82 and .42, respectively. However, the fraction of the cirrus layer radiances reaching the surface for these two events were calculated to be only .79 and .39. Looking back at figures 3.1a and b, it is shown that the total radiance coming from the cirrus layer (as seen at the bottom of the layer) is the largest below 800 cm^{-1} and decreases across the window with the smallest radiance values from 1100 cm^{-1} to 1200 cm^{-1}. Note that the transmittances in figure 3.6 are the smallest near 800 cm^{-1} and are the largest around 1100 cm^{-1}. It is this variability in the transmittance of the atmospheric window and the appropriate Planckian emission from the cirrus layer that cause the fractions of the integrated radiance values that reach the surface to be a smaller fraction than the integrated transmittance values.

It was shown in chapter 2 that the lowest 6-8 km of the troposphere is responsible for more than 98% of a measured clear sky radiance. With this in mind, the impact of the sub-cirrus layer on the magnitude of the cirrus sky measurements becomes very evident when looking at figure 3.7. This figure demonstrates the significant difference in the magnitudes of the clear sky measurements that were made at the two locations and illustrates the impact of the sub-cirrus layer upon the surface radiance values.

The FASCODE sensitivity tests were performed as follows. Using an arbitrarily chosen sounding taken during the Parsons2 case on Nov 26th at 1936Z to initialize the FASCODE model, tests were run by systematically varying the relative humidity and temperature profiles to examine the role of these parameters as an influence upon the surface measurements. The RH tests were run using constant values of RH throughout the atmospheric column extending vertically upward from the surface. The temperature tests were done by incrementing the

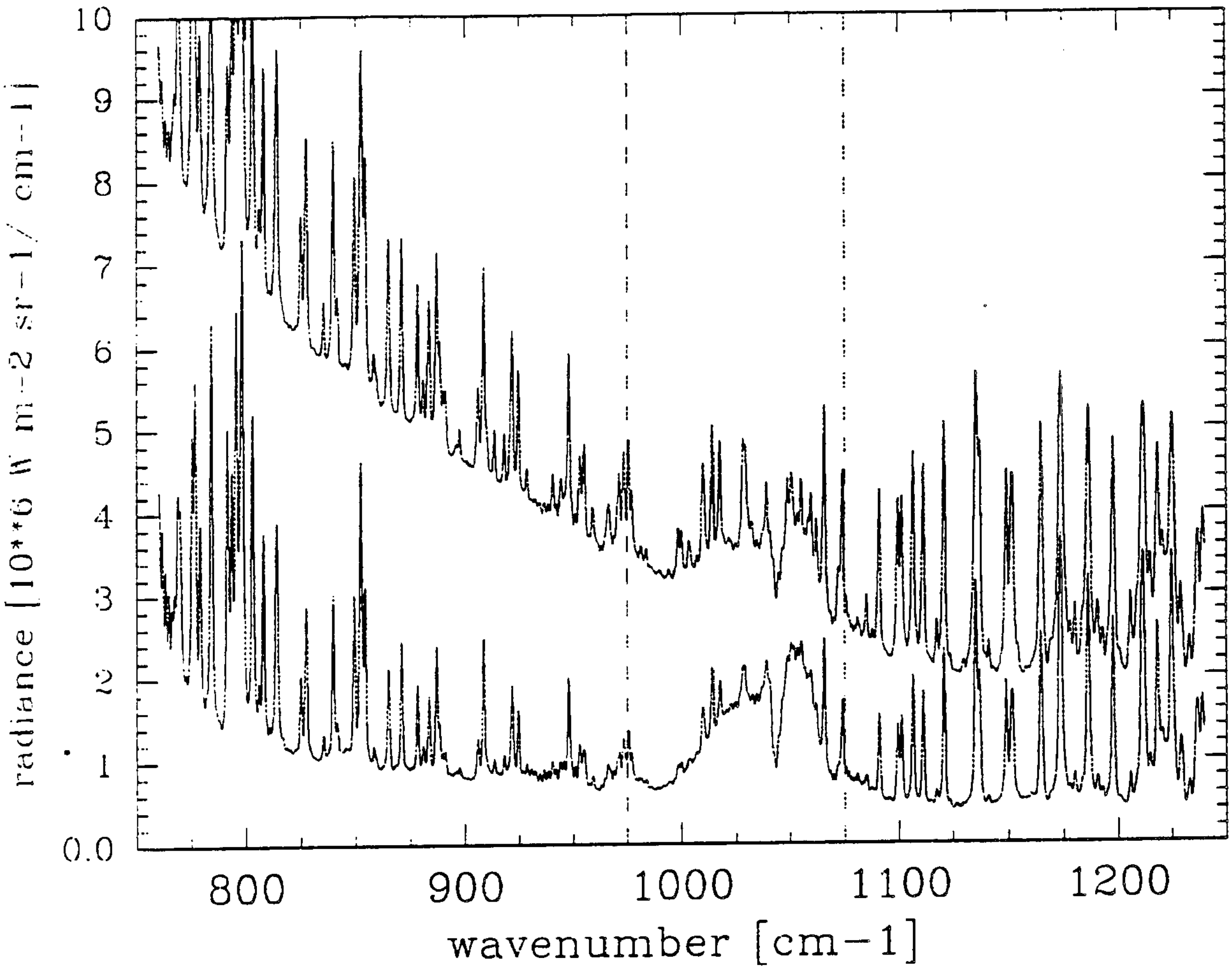

Figure 3.7. A comparison between the least emissive (Parsons1, upper curve) and the most emissive (Portsan3, lower curve) clear sky radiances.

existing temperatures in the sounding data.

Figures 3.8 and 3.9 show the results for a 10% increase in the column RH value (from 60% to 70%) and for a 2 degree temperature increase over the measured temperature profile, respectively. The integrated radiance values calculated for the 60% and the 70% column RH profiles bracket the integrated radiance value calculated from the original sounding data.

The integrated values of these plots are nearly identical suggesting that a 10% change in the relative humidity would cause a change in the magnitude of the surface radiance that is similiar to the change caused by a 2 Kelvin change in the temperature.

For each of the six cases that were used for this study, there was a measured clear sky spectrum. Figure 3.10 shows the spectral differences between four of these and the clear sky spectrum from the Parsons1 data set which had the smallest integrated value of the six. The slope of the spectra in the low wavenumber end of the window becomes steeper with increasing values of the integrated radiance while the magnitude of the radiances increases in a more uniform fashion.

The corresponding FASCODE calculated clear sky spectra differences shown in figure 3.11 appear to change in the same manner as described in section 1 with the exception of a slight curvature in the low wavenumber end of the window which becomes more evident with increasing values of integrated radiance.

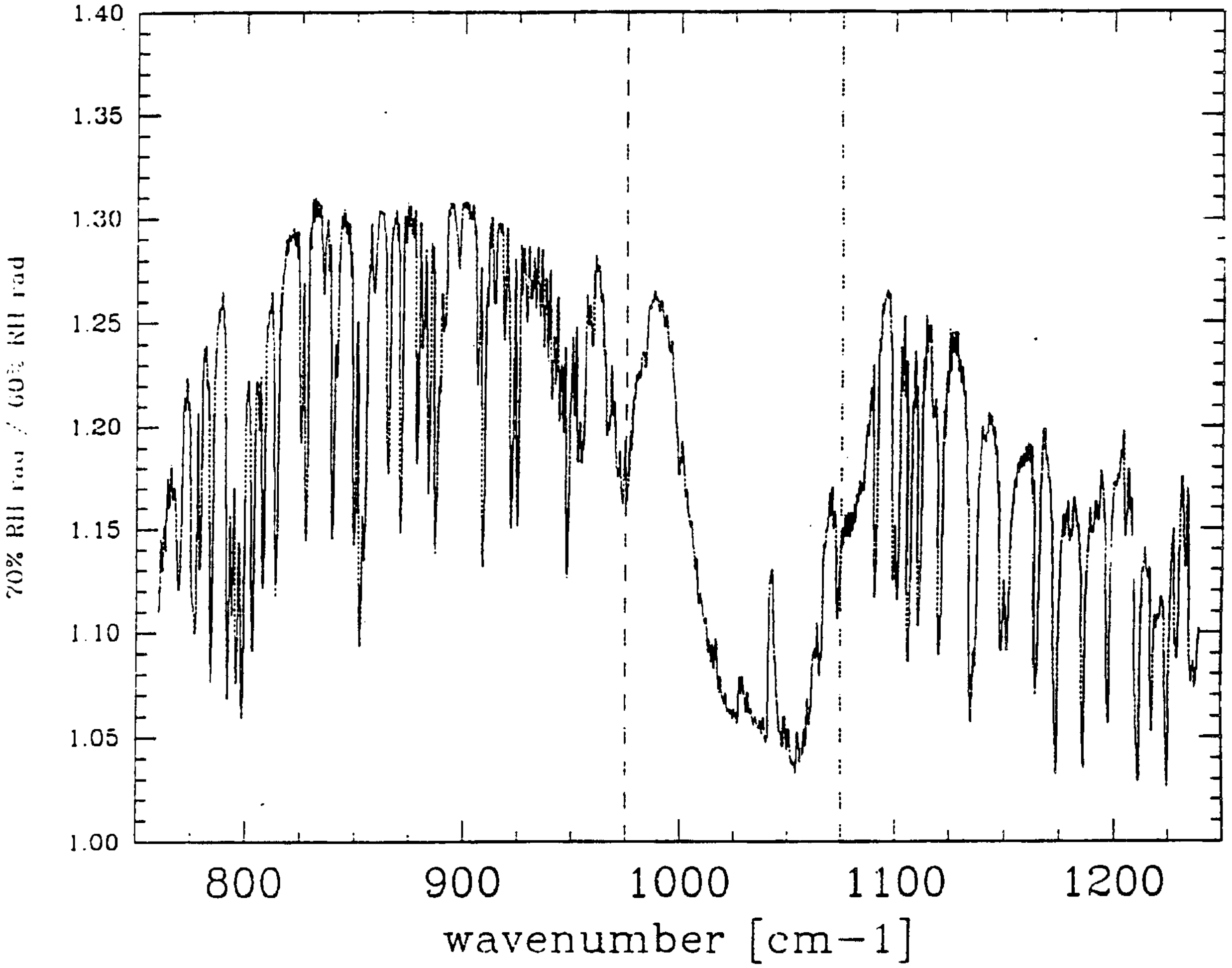

Figure 3.8. Spectral FASCODE calculated radiance ratio of an atmosphere with 70% column relative humidity to an atmosphere with 60% column relative humidity.

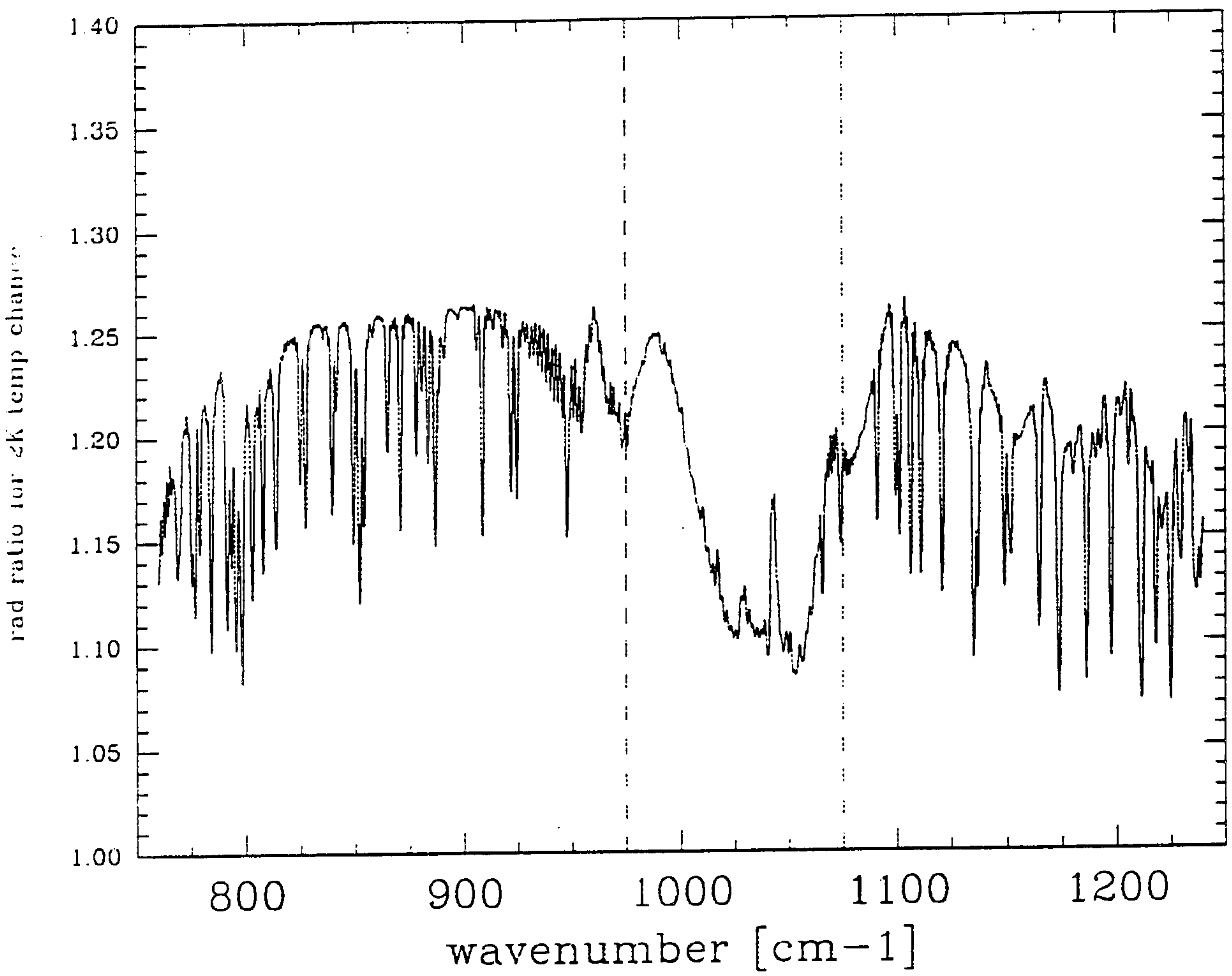

Figure 3.9. Spectral FASCODE calculated radiance ratio of an atmosphere sounding biased 2 K warmer to an unbiased atmospheric sounding.

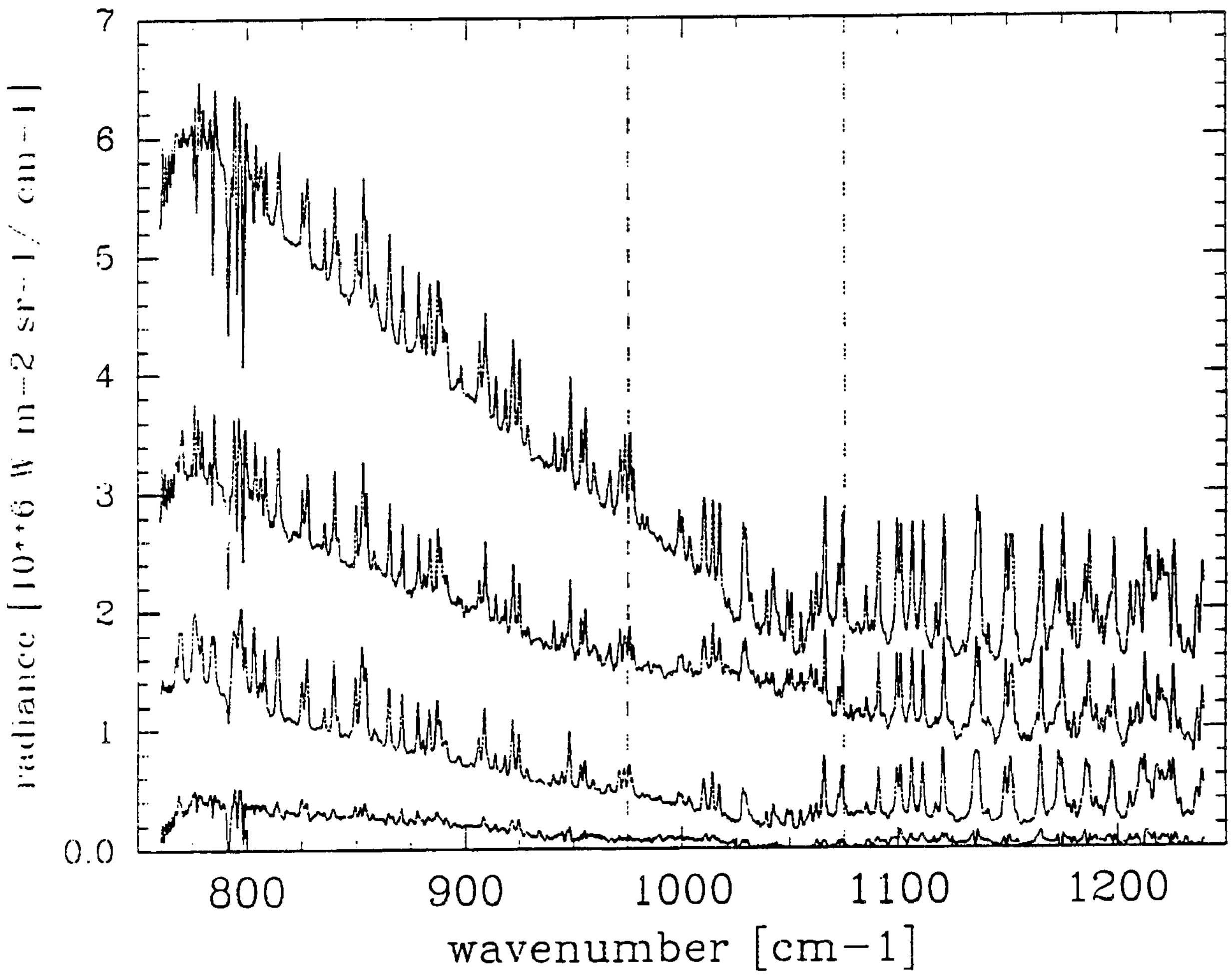

Figure 3.10. The radiance measurement differences between the least emissive clear sky spectrum used in this study, Parsons1, and the more emissive Parsons2, Parsons3, Portsan2 and Portsan3 clear sky spectra in order from the lowest curve to the highest curve.

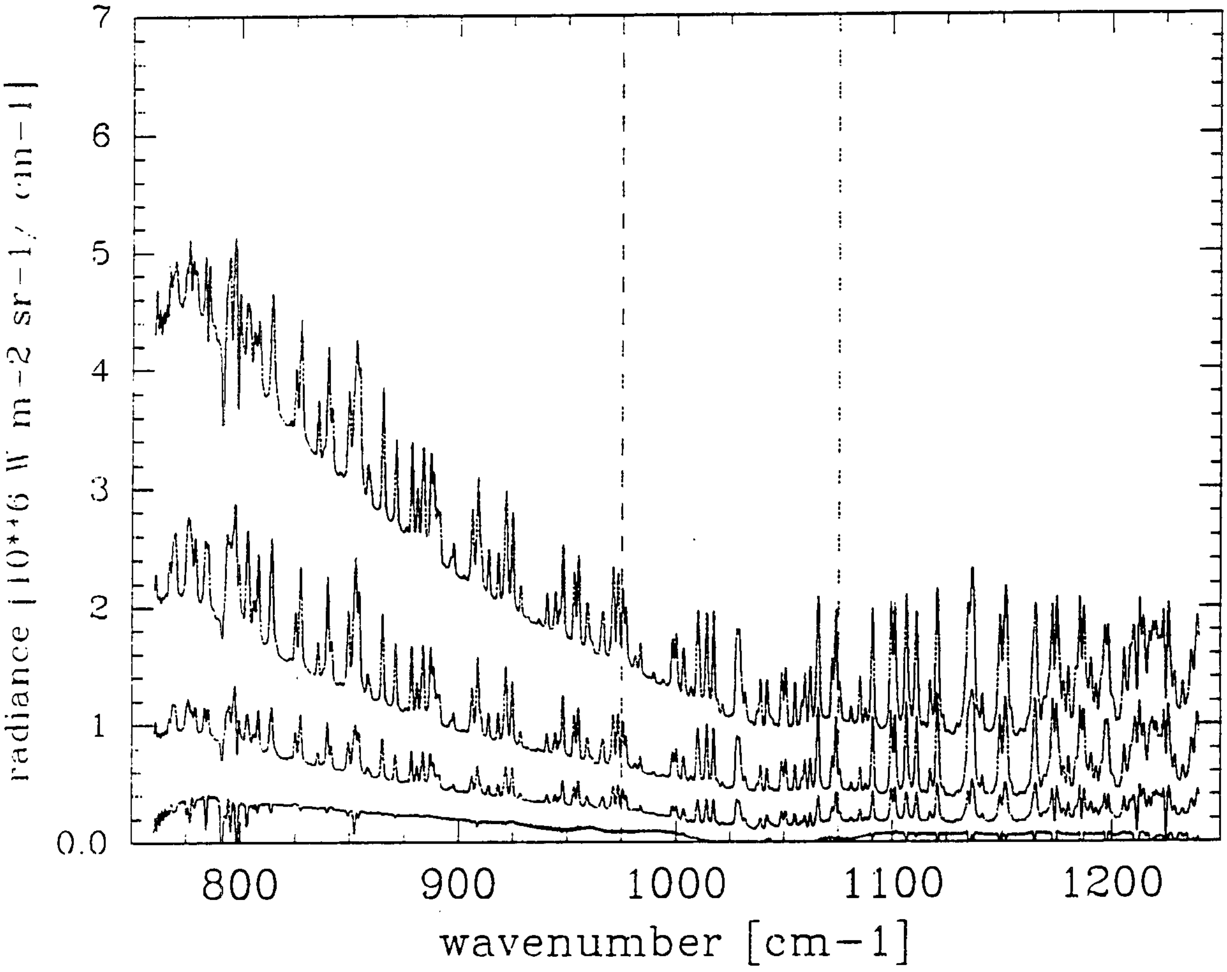

Figure 3.11. The FASCODE calculated radiance differences between the least emissive clear sky spectrum used in this study, Parsons1, and the more emissive Parsons2, Parsons3, Portsan2 and Portsan3 clear sky spectra in order from the lowest curve to the highest curve.

3.2.2. Remote sensing of the cirrus layer

Table 3.5 shows the increase in the integrated radiance values at the surface compared to the existing clear sky radiance based on Parsons measurements and FASCODE calculations. The two spectra from the Parsons1 case are for cirrus with low emittances.

		radiance[$Wm^{-2}sr^{-1}$]
measurements:	Parsons1 #30	.15
	Parsons1 #60	.87
RH bias tests:	10% increase	.79
	20% increase	1.64
	30% increase	2.53
temp bias tests:	1 K increase	.44
	2 K increase	.92

Table 3.5. 800 cm^{-1} to 1200 cm^{-1} integrated radiances for two low emittance Parsons cirrus and for the relative humidity and temperature bias FASCODE tests.

Temperature sensors on sondes are generally accurate to within two-tenths of a degree throughout most of the troposphere. Given the test results presented in the above table, a bias of 0.25 K between the time of the clear sky measurement and the time of the cirrus sky measurement would result in an integrated radiance error of about .1 $Wm^{-2}sr^{-1}$. For an extremely low emittance cirrus layer such as that in the Parsons1 #30 spectra with a radiance of only .15 $Wm^{-2}sr^{-1}$, a bias of .1 $Wm^{-2}sr^{-1}$ would dramatically change the values for the calculated radiance and emittance of the cirrus layer. The impact of such a change upon a spectrum such as the Parsons1 #60 cirrus spectrum would be much smaller and would be negligible for measurements of cirrus layers with even a moderate surface radiance value.

The main problem lies within the often large inaccuracies in the measurements of water vapor. A 10% negative bias in the sub-cirrus layer relative humidity values would cause a decrease in the measured surface radiance that would be much larger than the increase in the magnitude of the measured radiance with the onset of a cirrus layer such as the one that was present for the Parsons1 #30 measurement. This change would all but wipe out the increase caused by the cirrus layer present during the Parsons1 #60 measurement.

If the measured radiance could be modeled perfectly, then normalizations could be made flawlessly. Of course, the sounding data used to initialize this model would have to be perfect. In order to determine the accuracy to which water vapor must be measured, let us assume that there exists a perfect model and the only errors introduced into the radiance calculation come from radiosonde water vapor measurements. Let us also assume that the temperature is measured perfectly. Then, according to the above table, in order to calculate the parameters for the cirrus layer present during the Parsons1 #30 measurement to within 50% error, the relative humidity would have to be resolved to within a 1% bias! In order to calculate the parameters for the much more radiant cirrus layer present during the Parsons1 #60 measurement to within 50% error, the relative humidity would still need to be measured to within a bias of 5% and to minimize the error to 10%, the relative humidity would again need to be measured to within a bias of 1%! Even knowing these rather severe constraints, the normalization scheme detailed in chapter 2 seems to yield realistic results which will be presented in chapter 4.

3.3. Normalization of measurements and calculations

3.3.1. Magnitude of the normalizations

The results following the normalization procedures described in Chapter 2 are shown in table 3.6. The first two columns are the integrated surface radiance measurements before and after normalization. The last two columns list the values for the integrated radiances found from FASCODE clear sky calculations using sounding data nearest to the times of the cirrus sky measurement and of the associated clear sky measurement for that case, respectively.

	radiance [$Wm^{-2}sr^{-1}$]			
	unadj	adj	cloud	clear
Parsons1 #60	.85	.87	3.55	3.60
Parsons2 #06	9.86	8.52	4.89	4.03
Portsan2 #39	10.83	8.99	8.14	7.19
Portsan2 #75	.67	1.01	7.02	7.19
Portsan3 #45	3.22	3.22	11.45	11.45

Table 3.6. Integrated cirrus forcing radiances for both unadjusted and normalized spectra and the associated clear column FASCODE III calculations.

For the Parsons2 #06 and Portsan2 #39 spectra, the FASCODE generated clear sky values for the time at which the clear sky spectra was measured are smaller than the calculated clear sky values for the times at which the cirrus sky spectra were taken. As a result, the radiance values for the cirrus spectra were reduced following the normalization procedure. The effect on the Parsons1 #60 and the Portsan2 #75 spectra was the opposite, however, in light of the fact that the FASCODE generated clear sky values for the time at which the clear sky spectra were measured were larger than the calculated clear sky values for the times at which the cirrus sky spectra were taken. There was no change following normalization for the data for the Portsan3 event. All of the data for this case were taken within a time span of 72 minutes, and so it is a reasonable assumption that there was little change in the water vapor and temperature structures. Also, there is only one set of sounding data available that was taken near that time frame.

Although these changes may appear small in magnitude, they are significant. The following section will demonstrate the importance of normalizing the contribution of the sub-cloud layer when evaluating the effect of cirrus on the surface measured radiance.

3.3.2. Importance of the normalization: case study

The following table lists the radiances due to the cirrus presence with and without the normalization procedure. The importance of a normalization quickly will become evident. There was no meaningful information about the cirrus that could be drawn from the raw, unadjusted Parsons3 surface radiance measurements. The reason for this is that the radiance for the clear sky measured by the interferometer at 1956Z on the 6th is 7.07 $Wm^{-2}sr^{-1}$ and is larger than all of the measured cirrus sky radiances which range in value from 5.30 $Wm^{-2}sr^{-1}$ to 7.00 $Wm^{-2}sr^{-1}$; therefore, measurement differences between the cirrus spectra and the clear sky spectrum yielded negative emittances which have no physical meaning.

				radiance [$Wm^{-2}sr^{-1}$]	
Parsons3 - 12/5-6/91			layer hgt[km]	unadj	adj
#51	cirrus	1708Z	11-12	-1.87	.73
#75	cirrus	1932Z	10-12	-.96	1.07
#93	cirrus	2113Z	9.6-12.2	-2.72	2.12
#09	mult-layer	0114Z	8.5-12	-.97	.74
#33	2-layer ci	0758Z	7.2-9.4	-.71	1.51
#45	faint ci	0930Z	9	-1.68	.37
#30	clear	1956Z			

Table 3.7. Unadjusted and normalized integrated downwelling radiance values at the bottom of the cirrus layer.

The FASCODE calculated clear sky radiance for the time at which the clear sky spectrum was measured is 5.14 $Wm^{-2}sr^{-1}$ while the calculated clear sky values for the times at which there were cirrus present ranging from 3.51 $Wm^{-2}sr^{-1}$ to 4.06 $Wm^{-2}sr^{-1}$. This suggests that the sub-cloud layer experienced a significant increase in either temperature, water vapor amount or both or in some other unaccounted for atmospheric constituent.

Figures 3.12a and b show the temperature and relative humidity data, respectively, from sondes that were launched at 1230Z and at 1704Z on the 6th. The temperature change appears to be fairly small except for right near the surface, however, the data presented in figure 3.12b show a significant increase in the relative humidity values extending from 800 mb all the way up to 400 mb between the launch times of 1230Z and 1704Z. This large increase in the water vapor content for most of the lower troposphere would account for the magnitude of the clear sky spectrum actually being larger than the magnitudes for all the cirrus spectra taken previous to this increase. Also, the cirrus were very high and cold on the 5th and were multi-layer or

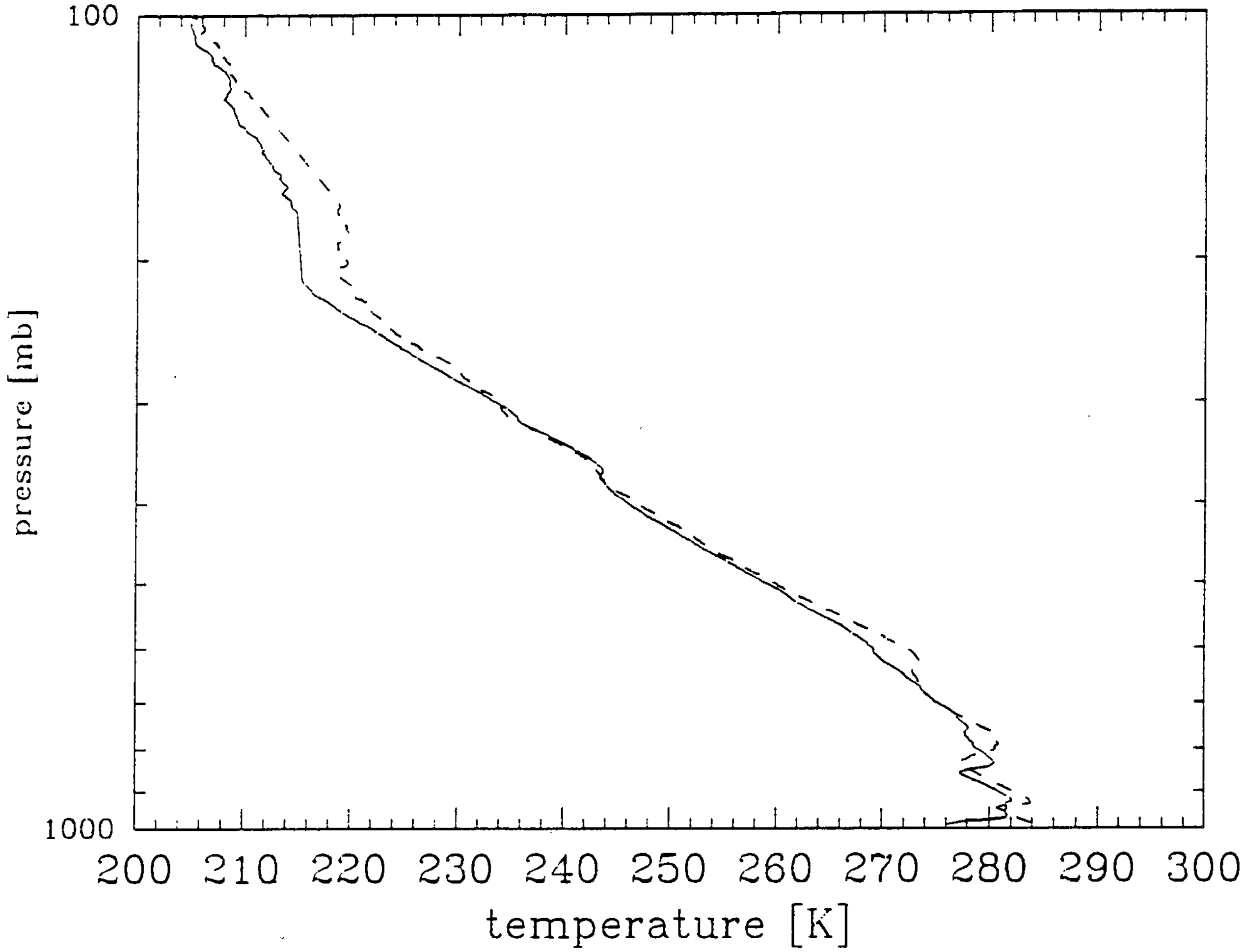

Figure 3.12a. The Parsons December 6, 1991 1230Z (solid line) and 1704Z (dashed line) temperature profiles.

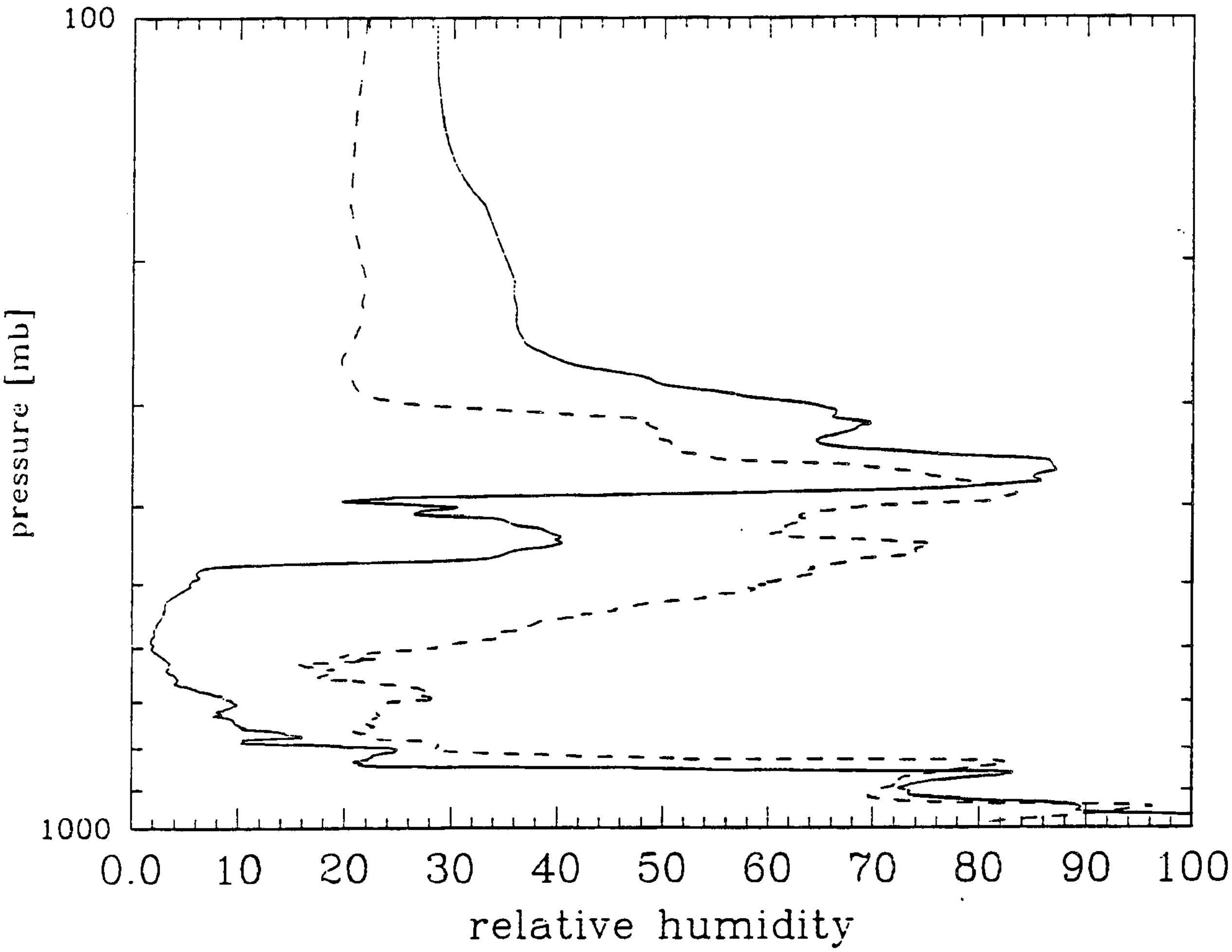

Figure 3.12b. The Parsons December 6, 1991 1230Z (solid line) and 1704Z (dashed line) relative humidity profiles.

nearly sub-visual on the 6th. So, the increase of moisture between 0930Z and 1936Z on the 6th caused an increase to occur in clear sky surface measurement that was larger in magnitude than the decrease in the magnitude of the radiance due to the disappearance of the cirrus.

Again, because of the importance of trying to understand the impact of thin cirrus upon our climate, a normalization to the data to try to compensate for sub-cloud layer moisture and temperature changes is vital, especially when observing cirrus with small emittance values.

3.4. Uncertainty Analysis

An uncertainty analysis was performed in order to determine the impact of random, uncorrelated errors in the measured input parameters as well as a probable error in the emittance-reflectance empirical relation that was used for this study. This analysis was performed on the Parsons2 #90 spectrum that was taken on November 26, 1991 at 2030Z. Sixty different sets of random errors were found.

The sounding data used for the initialization of the FASCODE model were assigned a one standard deviation atmospheric column bias error of 1K for the temperature and 10% RH column bias error for the relative humidity. The cloudbase height error was set at 5% of the value for the measured height. By multiplying the numbers output from the random number generator which ranged from -1 to +1 by these assigned errors, these errors were varied in a random fashion and then input into the FASCODE model in order to generate the various spectra that are needed to perform the normalization procedure. For the nested iterative scheme, the cloudbase and cloudtop temperatures were assigned errors of 3.5K and 7K, respectively, and the surface temperature was assigned a 1K error. The emittance-reflectance relationship was given an error that was 10% of the reflectance value.

A bar-graph of the distribution of emittance values is shown in figure 3.13 with a smoothed distribution curve superimposed upon it. The distribution is very nearly Gaussian as one might expect. The emittance value for this spectrum was found to be 0.342. For the uncertainty analysis, both the average and the mean were 0.340, the standard deviation was 0.020 and the standard error was 0.0026. The emittances found for this analysis ranged in value from 0.300 to 0.385.

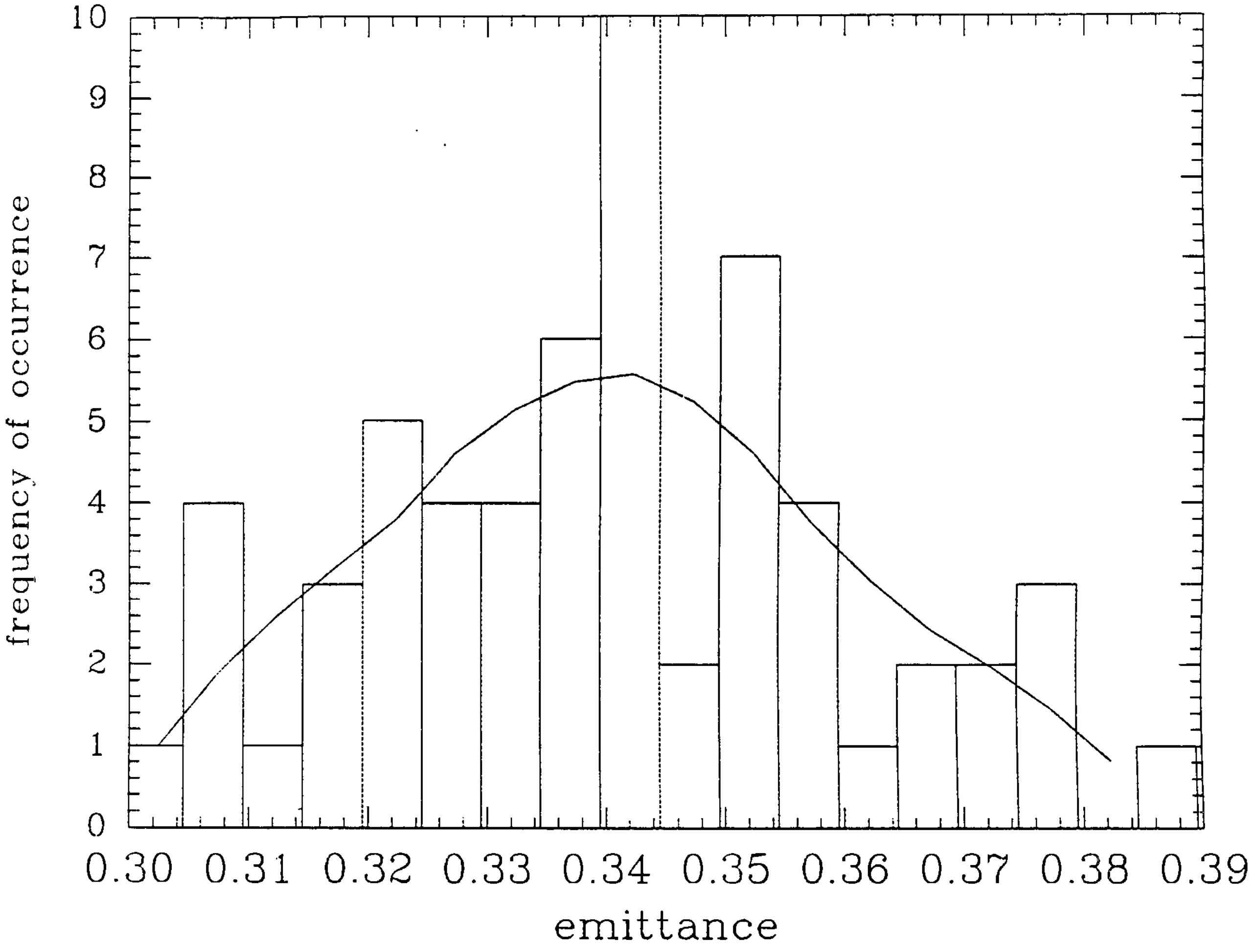

Figure 3.13. Frequency of occurrence of emittances from the random error analysis.

4. RESULTS OF THE STUDY

The results for the deduced cirrus layer properties prior to transmission to the surface and for the radiative forcing by the cirrus cloud layers along with their impact upon the surface energy budget are presented.

4.1. Radiative properties of cirrus

With one exception, the derived mean emittances over the spectral bandpass 800 cm^{-1} to 1200 cm^{-1} from the Parsons data set ranged from 0.006 for a high, thin layer of sparse cirrus observed on Nov. 21 at 2250Z to 0.406 for a 3.5 km thick cirrus layer which was observed on Nov. 26 at 2000Z. The exception was an emittance value for a cirrus layer that was observed was 0.749 on Nov. 26 at 2140Z. The derived emittances from the Porto Santo data set ranged from 0.029 to 0.926.

Figure 4.1a shows the emittance plotted against the thickness of the cirrus layers used in this study from both the Parsons data set and the Porto Santo data set. The multi-layer data is from the Parsons3 data set. Figure 4.1b is the same as 4.1a except that radiance is on the y-axis in place of the emittance. It can be seen from these figures that both the emittance and the emitted radiance increased with increasing cirrus layer thickness. But, what is even more evident from these figures is that the Porto Santo subtropical cirrus had much higher emittances, given the same cirrus layer thickness, than did the Parsons mid-latitude cirrus. Furthermore, figure 4.1b, shows that the differences between the Porto Santo and the Parsons cirrus layer

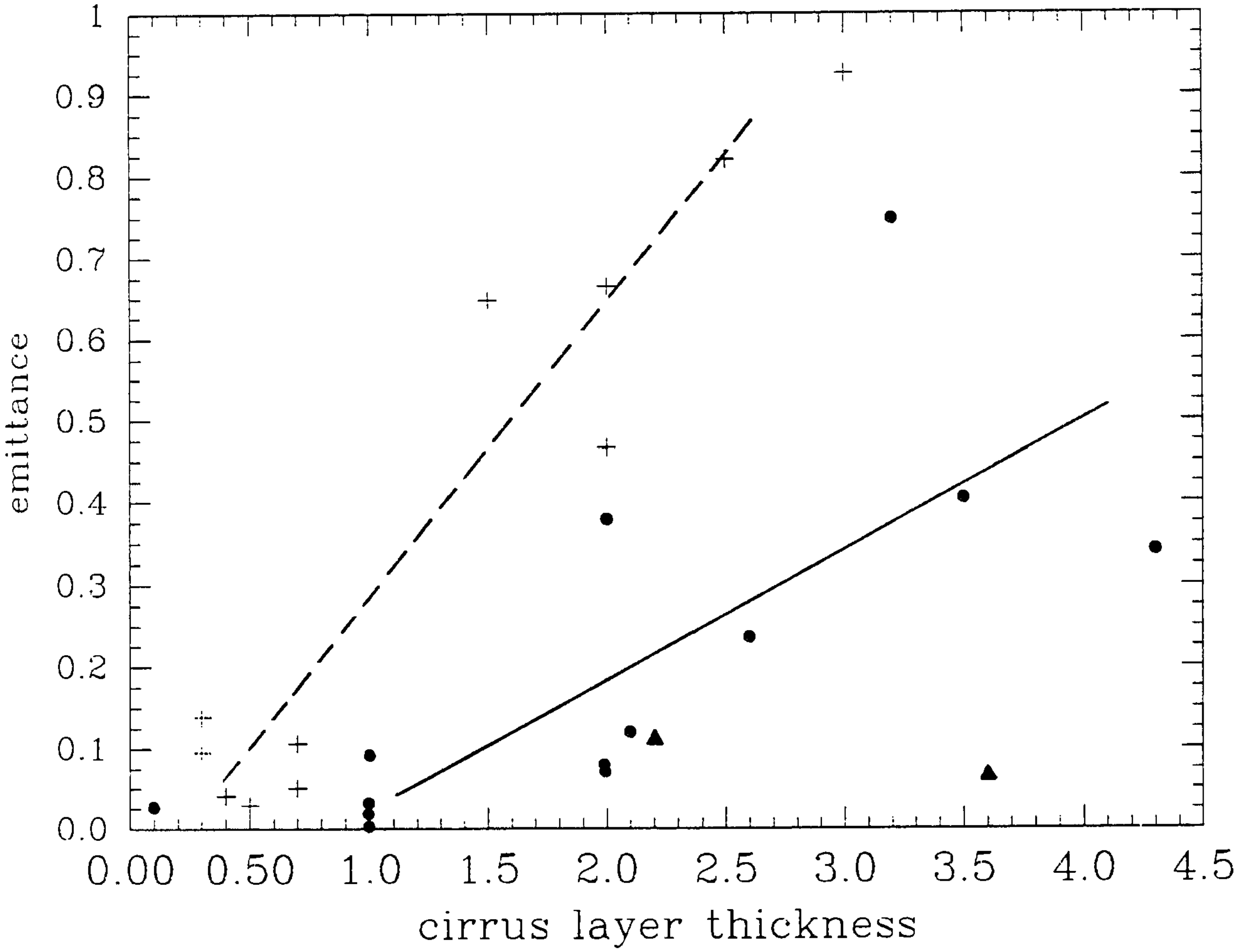

Figure 4.1a. Emittance versus cirrus layer thickness for Porto Santo cirrus (crosses), Parsons cirrus (circles) and multi-layer cirrus from Parsons (triangles).

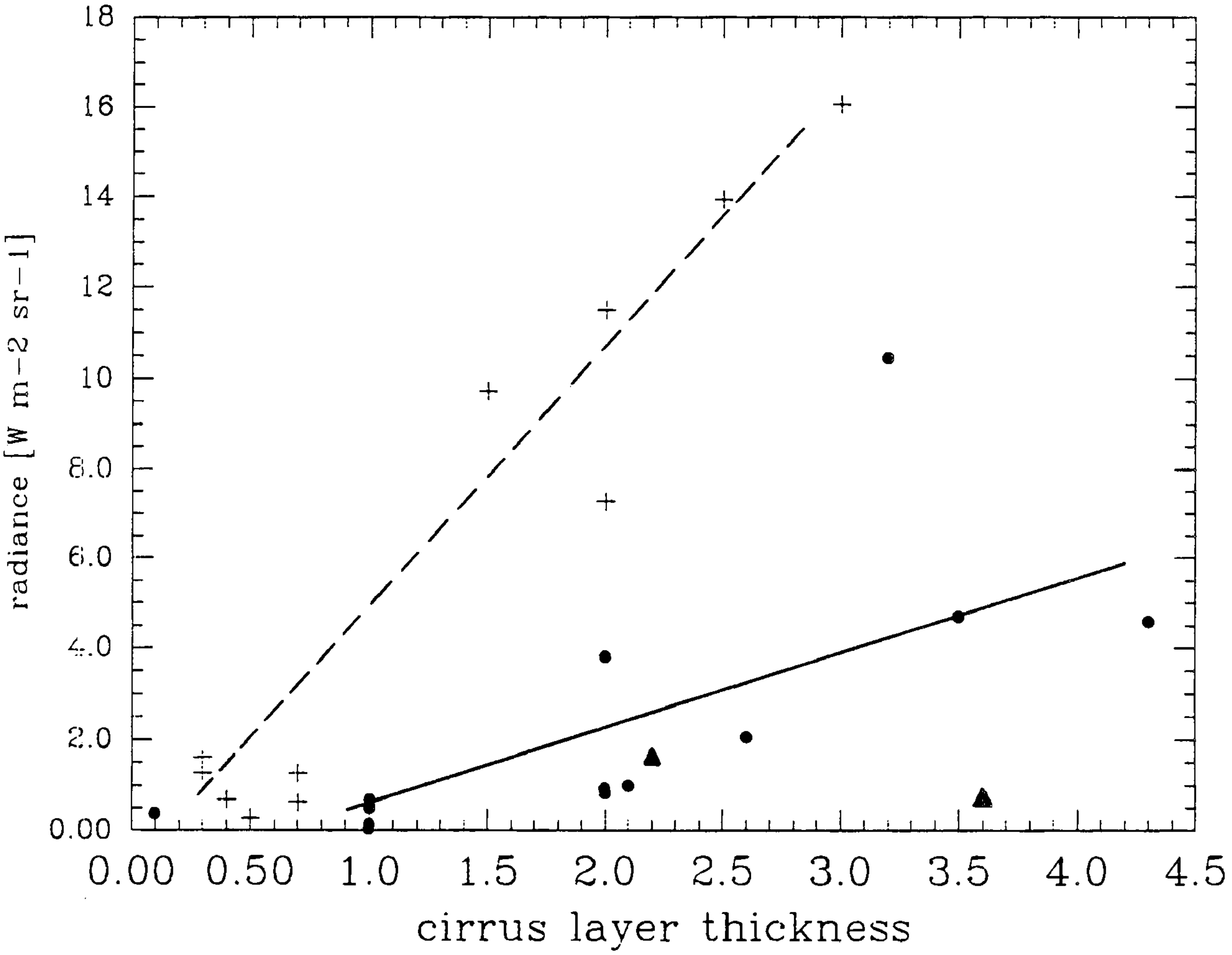

Figure 4.1b. 800 cm^{-1} to 1200 cm^{-1} integrated radiance versus cirrus layer thickness for Porto Santo cirrus (crosses), Parsons cirrus (circles) and multi-layer cirrus from Parsons (triangles).

emitted radiances are even more striking. The multi-layered cirrus decks were much less emissive than either of these.

Shown in figure 4.2a are data for the cirrus layer emittance versus the median temperature of the cirrus layer. There seems to be a general trend of increasing emittance with increasing temperature. However, what's most striking, again, is the difference between the Parsons and the Porto Santo data point distributions. The Parsons mid-latitude cirrus had higher emittance values at colder temperatures than did the Porto Santo subtropical cirrus decks. The slope of the two curves shown in figure 4.2b for the cirrus extinction coefficient versus the median temperature of the cirrus layer are similiar to those shown in figure 4.2a.

Table 4.1 shows the results for the integrated values of the emitted radiation by the cirrus cloud, the radiation which is reflected by the cirrus layer, and the percentage of reflected radiation to the total radiation coming from the cirrus layer, i.e., reflected/(reflected+emitted).

	radiance[$Wm^{-2}sr^{-1}$] emit	 refl	 reflrad%
Parsons1 #60	.82	.28	26.3
Parsons2 #06	10.44	.96	8.2
Portsan2 #75	1.27	.50	28.4
Portsan2 #39	16.04	1.33	7.5

Table 4.1. The emitted and reflected downwelling radiances and the reflected radiance percentage of the total downwelling radiance at the bottom of the cirrus layer for four cirrus events.

The vital importance of considering the effects of reflection for the retrieval of cirrus layer properties is apparent from the fact that between 7% and 28% of the radiance emerging

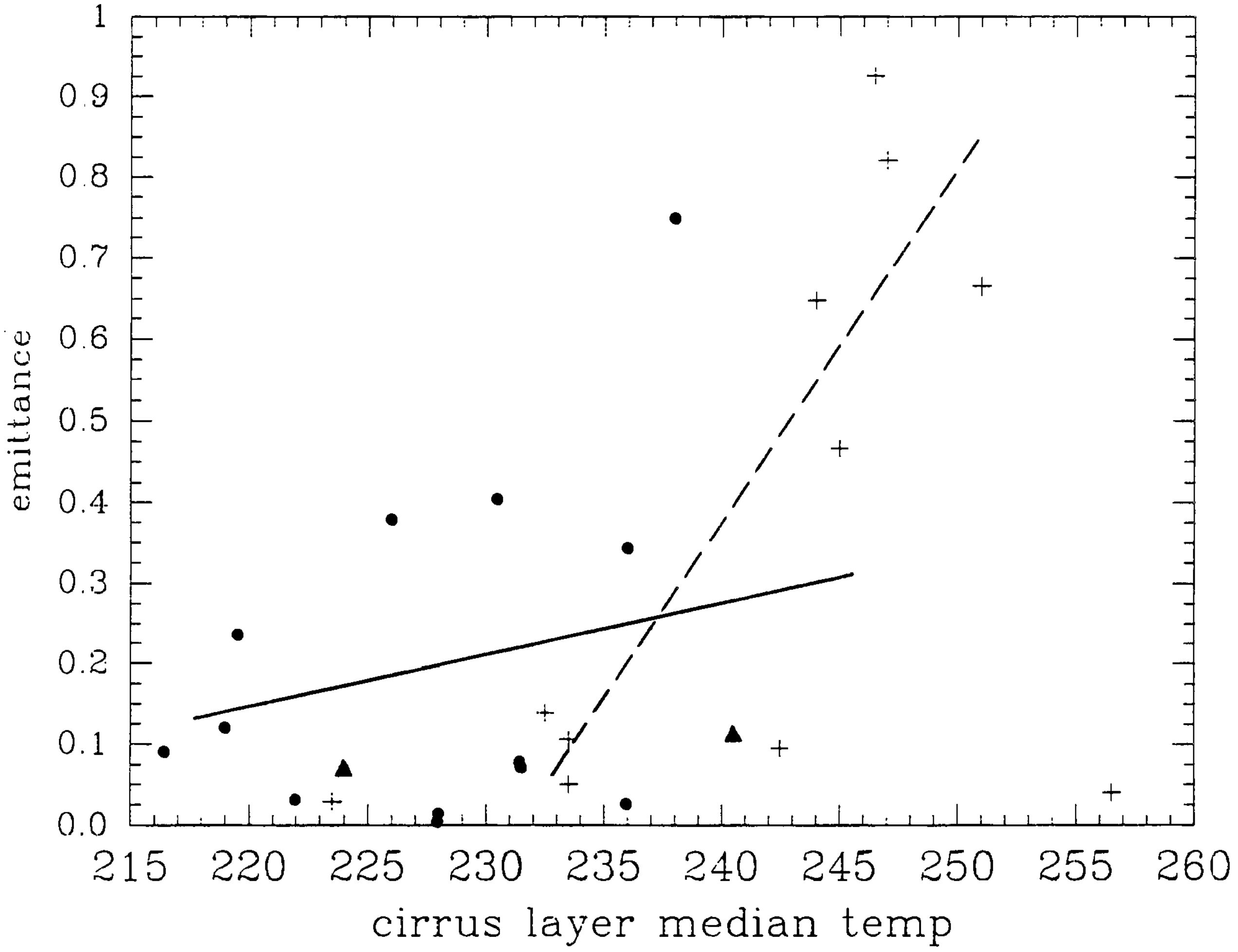

Figure 4.2a. Emittance versus cirrus layer median temperature for Porto Santo cirrus (crosses), Parsons cirrus (circles) and multi-layer cirrus from Parsons (triangles).

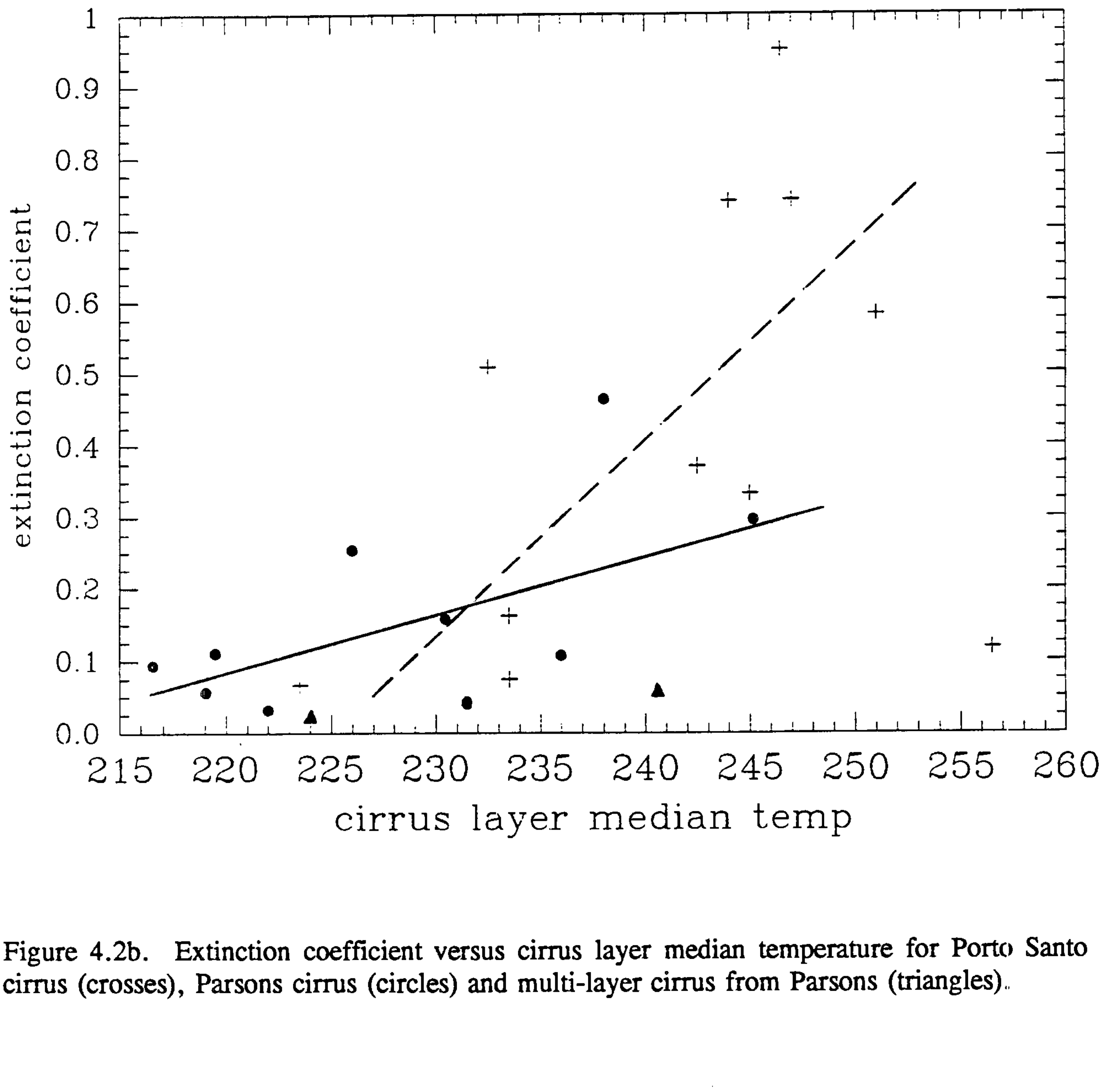

Figure 4.2b. Extinction coefficient versus cirrus layer median temperature for Porto Santo cirrus (crosses), Parsons cirrus (circles) and multi-layer cirrus from Parsons (triangles).

from the base of the cirrus layer results from reflection of the upward irradiance. This is especially important for thin, low emissive cirrus clouds.

4.2. Impact of cirrus upon surface radiance values

4.2.1. Effect on the surface energy budget

Figures 4.3a-d show comparisons of spectra measured under cirrus conditions to spectra measured under clear sky conditions taken at times nearest to the time of the cirrus sky measurement. One low emittance and one high emittance spectra is presented for each location.

Table 4.2 lists the integrated radiances measured at the surface during the presence of cirrus, the fraction of the integrated surface radiance from the cirrus and the percentage of the measured radiance which is attributed to the cirrus presence. The values in the last column are

	radiance[$Wm^{-2}sr^{-1}$]		
	total	cirrus	cirrus%
Parsons1 #60	5.46	.87	16
Parsons2 #90	10.11	4.00	40
Parsons2 #06	14.32	8.52	59
Portsan2 #75	12.17	1.01	08
Portsan3 #45	19.88	3.22	16
Portsan2 #39	21.59	8.99	42

Table 4.2. The 800-1200 cm^{-1} downwelling radiance and the radiance contribution from the cirrus layer to the surface and the cirrus contribution percentage of the total radiance for six cirrus events.

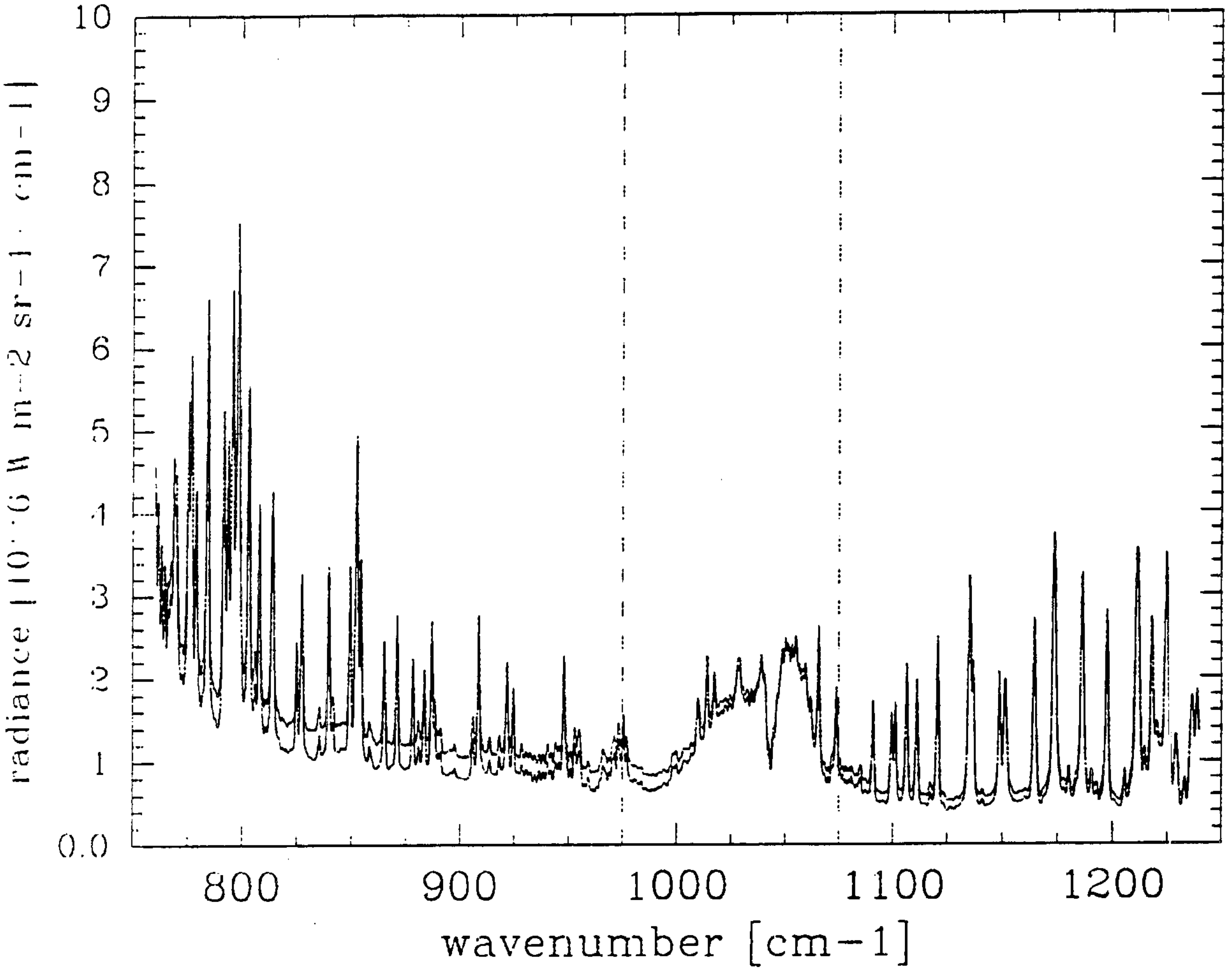

Figure 4.3a. Parsons1 clear sky (lower curve) and #60 cirrus sky radiances (upper curve).

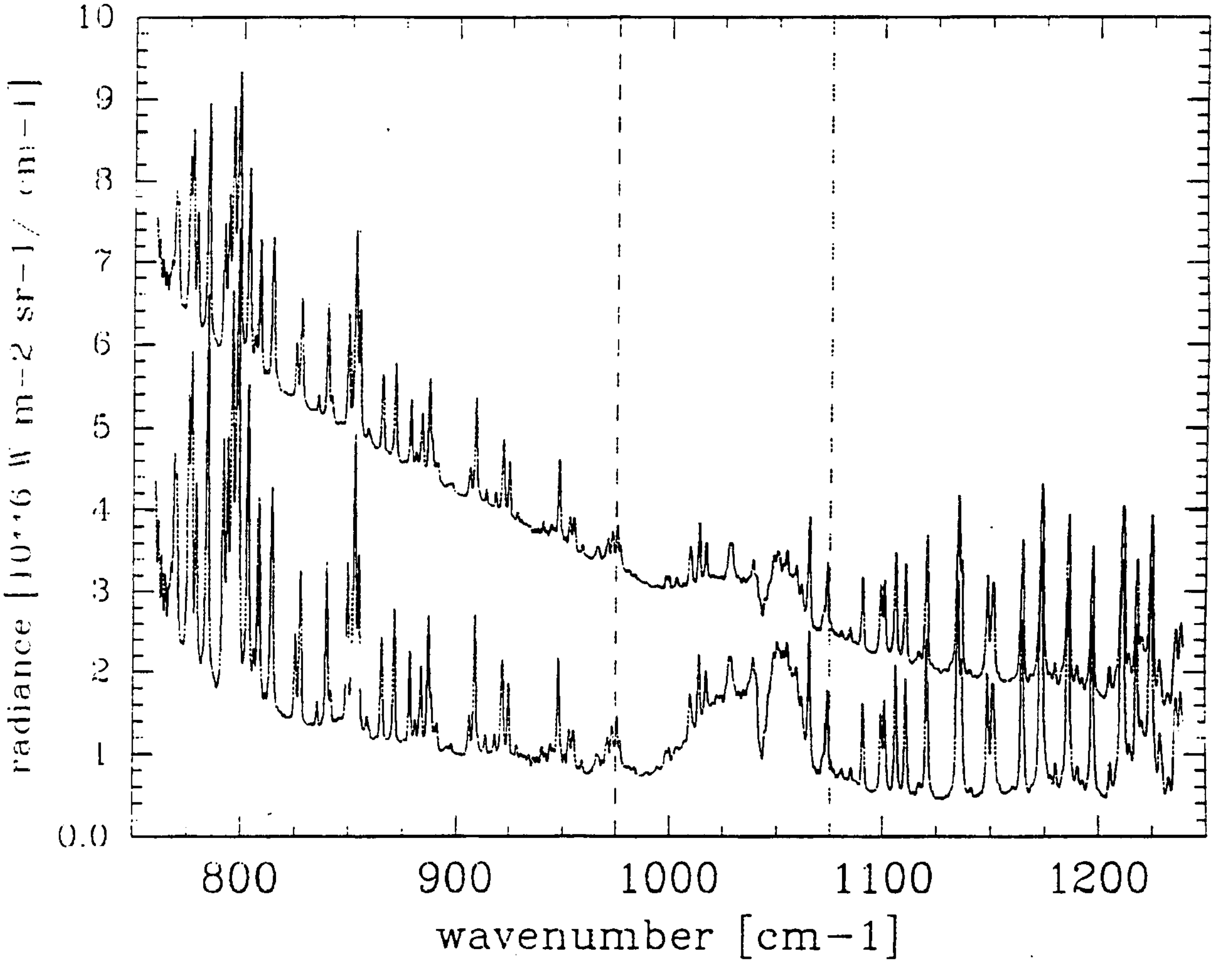

Figure 4.3b. Parsons2 clear sky (lower curve) and #12 cirrus sky radiances (upper curve).

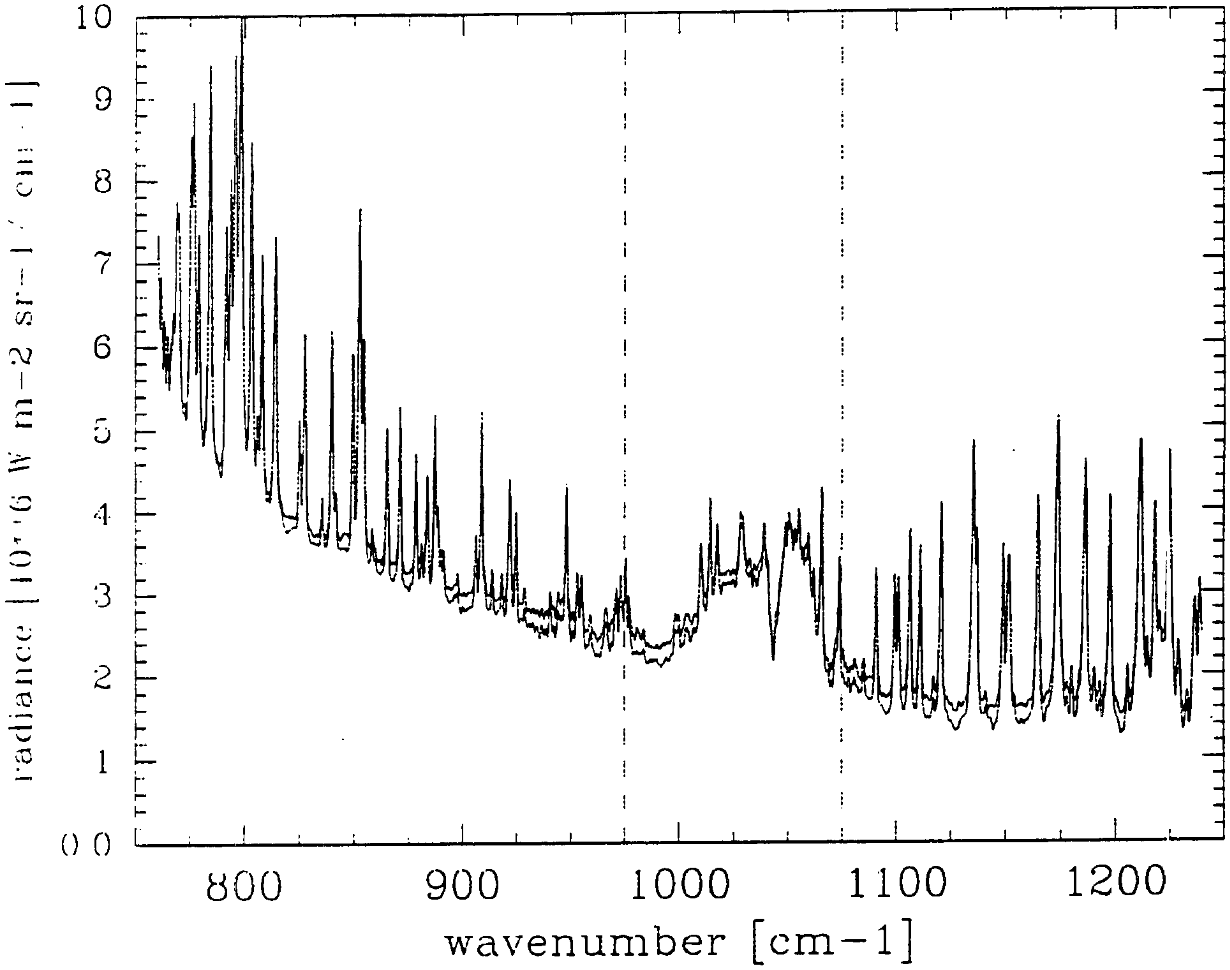

Figure 4.3c. Portsan2 clear sky (lower curve) and #75 cirrus sky radiances (upper curve).

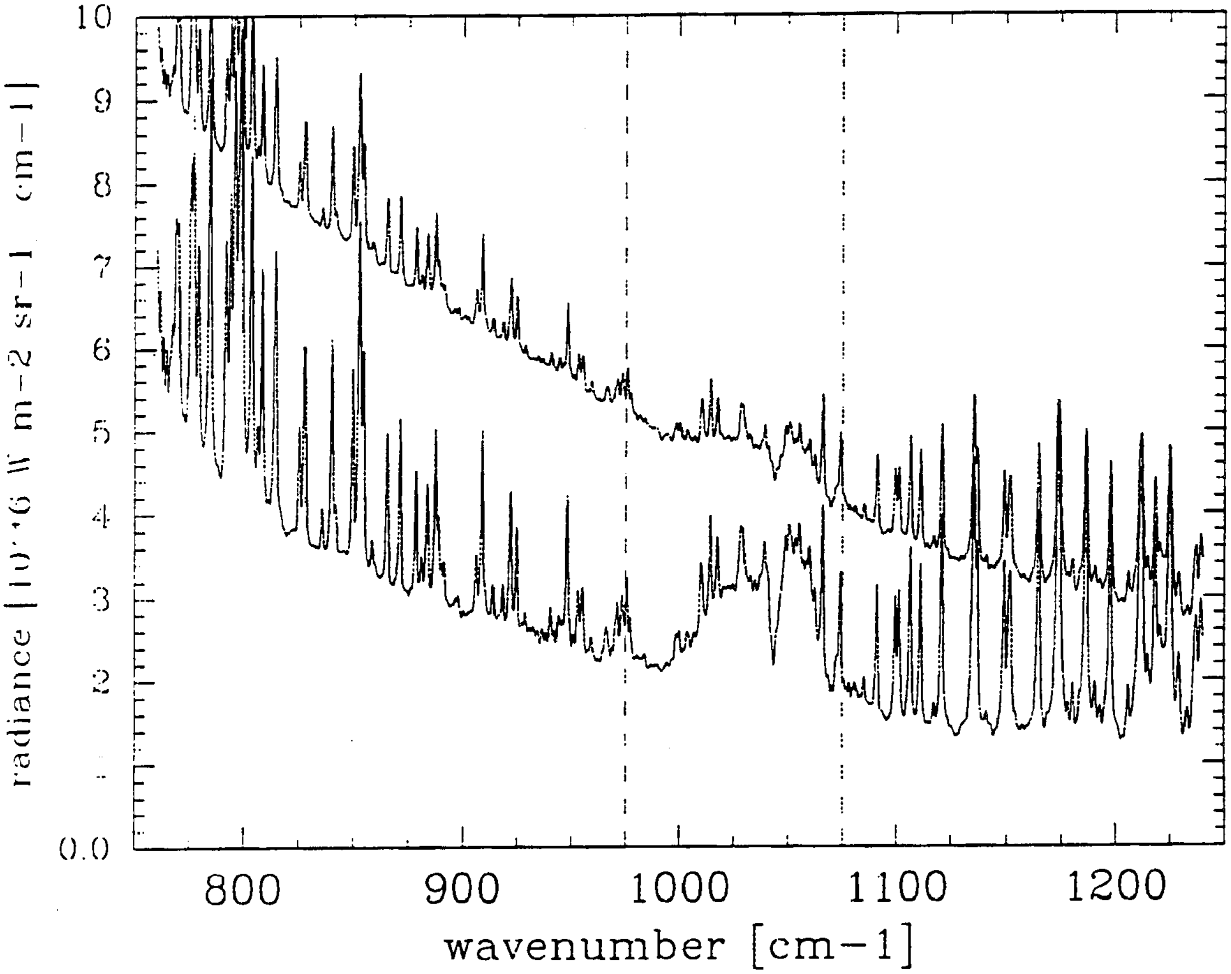

Figure 4.3d. Portsan2 clear sky (lower curve) and #39 cirrus sky radiances (upper curve).

found by dividing the values in the second column by those in the first column. These results indicate that mid-latitude cirrus have a larger relative impact upon the surface radiation budget because the clear sky radiances are smaller than the subtropical clear sky measurements; this is of course primarily a result of the greater water vapor amounts in the subtropical cases.

The following table (4.3) lists the integrated radiance values for the same spectra that are listed in table 4.2, but here the integration is performed over the 500 cm^{-1} to 2000 cm^{-1} wavenumber range and all wavenumbers within this range are included in the integration. This wavenumber range accounts for about 60% to 65% of the total radiation which is emitted at temperatures common to the atmosphere. This tabulation is offered to give a better indication of the actual impact on the total radiation reaching the surface. If the wavenumber range of integration could cover the entire wavenumber range of atmospheric emission, the integrated radiances would be larger and the percentage change would be smaller since the atmosphere is fairly opaque at wavenumbers below 500 cm^{-1}. The first column contains the 500 cm^{-1} to 2000

	radiance [$Wm^{-2}sr^{-1}$] clear sky	cirrus sky	cirrus%
Parsons1 #60	8.38	9.25	110
Parsons2 #90	8.98	12.98	145
Parsons2 #06	8.98	17.50	195
Portsan2 #75	17.53	18.54	106
Portsan3 #45	24.79	28.01	113
Portsan2 #39	17.53	26.52	151

Table 4.3. The 500-2000 cm^{-1} surface radiance values under clear sky and cirrus sky conditions and the percentage increase by the cirrus contribution over the clear sky value.

cm^{-1} integrated radiances for the clear sky spectra associated with the listed cirrus spectra. The second column lists the integrated radiance values for the listed cirrus spectra and the third column contains the percentage increase in the surface radiance due to the cirrus contribution to the total radiance. The values in the last column are found by dividing the values in the second column by those in the first column.

Table 4.3 clearly shows that, by comparison, the relative impact of cirrus cloud forcing upon a mid-latitude continental surface radiation budget is much greater than it is for a subtropical location.

Figures 4.4a and b show the contributions from the cirrus layers to the surface radiance for the spectra listed in table 4.2. As might be expected, figures 4.4a and b show the cirrus cloud forcing upon the clear sky spectra for the Parsons cases to be the greatest in the 800 cm^{-1} to 900 cm^{-1} region, but for the Portsan2 #75 spectrum, the impact was least evident in the 800 cm^{-1} to 900 cm^{-1} region. This is due to much lower sub-cirrus layer transmittance values for the Porto Santo cases compared to the Parsons cases and will be discussed further in the next section.

4.2.2. The effects of the sub-cloud layer

A comparison of the changes in radiance caused by the sub-cirrus layer and those arising from the presence of cirrus will be presented in three different ways. The first will be a comparison of the magnitude of the changes, the second a comparison of the changes in the slope of the radiance curves, and finally an analysis of the changes in the spectral valley to peak

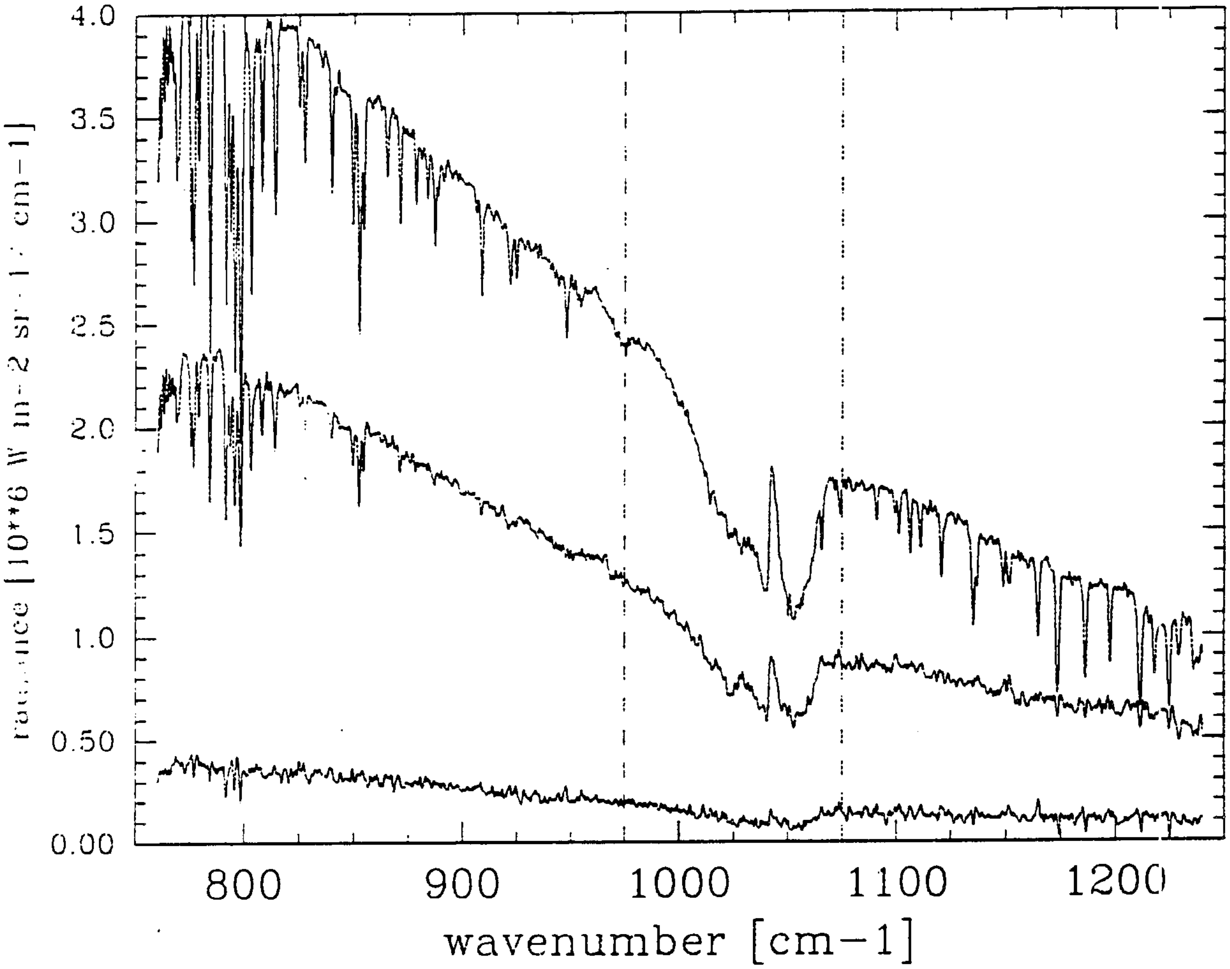

Figure 4.4a. The difference between the cirrus sky measured radiances and the associated measured clear sky radiances for the Parsons1 #60 (bottom curve), Parsons2 #90 (middle curve) and Parsons2 #06 cirrus (top curve).

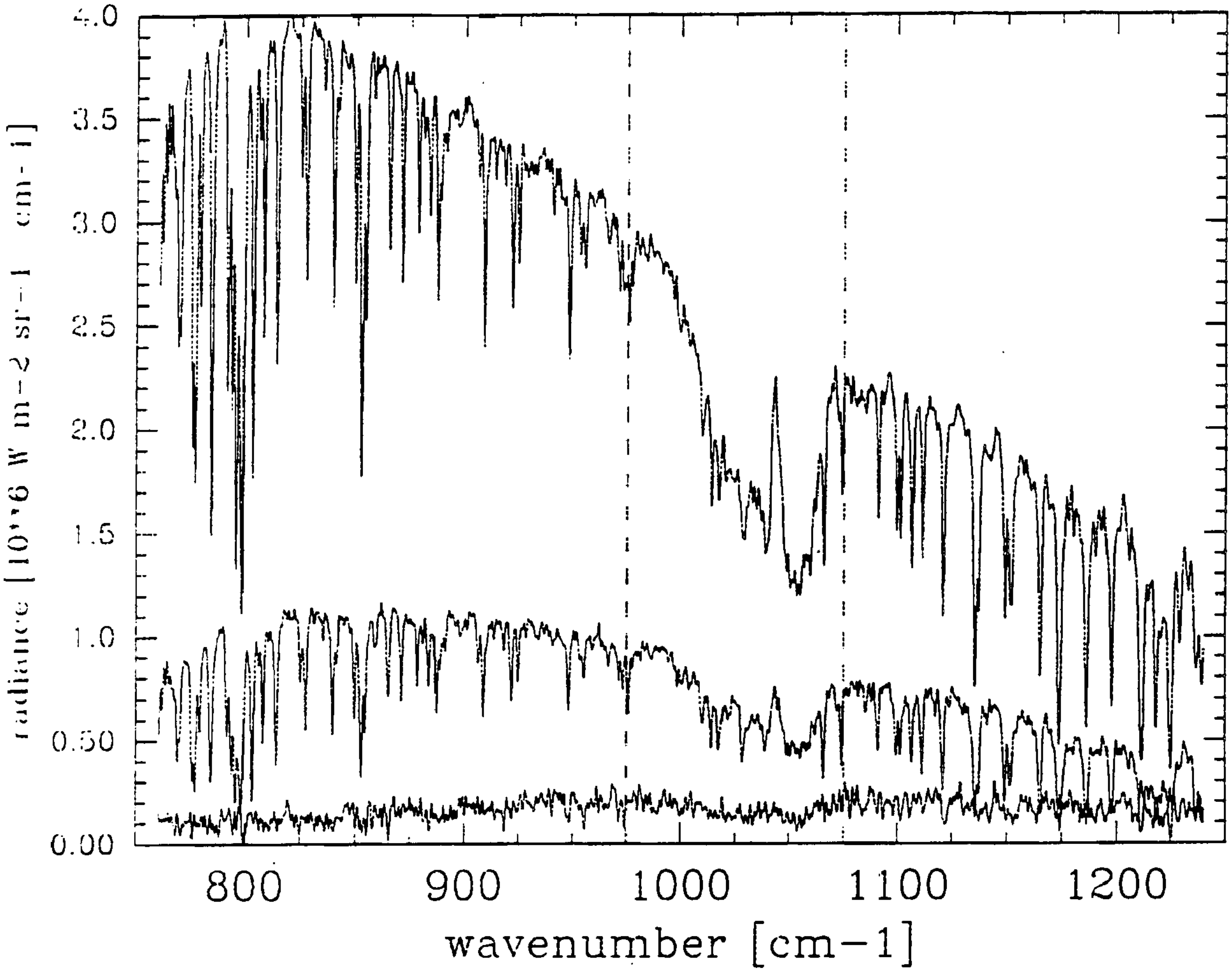

Figure 4.4b. The difference between the cirrus sky measured radiances and the associated measured clear sky radiances for the Portsan2 #75 (bottom curve), Portsan3 #45 (middle curve) and Portsan2 #39 cirrus (top curve).

line heights throughout the 800 cm^{-1} to 1200 cm^{-1} window region of the IR spectrum. These analyses will help determine the relative impact of cirrus upon surface measurements as compared to the impact caused by changes in atmospheric column water vapor and temperature structures. They will also assist in distinguishing the difference between each effect.

The first column in table 4.4 lists the differences between the clear sky integrated radiance measurements used for the three cases at each location. For example, the integrated clear sky radiance measured for the Parsons2 case was 0.50 $Wm^{-2}sr^{-1}$ greater than the integrated clear sky radiance measurement for the Parsons1 case. Accordingly, the integrated clear sky radiance measured for the Portsan3 case was 5.34 $Wm^{-2}sr^{-1}$ greater than the integrated clear sky radiance measurement for the Portsan2 case. The second and third columns list the cirrus integrated radiance contributions to the surface measurement for the spectra with the lowest and the highest emittances, respectively, that were taken during that particular period.

	radiance [$Wm^{-2}sr^{-1}$]		
	clear sky	low emit	high emit
Parsons1	---	.05	.94
Parsons2	.50	.27	8.52
Parsons3	2.38	.37	2.12
Portsan1	.36	.20	5.55
Portsan2	---	1.01	8.99
Portsan3	5.34	.30	6.10

Table 4.4. The first column contains the differences between the three clear sky integrated radiances used in this study for each location. The second and third columns show the cirrus layer contribution to the surface integrated radiance.

The cirrus integrated radiance contributions to the surface measurements for the low emittance spectra are much smaller than the values found from differencing the clear sky spectra. The highest emittance value for a cirrus layer that was measured at the Parsons site is 0.749 and for Porto Santo 0.926. With these high emittance values, the largest impact upon the surface radiance was 8.99 $Wm^{-2}sr^{-1}$. Even with only 3 clear sky spectra to compare for each site, the largest clear sky difference for Porto Santo was 5.34 $Wm^{-2}sr^{-1}$ which is quite comparable to the maximum change due to a cirrus onset.

Spectral differences from the results of the FASCODE relative humidity and temperature sensitivity tests are shown in figures 4.5 and 4.6, respectively. These figures are presented to gain insight into the impacts of temperature and water vapor changes on the appearance of the spectra. At first glance, the slopes in both of the figures appear to be quite similiar, however, there is a difference between the slopes in the 760 cm^{-1} to 800 cm^{-1} region. The main absorber at 760 cm^{-1} is CO_2, thus in the relative humidity difference spectrum the radiance values near 760 cm^{-1} are smaller than those around 780 cm^{-1}. The radiance values for the temperature difference spectrum, however, decrease over the same range. The most notable difference between these two spectra is the magnitude of the change in the line heights all across the window. In general, both temperature and water vapor change the slope of the radiance curves throughout most of the window in a similiar fashion.

Figures 4.7a and b show comparisons between the difference of the largest and smallest clear sky radiances and the difference in radiance due to the onset of cirrus that had a similiar value for the integrated radiance. These plots illustrate the differences in the impact of cirrus upon the measured spectra at the surface and of the impact upon the surface radiance arising

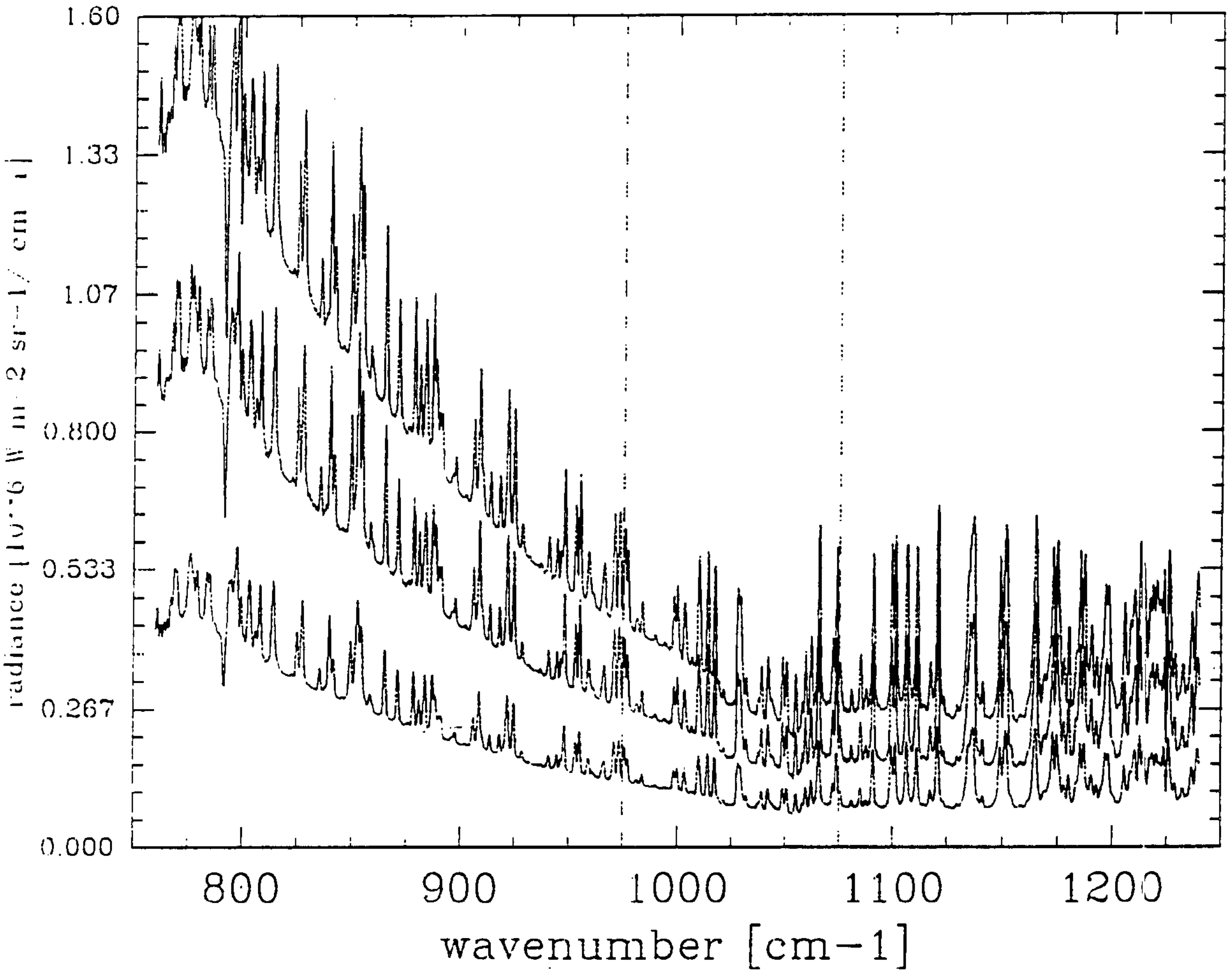

Figure 4.5. Differences between FASCODE calculated radiances using unbiased sounding data and the calculated radiances resulting from biasing the relative humidity profile by 10% (bottom curve), 20% (middle curve) and 30% (top curve).

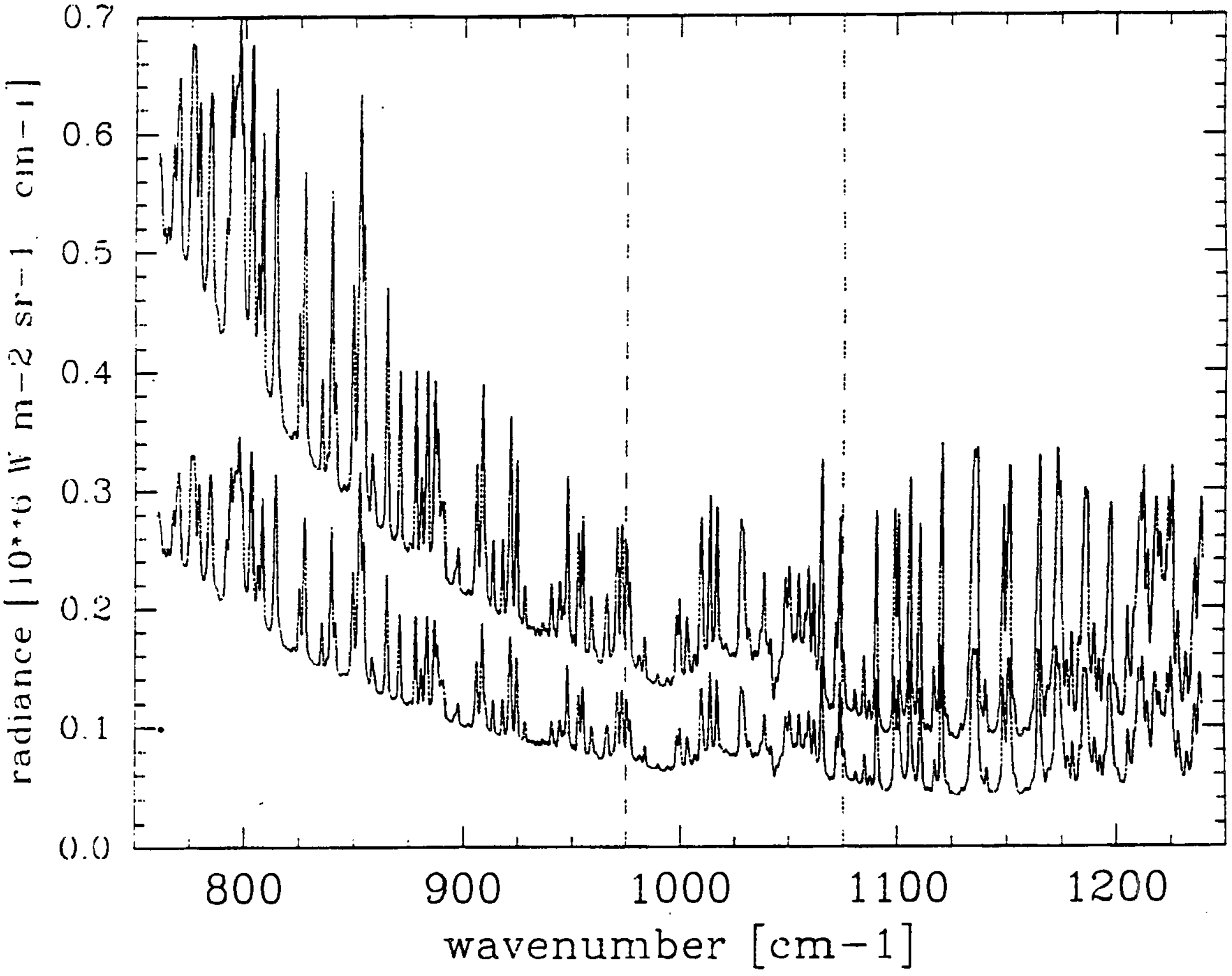

Figure 4.6. Differences between FASCODE calculated radiances using unbiased sounding data and the calculated radiances resulting from biasing the temperature profile by 1 K (lower curve), 2 K (upper curve).

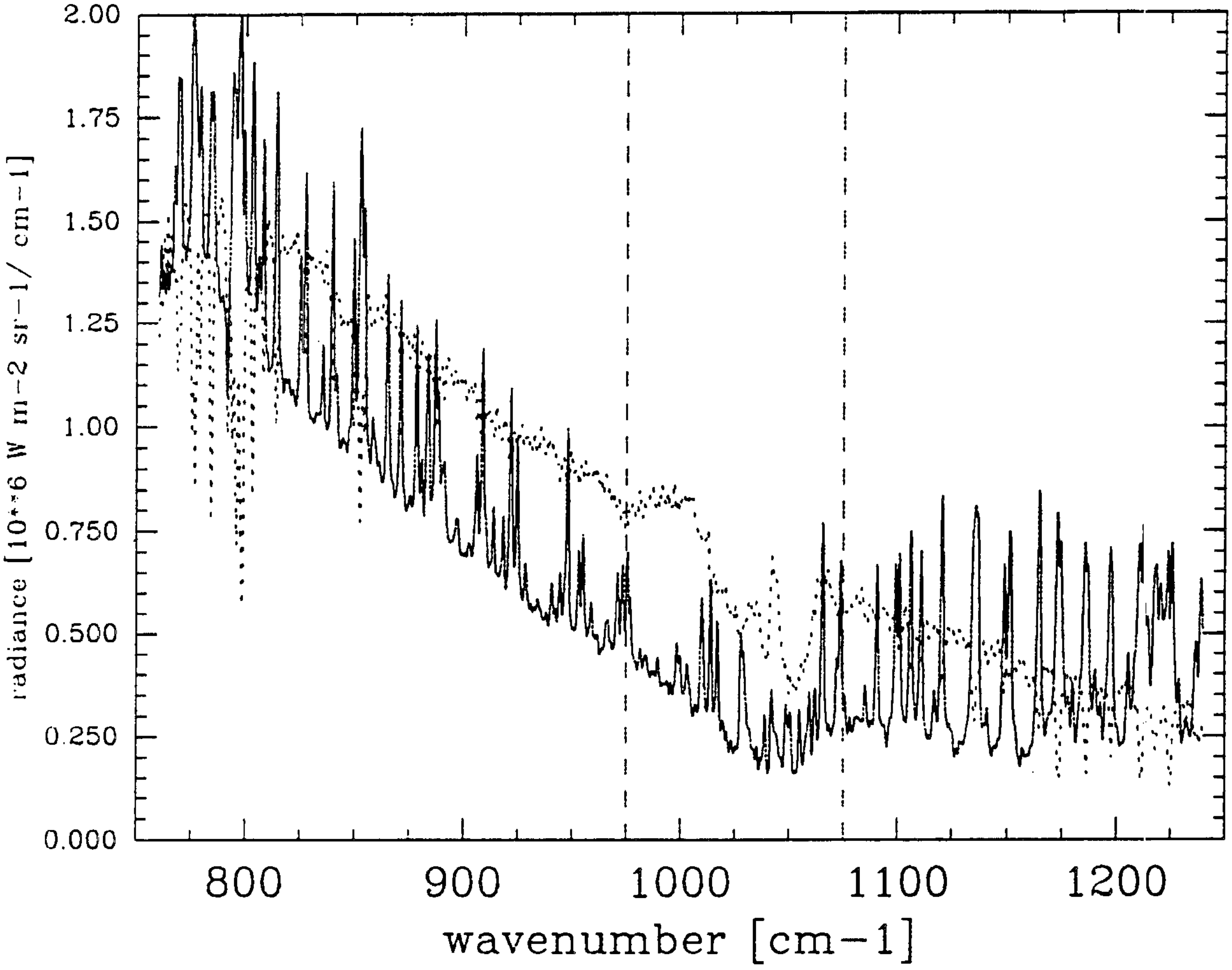

Figure 4.7a. Comparison between the difference of the largest and smallest clear sky radiances (solid line) from the Parsons data set and the difference in radiance due to the onset of cirrus (dashed line) from the Parsons data set that had a similiar value for the integrated radiance.

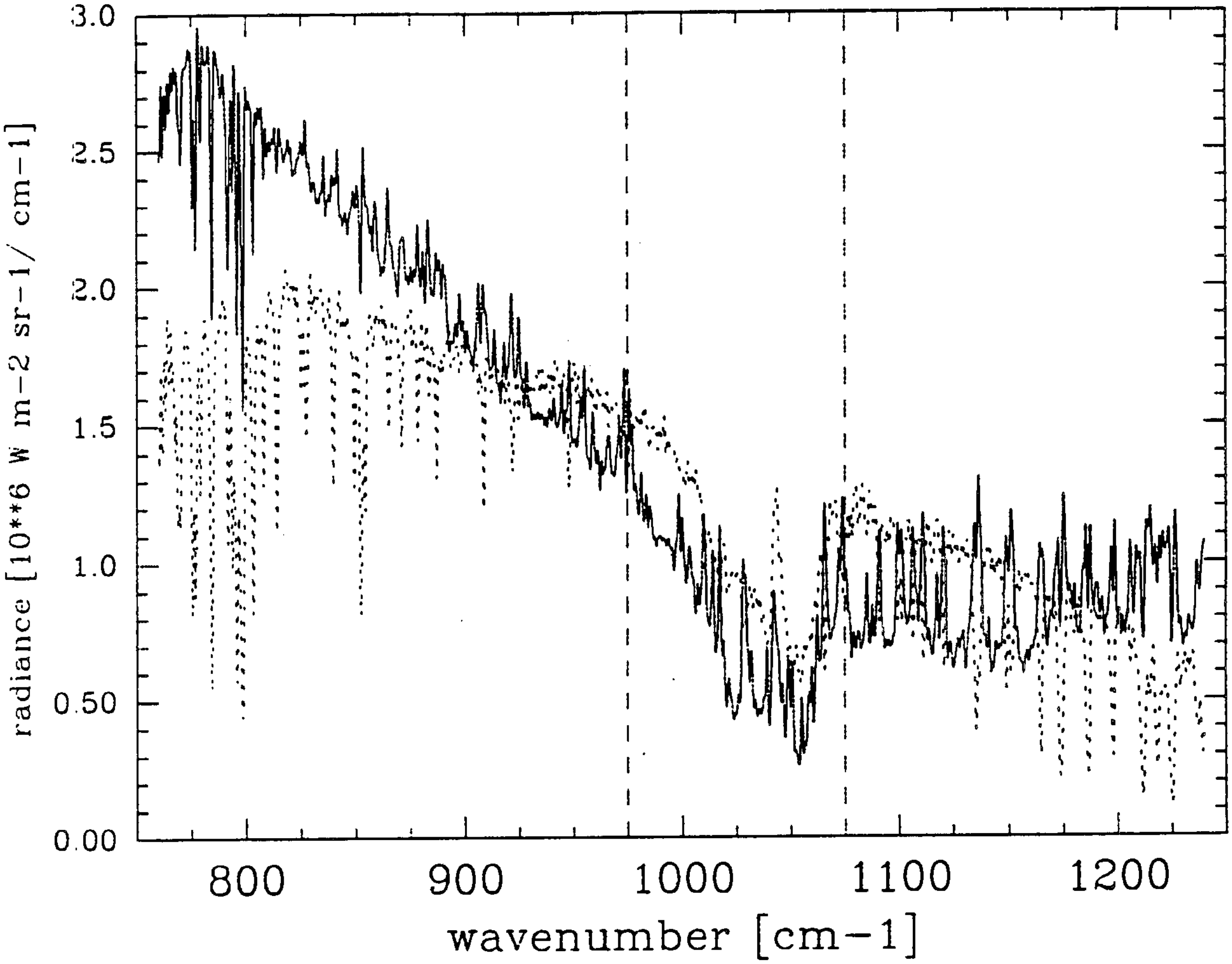

Figure 4.7b. Comparison between the difference of the largest and smallest clear sky radiances (solid line) from the Porto Santo data set and the difference in radiance due to the onset of cirrus (dashed line) from the Porto Santo data set that had a similiar value for the integrated radiance.

from changes in temperature and moisture structure.

The FASCODE tests discussed previously and shown in figures 4.5 and 4.6 indicate that the line height increased as the radiance increased for both tests. A comparison using clear sky measurements seemed to confirm these results fairly well. Several line heights were measured from the peak maximum down to the nearest valley minimum for three clear sky spectra from each of the Parsons and Porto Santo data sets are shown in table 4.5. These results show a definite increase of valley to line peak heights with increasing clear sky integrated radiance. The results for the change in the line heights following the onset of cirrus were inconclusive for both the unadjusted and the normalized cirrus sky spectra for all six cases.

	wavenumber cm^{-1}							
clear sky spec	827	865	908	948	1111	1165	1198	rad
Parsons1 #90	1.84	1.22	1.70	1.21	1.34	2.04	2.24	4.69
Parsons2 #12	1.91	1.23	1.74	1.31	1.41	2.13	2.20	5.19
Parsons3 #30	2.43	1.68	2.18	1.70	1.78	2.64	2.70	7.07
Portsan2 #84	2.41	1.73	2.17	1.82	1.93	2.60	2.69	11.50
Portsan1 #06	2.46	1.75	2.31	1.84	2.00	2.69	2.67	11.86
Portsan3 #51	2.60	2.02	2.41	2.11	2.42	2.93	2.82	16.84

Table 4.5. The line heights are given for seven wavenumbers for the six clear sky spectra used for this study are listed by increasing integrated 800 cm^{-1} to 1200 cm^{-1} clear sky radiance [$Wm^{-2}sr^{-1}$] which is given in the right hand column.

4.3. Impact of cirrus upon heating rates

An investigation into the effects of cirrus clouds upon heating rates both within the cirrus layer and throughout the subcloud layer was performed by introducing a cirrus cloud layer into the radiative transfer model MODTRAN. MODTRAN is a moderate resolution radiative transfer model developed by Spectral Sciences Inc. under contract to Phillips Laboratory at Hanscom Air Force Base. The model calculations were performed at a resolution of 1 cm^{-1} over the wavenumber range spanning from 10 cm^{-1} to 2500 cm^{-1}. This wide range of frequencies allows for approximately 99.96% of the radiation that is emitted at temperatures common to the atmosphere to be included. The cirrus cloud layer emittances were varied between 0.05 and 0.75 and were derived from normalized extinction coefficient profiles available in MODTRAN. The normalized extinction coefficient values are given at 47 wavenumbers ranging from 3.33 cm^{-1} to 50,000 cm^{-1}. Multiple scattering was not flagged, thus reflection was not included in the MODTRAN calculations.

Two soundings were used to initialize the model for this investigation. One sounding was a relatively cool and dry sounding from the Parsons data; the other was a much warmer and more moist sounding from the Porto Santo data set.

4.3.1. Parsons, Kansas case study

For the Parsons investigation, the cirrus layer was placed between 7.75 km and 9.75 km. Figure 4.8 shows the temperature and relative humidity profiles from a sonde launched at 0200Z on November 22, 1991 and also denotes the position of the cirrus layer that was introduced into the model. The effects of the moist layers and the cirrus cloud layer upon the heating rates can be seen in the following figures 4.9a and b. The heating rates shown in figures 4.9a and b were derived from MODTRAN calculations. The heating rates for the layer nearest the surface were

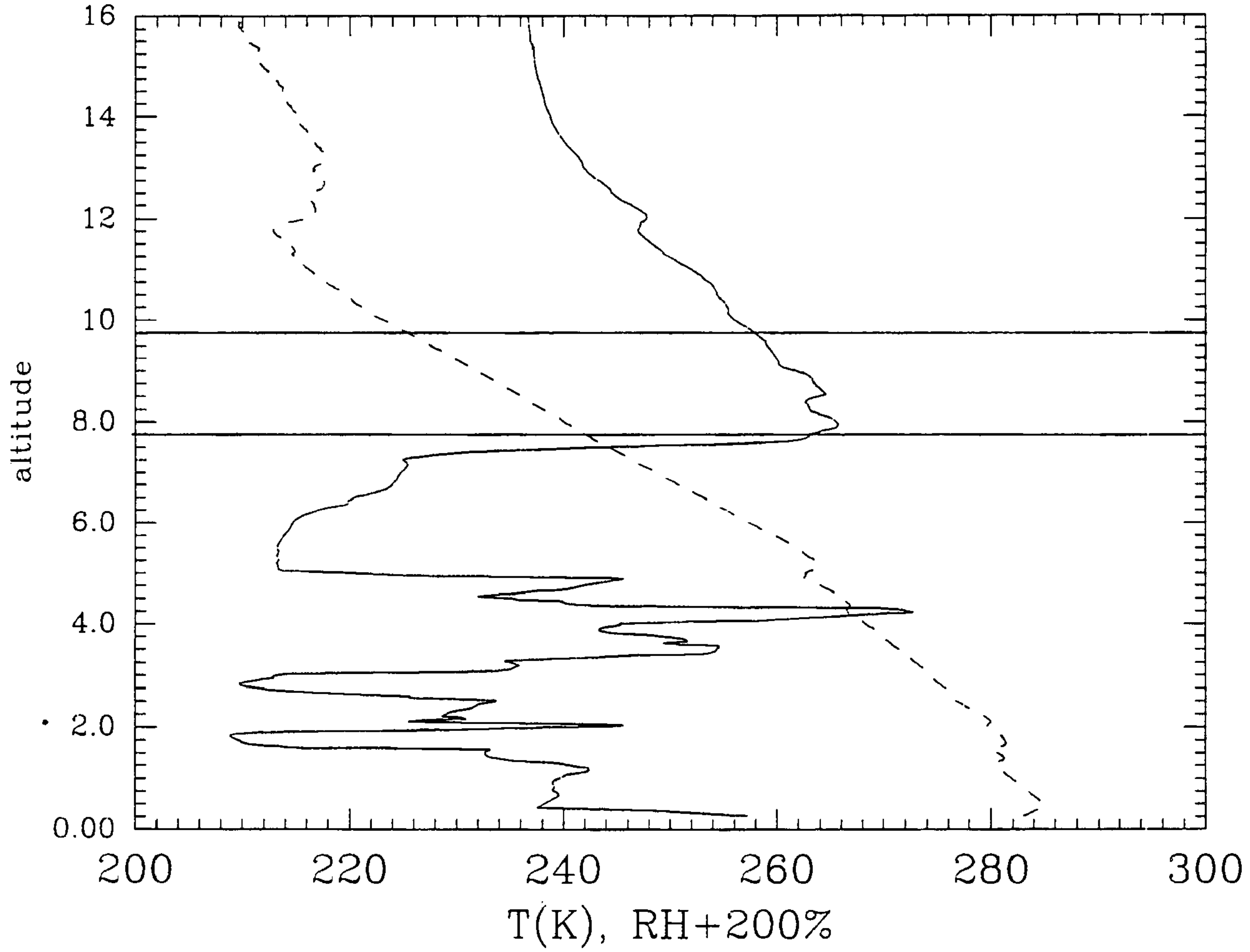

Figure 4.8. Parsons November 22, 1991 0200Z sounding data.

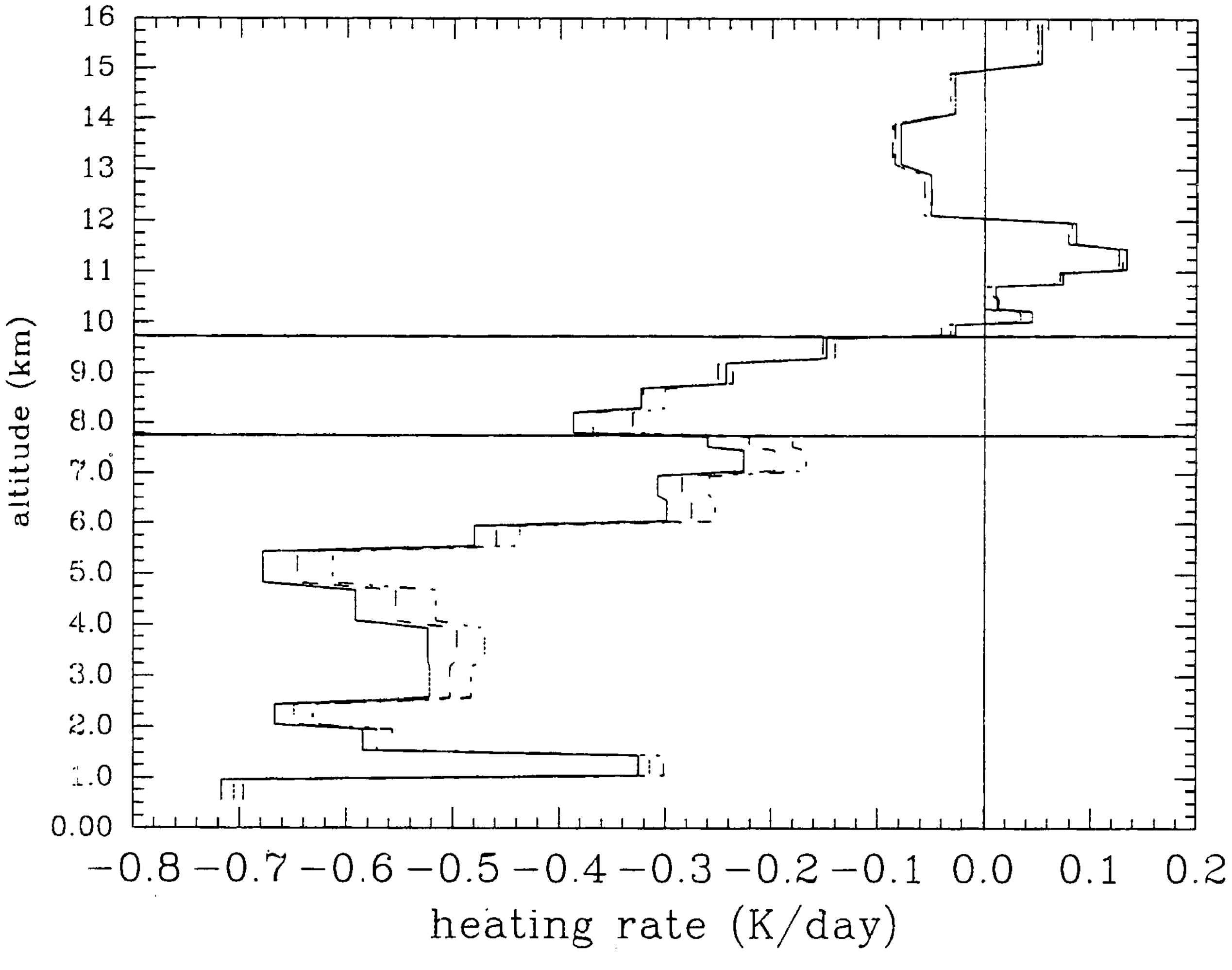

Figure 4.9a. Heating rates derived from MODTRAN calculations from the Parsons November 21, 1991 2106Z sounding data for a clear sky (solid line) and for cirrus located between 7.75 and 9.75 km with emittances of 0.1 (dashed line) and 0.2 (double-dashed line).

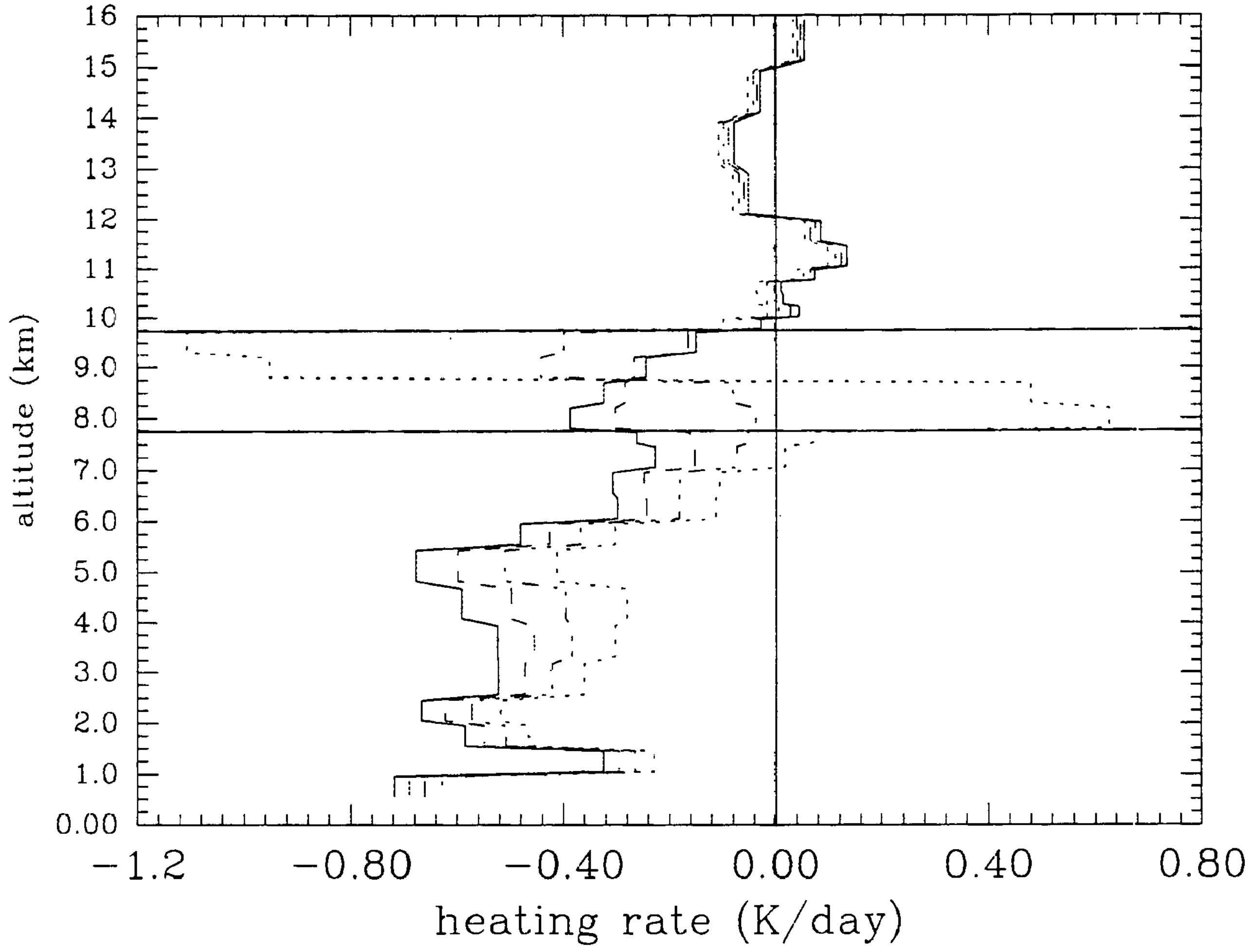

Figure 4.9b. Heating rates derived from MODTRAN calculations from the Parsons November 21, 1991 2106Z sounding data for a clear sky (solid line) and for cirrus located between 7.75 and 9.75 km with emittances of 0.25 (dashed line), 0.5 (double-dashed line) and 0.75 (dotted line).

excluded from these two figures so that values for the rest of the layers might be more easily displayed. As one might expect when considering only longwave radiation, these figures show a net cooling throughout the entire troposphere for the clear sky case. This is also true for all of the cirrus emittances up to 0.5. However, for the case of the 0.75 emittance cirrus layer, there is net warming within the lowest 1 km of the cloud layer and for 0.75 km below the layer. Note that for each cirrus case there is a net longwave energy loss for the cloud layer as a whole. The tropopause is apparent from the warming located between 11 km and 12 km.

The heating rate changes discussed throughout this section are defined as the differences between cirrus sky and clear sky heating rates under a given set of conditions. These changes indicate the impact that an approaching cirrus cloud layer would have upon the heating rates. It is also important to remember that only longwave radiation is included for the derived heating rate changes. Figures 4.10a and b show the change in the heating rates from the clear sky values due to the introduction of a cirrus layer.

In both figures it is apparent that the subcloud layers experience nearly linear heating rate increases with increasing cirrus layer emittance. All cases showed a heating rate increase for the layer adjacent to the cloudbase. Referring back to the sounding in figure 4.8, it can be seen that the largest heating rate changes are found in the most moist layers nearest the cirrus layer.

The heating rate changes in the lowest 0.5 km of the cirrus layer increased dramatically with increasing emittance. The heating rate changes in the highest 0.5 km of the cirrus layer at first increased and then decreased with increasing emittance. This is true also for the Porto Santo data set shown in the following section. This initial stabilizing tendency for the low emittance cirrus cases may have implications in cloud dynamic models since cloud layers are

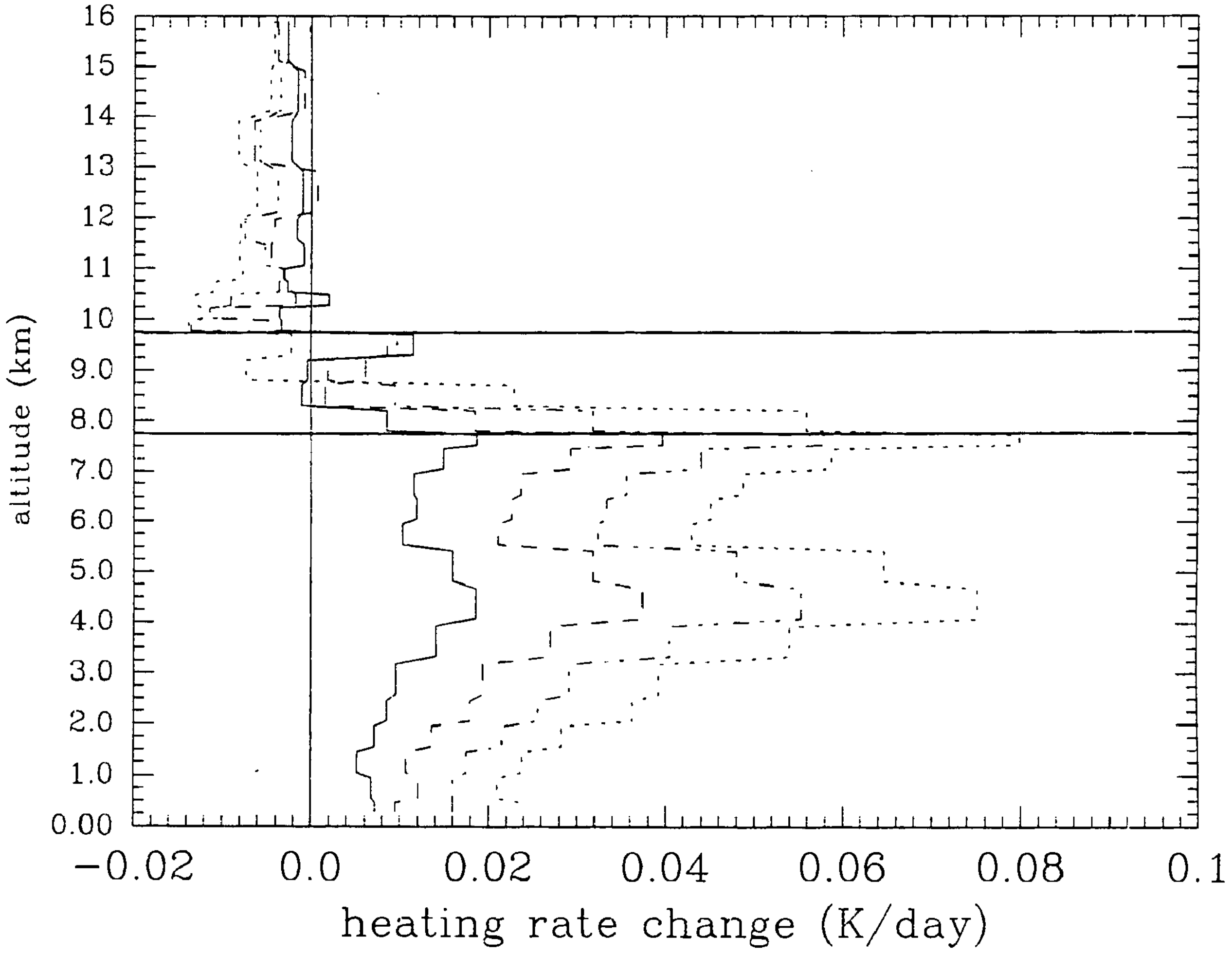

Figure 4.10a. Heating rate changes derived from MODTRAN calculations from the Parsons November 21, 1991 2106Z sounding data for cirrus located between 7.75 and 9.75 km with emittances of 0.05 (solid line), 0.1 (dashed line), 0.15 (double-dashed line) and 0.20 (dotted line).

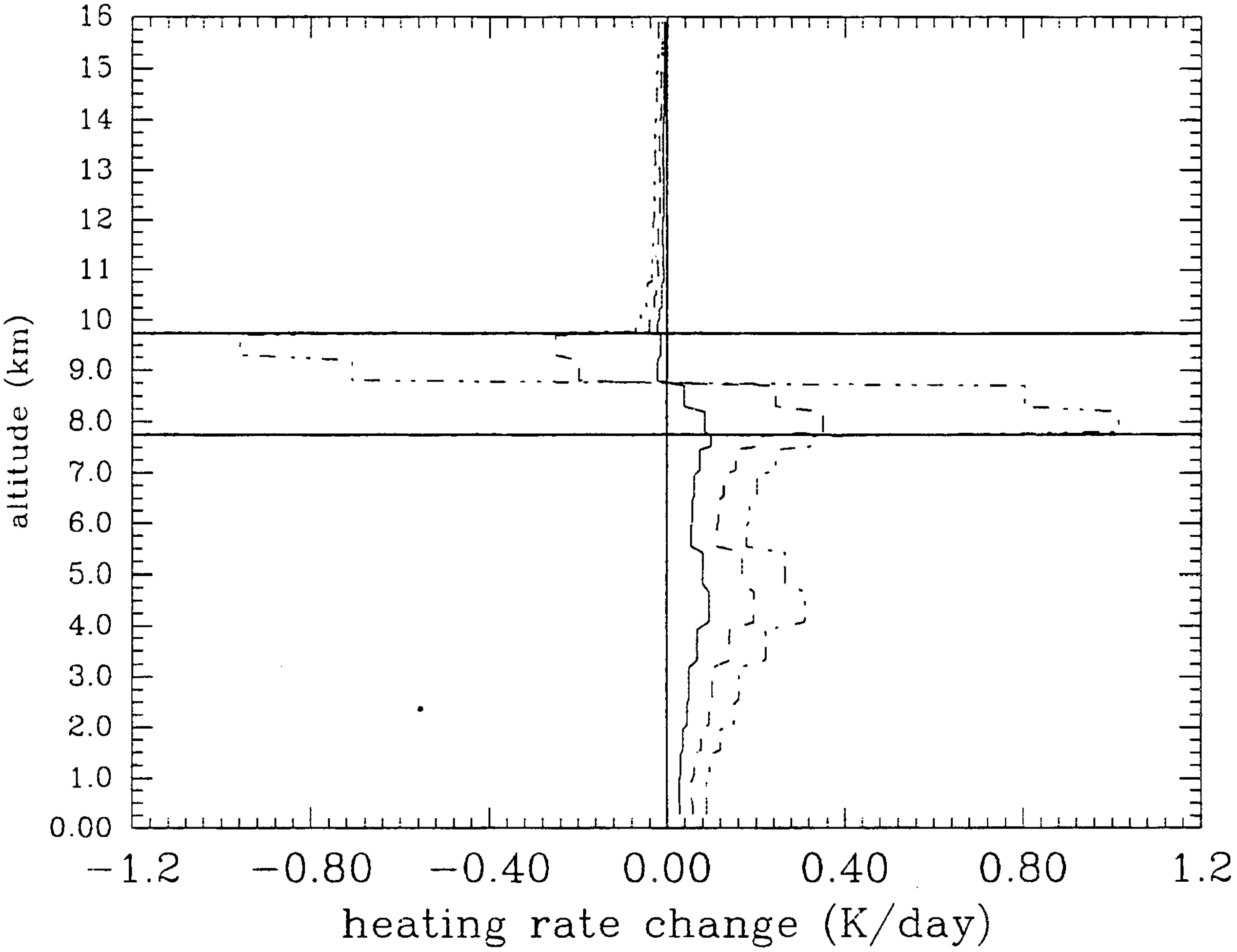

Figure 4.10b. Heating rate changes derived from MODTRAN calculations from the Parsons November 21, 1991 2106Z sounding data for cirrus located between 7.75 and 9.75 km with emittances of 0.25 (solid line), 0.5 (dashed line) and 0.75 (double-dashed line).

usually thought to always experience more cooling near the top and less cooling or even warming near the bottom due to infrared radiation. For all of the cases there is a heat loss for the layer adjacent to the cloudtop when compared to the clear sky heating rates.

Figures 4.11a and b show the results from two of four tests which were performed in an attempt to determine the sensitivity of the heating rate changes within the cirrus layer to various perturbations on the sounding. All of these tests were done with the cirrus emittance set at the value 0.1. Plotted in figures 4.11a and b are the heating rate changes for the unaltered sounding versus the heating rate changes found for various perturbations on the atmospheric sounding.

The impact of a 10 K increase in the surface temperature upon the heating rate changes is seen in figure 4.11a. Although this impact upon the heating rates for layers near the surface would obviously be large, its effect upon the heating rate changes (the cirrus sky heating rates minus the clear sky heating rates) in the subcloud layers was negligible. The impact of this surface temperature increase upon the cirrus layer, however, was large.

Figure 4.11b shows the dramatic change in the heating rate structure within the cirrus layer which occurred when the temperature structure within the cirrus layer was forced to be isothermal. This illustrates the impact that cirrus cloud layer lapse rates have upon the distribution of radiative heating. Again, little effect upon the heating rate changes is seen outside the cloud layer.

Two tests (not shown) were performed to assess the effects of water vapor and ozone. First, all ozone was removed and second all water vapor above the cirrus cloud layer was deleted. Neither of these played a significant role in affecting either the heating rates or the heating rate changes within the cirrus layer or the subcloud layer.

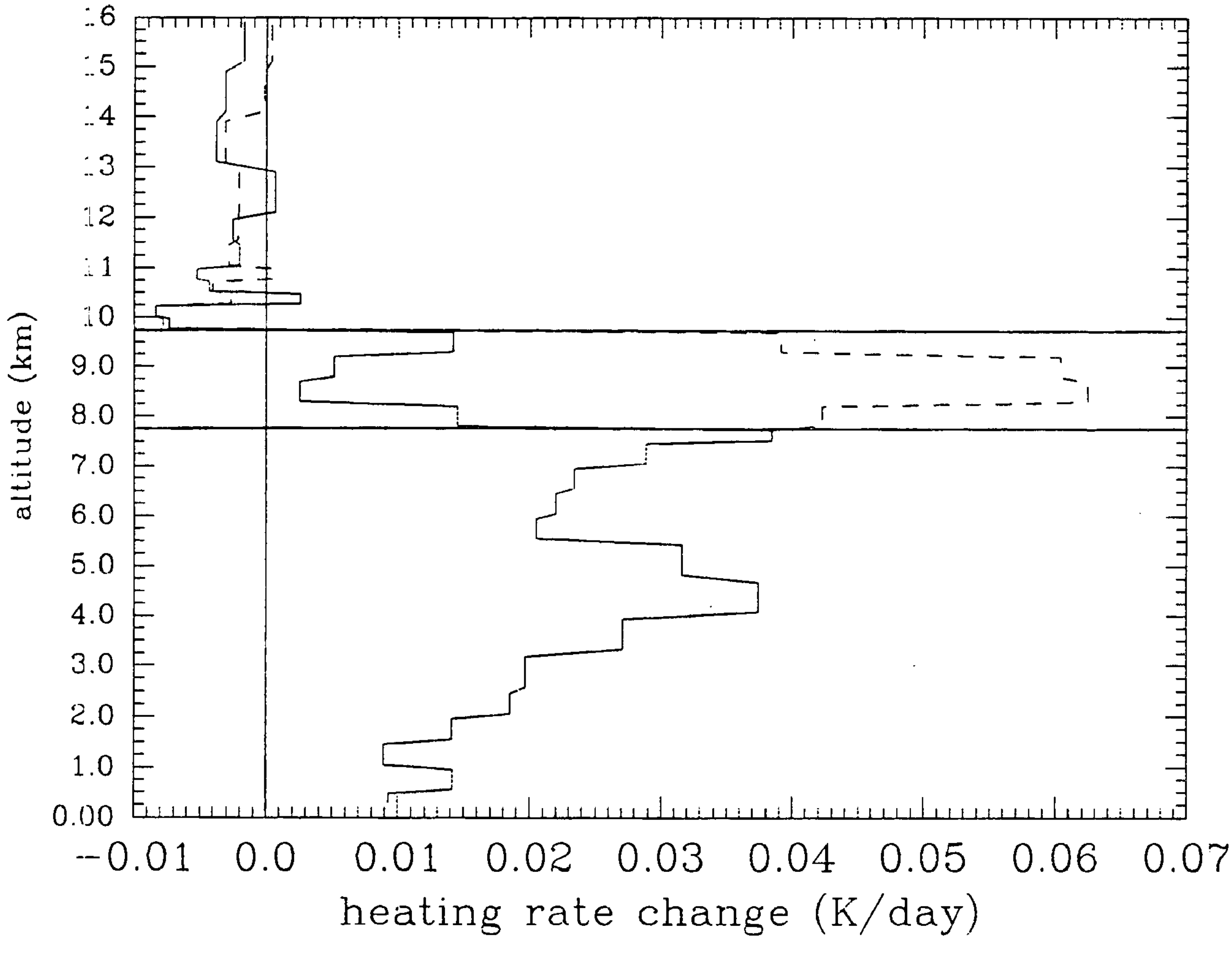

Figure 4.11a. Heating rates derived from MODTRAN calculations with a 0.1 emittance cirrus cloud layer from the Parsons November 21, 1991 2106Z sounding data (solid line) and the derived heating rates given a 10 K warmer surface temperature (dashed line).

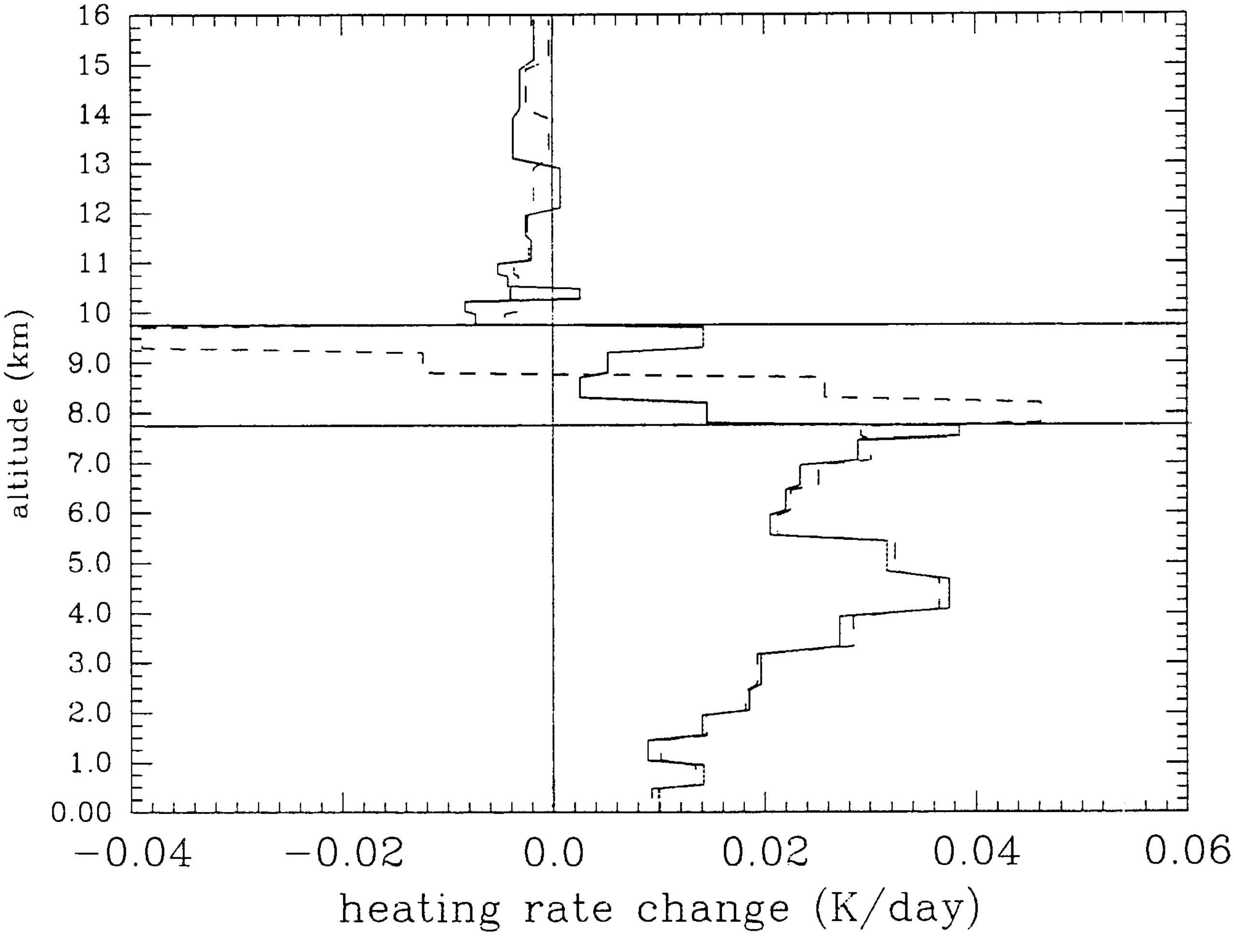

Figure 4.11b. Heating rates derived from MODTRAN calculations with a 0.1 emittance cirrus cloud layer from the Parsons November 21, 1991 2106Z sounding data (solid line) and the derived heating rates given an isothermal cirrus cloud layer (dashed line).

4.3.2. Porto Santo case study

For the Porto Santo investigation, the cirrus layer was placed between 9.5 km and 11.5 km. Figure 4.12 shows the temperature and relative humidity profiles from a sonde launched at 1139Z on June 27, 1992 and also denotes the position of the cirrus layer that was introduced into the model. The cirrus properties introduced into the model for this investigation are the same as those used for the Parsons, Kansas study except for the cloud placement which was 1.75 km higher. Also, the cloudbase and cloudtop temperatures of the cirrus clouds for this case study are 237 K and 221 K, respectively, each being 5 K colder than the cirrus for the Parsons case study. Figures 4.13a and b show the derived heating rates.

There is one major difference between the heating rates shown here in figures 4.13a and b and those shown for the Parsons case study in figures 4.9a and b. For all of the Parsons cirrus layers, there is a net longwave energy loss for the cloud layer as a whole. This is also true to a lesser degree for the Porto Santo cirrus layers with emittances less than or equal to 0.25. However, the Porto Santo cirrus with emittance values of 0.50 and 0.75 actually show a net longwave energy gain when considering the cloud layer as a whole. The Porto Santo subcloud layer, however, experienced more cooling than did the Parsons subcloud layer.

The net radiation for a cirrus layer may be expressed as:

$$net\ radiation = E_B \sigma T_B^4 - 2E_C \sigma T_C^4 + E_A \sigma T_A^4, \qquad (4.1)$$

where, the three right hand side terms from left to right represent the subcloud layer (subscript

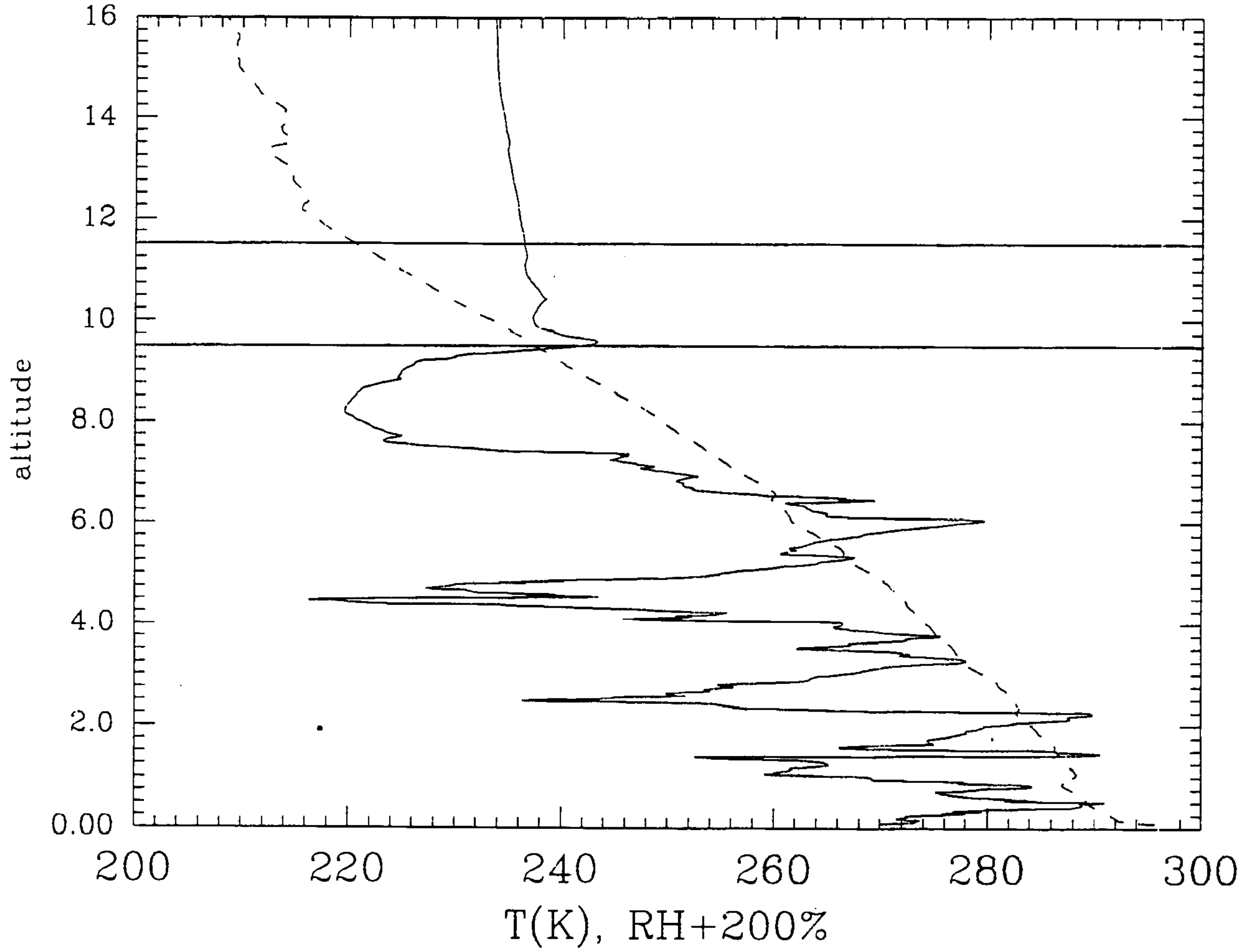

Figure 4.12. Porto Santo June 27, 1992 1139Z sounding data.

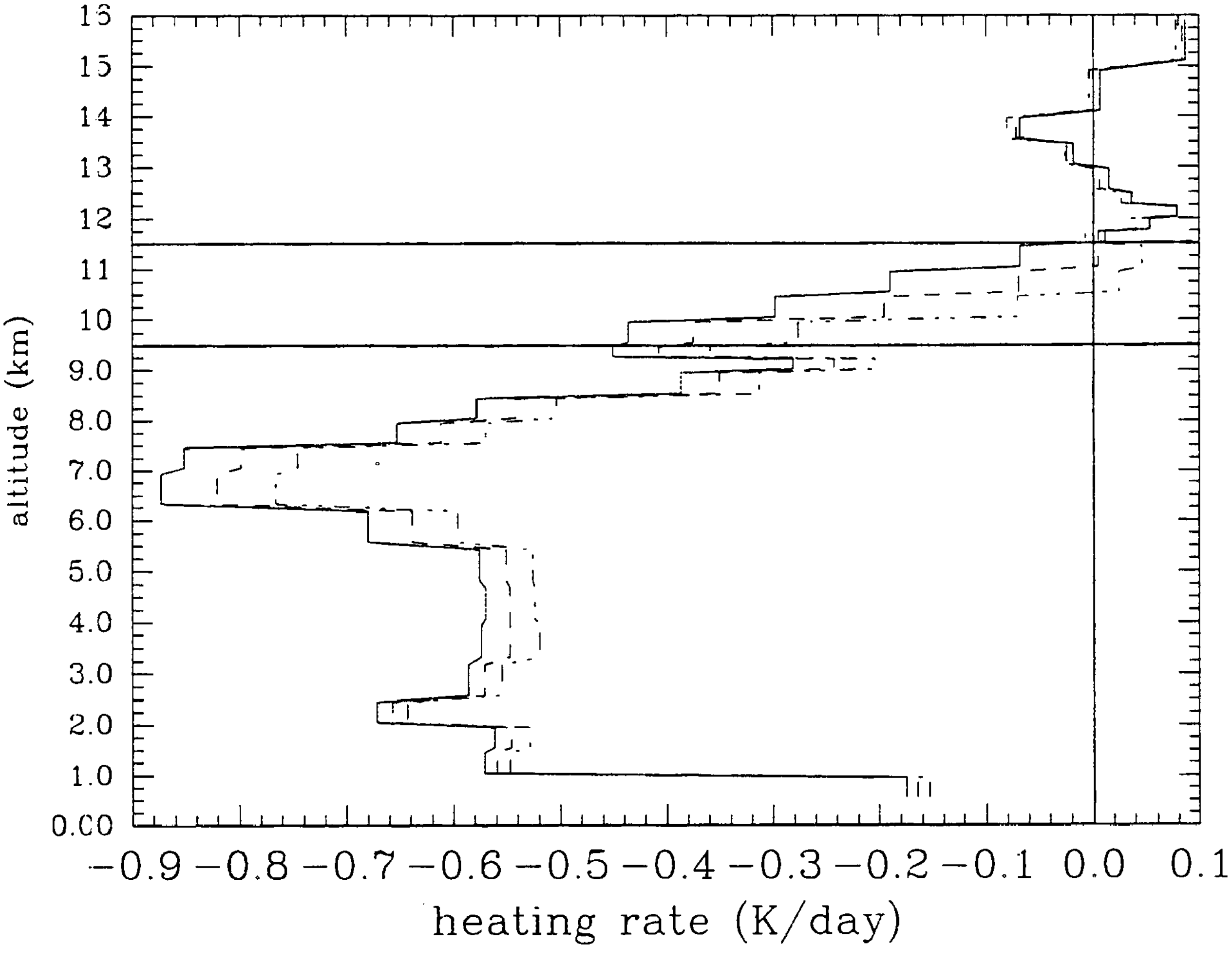

Figure 4.13a. Heating rates derived from MODTRAN calculations from the Porto Santo June 27, 1992 1139Z sounding data for a clear sky (solid line) and for cirrus located between 9.5 and 11.5 km with emittances of 0.1 (dashed line) and 0.2 (double-dashed line).

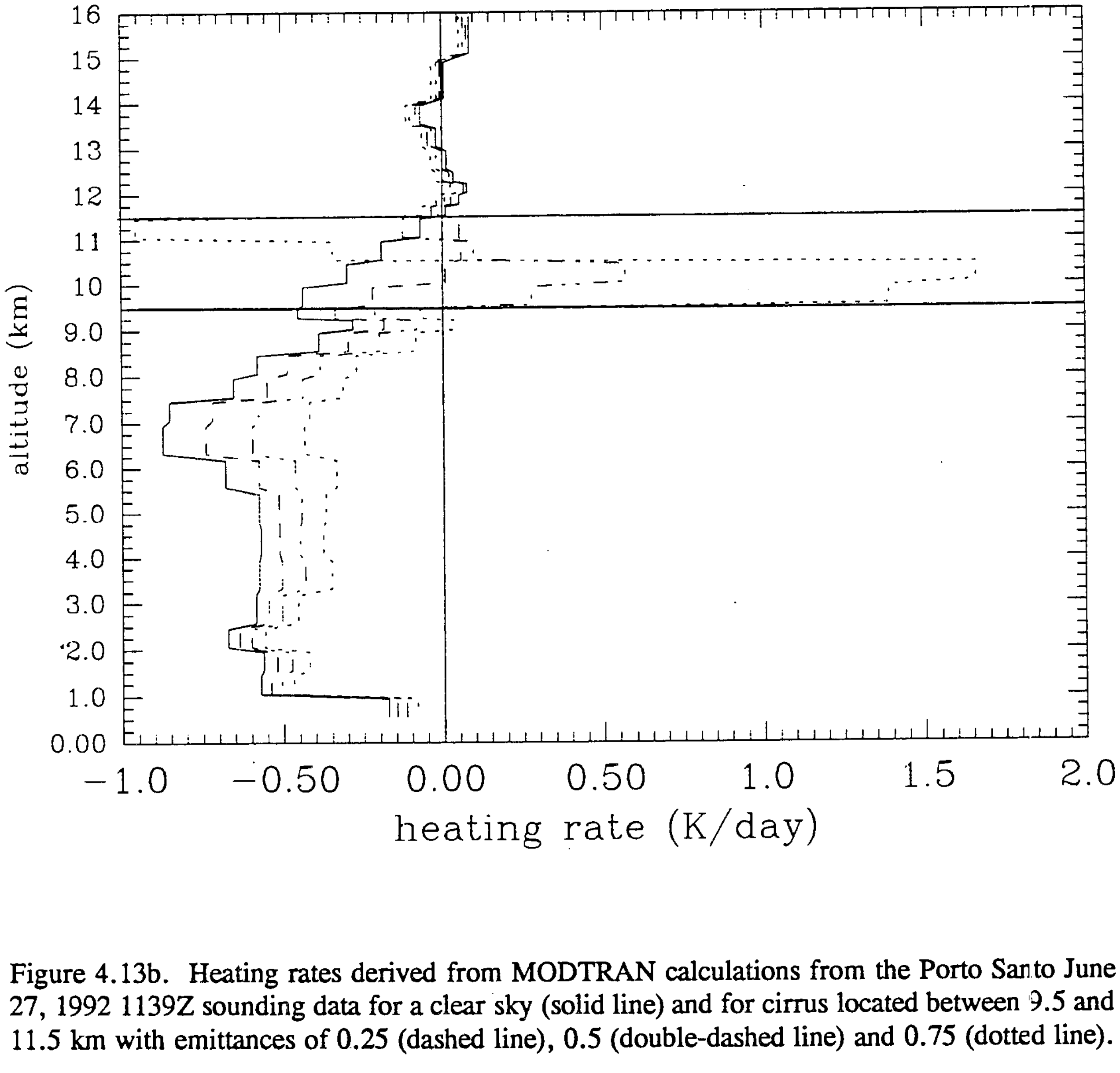

Figure 4.13b. Heating rates derived from MODTRAN calculations from the Porto Santo June 27, 1992 1139Z sounding data for a clear sky (solid line) and for cirrus located between 9.5 and 11.5 km with emittances of 0.25 (dashed line), 0.5 (double-dashed line) and 0.75 (dotted line).

B), the cirrus layer (subscript C) and the atmosphere above the cirrus cloud layer (subscript A), respectively, where E is emittance, T is temperature and σ is the Stephan-Boltzman constant. Since the atmospheric emission above the cirrus cloud layer is very small (see table 2.1), equation (4.1) may be rewritten as:

$$net\ radiation = E_B \sigma T_B^4 - 2E_C \sigma T_C^4. \tag{4.2}$$

The temperature and moisture profiles and the location of the cirrus layer was different for the Porto Santo case study than it was for the Parsons case study, but the same set of emittances were used for both. To eliminate the cirrus layer emittance from the previous equation, a new variable may be defined as:

$$\alpha = \frac{2E_C}{E_B}, \tag{4.3}$$

and combining with equation (4.2) yields:

$$net\ radiation = E_B \sigma [T_B^4 - \alpha T_C^4]. \tag{4.4}$$

It is apparent from this equation that when a subcloud layer becomes warmer or a cirrus cloud layer becomes colder that the net radiation for the cirrus layer will become less negative/more positive and thus the heating rates would change to less cooling/more warming. Less cooling/more heating would also occur for a more emissive (less transparent) subcloud layer in the previous equation. This concurs with the above observations; when compared to the Parsons cirrus case, the Porto Santo subcloud layer was warmer and more emissive while the cirrus layer was colder.

Two tests were performed using MODTRAN in an attempt to gain to further understand why the Parsons cirrus and the Porto Santo cirrus might be different. For these tests, only the temperatures from the Porto Santo sounding data used to initialize the model were varied throughout either the cirrus cloud layer or the subcloud layer. For the first test, the subcloud layer temperature structure was held constant while the cirrus cloud layer temperature structure was biased both warmer and then cooler. For the second test, the cirrus cloud layer temperature structure was held constant while the subcloud layer temperature structure was biased warmer and cooler.

Three conclusions may be drawn from the heating rate test results. First, under clear sky conditions, a warmer atmosphere will experience more cooling/less heating than will a colder atmosphere. Second, under cirrus sky conditions, a warmer subcloud layer will experience more cooling than will a colder subcloud layer and but will result in less cooling/more heating within the cirrus layer. Third, a warmer cirrus cloud layer will experience more cooling/less heating than will a colder cirrus layer, but will result in less cooling in the subcloud layer.

This is consistent with the results shown in figures 4.13 since first of all, the Porto Santo cirrus layer temperatures were 5 K colder than the Parsons cirrus and secondly, the Porto Santo subcloud layer was warmer than the Parsons subcloud layer.

Figures 4.14a and b show the change in the heating rates from the clear sky values due to the introduction of a cirrus layer. The data presented in these figures contain most of the same characteristics that were discussed for the Parsons case study. Again, the heating rate changes in the lowest 0.5 km of the cirrus layer increased dramatically with increasing emittance while the heating rate changes in the highest 0.5 km of the cirrus layer at first increased and then decreased with increasing emittance (compare to figures 4.10a and b). The magnitudes of the heating rate changes within the cirrus layer and throughout the subcloud layer for the Porto Santo cirrus are larger than for the Parsons cirrus.

Three conclusions may be drawn from the heating rate change test results. First, the presence of a cirrus cloud will result in less cooling/more warming within the subcloud layer, i.e., positive heating rate changes, whereas the cirrus layer may experience either positive or negative heating rate changes depending on the emittance and the location within the cloud layer. Second, a warmer subcloud layer will experience a larger positive heating rate change within the subcloud layers nearest cloudbase than will a colder subcloud layer; also, the cloud layer will experience a larger positive/smaller negative heating rate change. Because the warmer subcloud layer under clear sky conditions experiences more cooling than a colder subcloud layer, the presence of a cirrus layer results in a larger positive heating rate change, i.e., a shift towards less cooling. Third, a warmer cirrus cloud layer will experience a smaller positive/larger negative heating rate change within the cloud layer than will a colder cirrus layer. Again, in comparison to the Parsons case, the subcloud layer is warmer and the cirrus cloud layer is cooler and so this is also consistent with the tests.

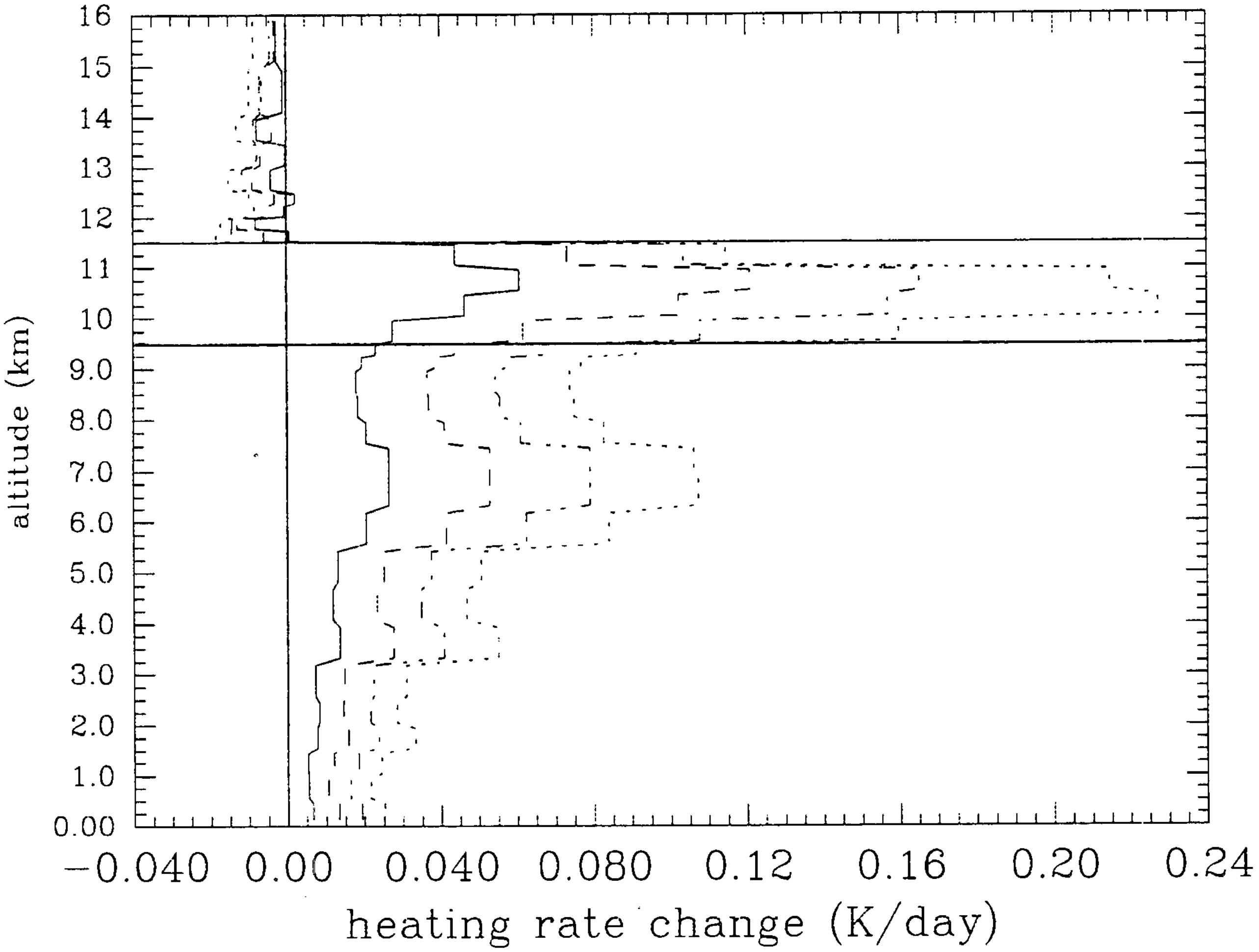

Figure 4.14a. Heating rate changes derived from MODTRAN calculations from the Porto Santo June 27, 1992 1139Z sounding data for a clear sky (solid line) and for cirrus located between 9.5 and 11.5 km with emittances of 0.1 (dashed line) and 0.2 (double-dashed line).

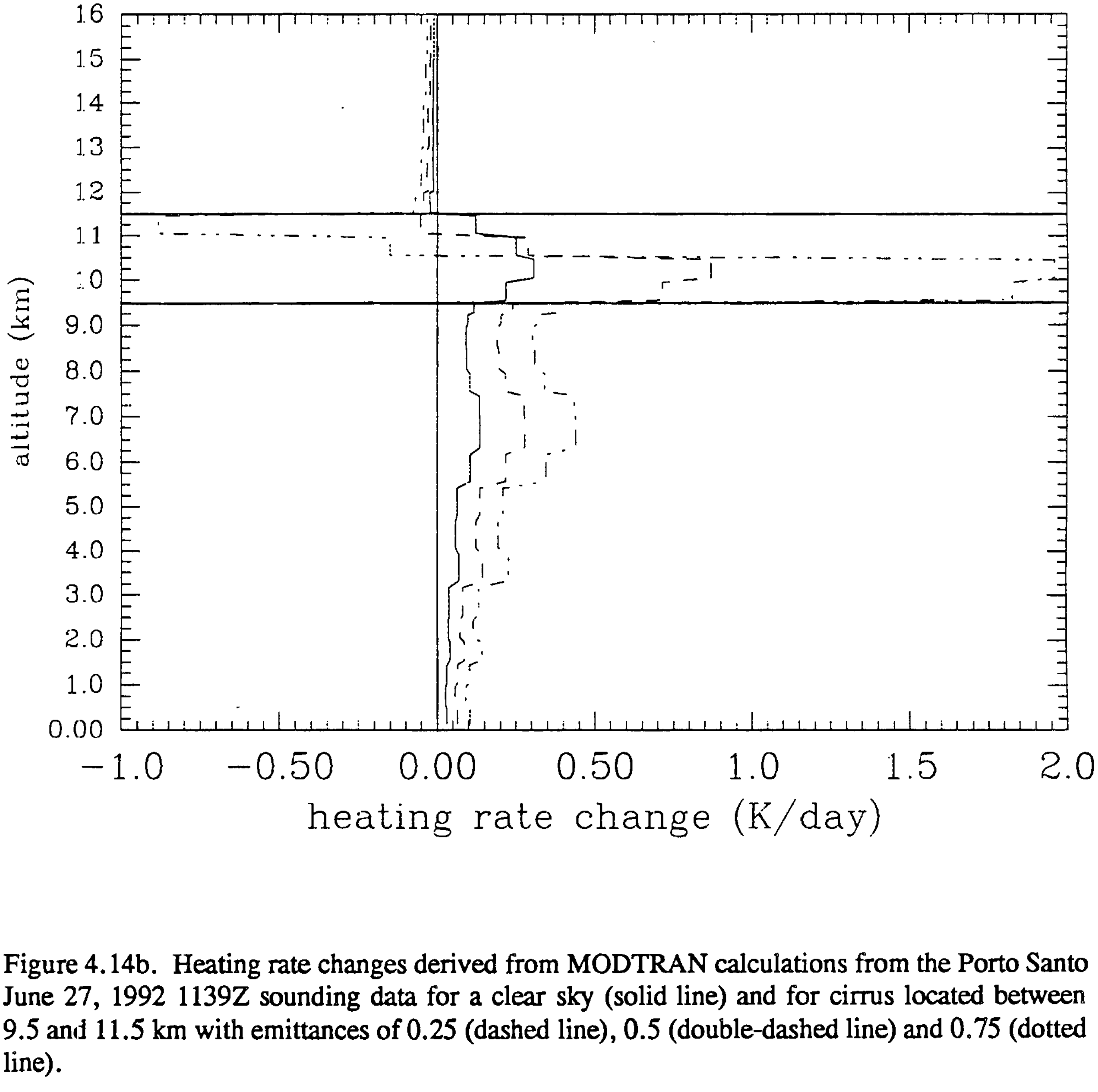

Figure 4.14b. Heating rate changes derived from MODTRAN calculations from the Porto Santo June 27, 1992 1139Z sounding data for a clear sky (solid line) and for cirrus located between 9.5 and 11.5 km with emittances of 0.25 (dashed line), 0.5 (double-dashed line) and 0.75 (dotted line).

5. SUMMARY AND CONCLUSIONS

This study of the infrared radiometric properties of cirrus clouds was performed using data from the Nov-Dec 1991 Parsons, Kansas field deployment phase and from the June 1992 Porto Santo, Madeira field deployment phase. Interferometric surface measurements, sonde data, lidar returns and FASCODE III model calculations were utilized in the analysis. The thicknesses of the cirrus layers varied from a few meters to 4.3 km for the Parsons data set and ranged from 0.3 km to 3 km for the Porto Santo data.

The emittance values derived for the subtropical cirrus observed at the Porto Santo site were generally greater than those found for the mid-latitude cirrus at Parsons. The magnitude of the emittances within the 800-1200 cm^{-1} atmospheric window region for observed cirrus at Parsons ranged from a very transparent 0.006 to fairly opaque 0.749 while the range for the Porto Santo cirrus was from 0.029 to 0.926. This wide range of values is consistent with those reported in previous cirrus studies. According to Hunt (1973), the maximum possible emittance that a cirrus layer can have in the 8-13 μm (770-1250 cm^{-1}) window is in the 0.50 to 0.70 range while Liou (1974) stated that a completely opaque cirrus layer can have an emittance in the 800-1200 cm^{-1} wavenumber range as high as 0.95; Allen (1971) derived cirrus emittance values for the as high as 1.0 in the 8-13 μm region. Griffith, et al. (1980) also derived cirrus emittance values as high as 1.0 for the 4-50 μm wavelength range. The importance of including reflectance for the inference of these cirrus cloud layer parameters was shown. Ignoring reflection, two of the derived Parsons cirrus emittance values were 0.102 and 0.823 but the derived emittances for these same two cases with the inclusion of reflectance were found to be

0.072 and 0.749, respectively.

The data for the higher altitude cirrus (7-10 km) from this study yielded a mean emittance value of 0.09 while the lower cirrus (5.5-7 km) yielded a value of 0.66 for the mean emittance. Cox (1971) reported that for the 835-1250 cm^{-1} range, high cirrus (7-10 km) had a mean emittance of 0.10 while lower cirrus (5-7 km) had a mean value of 0.58. The overall mean cirrus emittance from Platt (1973) was 0.245 in the 10-12 μm region while a study by Allen (1971) yielded a value of 0.35 for the mean emittance in the 8-13 μm region.

The relative impact (the cirrus sky surface radiance percentage of the clear sky surface radiance value) of cirrus forcing upon the surface radiance values for the 500 cm^{-1} to 2000 cm^{-1} wavenumber range was found to be larger for the Parsons mid-latitude data (110% to 195%) than for the Porto Santo subtropical data set (106% to 151%). The absolute radiance changes at the surface, on the other hand, were quite similiar for the two locations ranging from 0.87 to 8.52 $Wm^{-2}sr^{-1}$ for Parsons and 1.01 to 8.99 $Wm^{-2}sr^{-1}$ for Porto Santo.

An investigation into the impact of both mid-latitude and subtropical cirrus upon heating rates in the subcloud layer showed a linear increase with increasing cirrus emittance values. Within the cirrus cloud, there was a dramatic heating rate increase for the lowest portion of the cloud layer while the highest portion of the cloud layer showed an initial increase followed by a decrease with increasing values of emittance. It was also shown that the surface temperature and the cloud layer temperature structure play an important role in the distribution of the heating rates throughout the cirrus cloud layer. Within the subcloud layer, the Porto Santo cirrus had a larger impact upon heating rates than did the Parsons cirrus.

The derived emittances from this study were always smaller when reflectance was included in the calculation of the cirrus layer properties than they were when the reflectance was ignored. Because the parameterization of cirrus clouds emittances is considered to be important for climate modelling (Stephens 1984, Fu and Liou 1992), this could have a significant impact upon climate model output and thus have serious implications upon global climate change forcasting. The emittance of cirrus is also crucial for the determination of the net radiative effect of cirrus clouds, i.e, the "trapping" of terrestrial radiation versus the reflectance of solar radiation, which is a major concern those who study global climate change. Manabe and Strickler (1964) developed a critical blackness curve for determining whether cirrus will have a net cooling or warming effect upon the troposphere based on their emittance and pressure. They showed that although mid-latitude cirrus at all levels tend to cool, tropical cirrus between about 260 and 400 mb had the tendency to warm the troposphere below the cloud. However, this may be true to a lesser extent if cirrus cloud emittances have indeed tended to be overestimated historically.

The differences between the clear sky interferometer radiance measurements and the FASCODE III model calculations of the clear sky downwelling radiances were quite large in some cases. Because of this, a normalization of the spectra was necessary before deriving the cirrus layer radiative properties, especially for the Parsons3 case. While the normalization process was somewhat simplistic, it yielded reasonable results. The gamma adjustment from Smith (1993) is another method for finding "corrected" emittance values for cirrus cloud layers. His method relies upon FASCOD2 calculations and the resulting "corrected" emittance values are dependent upon the determination of both an effective particle size for the cirrus layer and a value for the cloud water content which are found empirically. Until there is better agreement between the measurements and model calculations, future studies of this kind could greatly benefit from a more rigorous normalization scheme.

Sounding data are necessary to initialize the model. While it takes only 2 minutes for the interferometer to acquire an interferogram that can be transformed to a spectrum, it takes more than an hour for a sonde to travel through the troposphere. Also, the interferometer views straight upward with a 2 degree field of view, while the sonde travels with the wind as far as 50 to 100 km away. "Instantaneous" soundings, from the retrieval of temperature and moisture profiles by remote sensing instruments would greatly benefit the remote sensing of cirrus.

Another caveat which is always a concern to those who study cirrus clouds, is the possibility of liquid water within the cloud layer for some of the lower cirrus cases. This can have an effect upon the slope of the derived emission in the atmospheric window as well as the magnitude.

Concerning the inclusion of reflectance in the calculations of the cirrus parameters, the derivation of a spectral emittance-reflectance relation for ice clouds could greatly enhance future studies of this sort. This would change not only the magnitude, but possibly the slope of the derived cirrus emission throughout the 8-12 μm window.

REFERENCES

Ackerman, S.A., Smith, W.L., Spinhirne, J.D. and H.E. Revercomb, 1990: The 27-28 October 1986 FIRE IFO Cirrus Case Study: Spectral Properties of Cirrus Clouds in the 8-12 μm Window. *Monthly Weather Review*, **118**, 2377-2388.

Allen, J.R., 1971: Measurements of cloud emissivity in the 8-13 μm waveband. *J. Appl. Meteor.*, **10**, 260-265.

Beck, G.H., Davis, J.M. and S.K. Cox, 1993: Spectral Emittance of Cirrus Clouds. Proceedings: FIRE Cirrus Science Results 1993, Breckenridge, Colorado, June 14-17, 1993, 214 pp.

Bretherton, F.P. and V.E. Suomi, 1983: First International Satellite Cloud Climatology Project Regional Experiment (FIRE) Research Plan, 76 pp.

Cox, S.K., 1971: Cirrus clouds and the climate. *J. Atmos. Sci.*, **28**, 1513-1515.

Cox, S.K., Beck, G., Cornwall, C., Davis, J., Hein, P., Lappen, C., Song, R., Withrow, J. and D. Wood, 1992: CSU FIRE II Cirrus Field Experiment: Description of Field Deployment Phase. Department of Atmospheric Science Paper No. 506, Colorado State University.

Feigel'son, E.M., 1970: Radiant Heat Transfer in a Cloudy Atmosphere. Israel Program for Scientific Translations, 191 pp.

Fu, Q. and K.N. Liou, 1992: Parameterization of the Radiative Properties of Cirrus Clouds. *J. Atmos. Sci.*, **50**, 2008-2025.

Griffith, K.T., S.K. Cox and R.G. Knollenberg, 1980: Infrared properties of cirrus clouds inferred from aircraft measurements. *J. Atmos. Sci.*, **37**, 1077-1087.

Hunt, G.E., 1973: Radiative properties of terrestrial clouds at visible and infra-red thermal window wavelengths. *Quart. J. R. Met. Soc.*, **99**, 346-369.

Liou, K.N., 1974: On the radiative properties of cirrus in the window region and their influence on remote sensing of the atmosphere. *J. Atmos. Sci.*, **31**, 522-532.

Manabe, S. and Strickler, 1964: Thermal equilibrium of the atmosphere with a convective adjustment. *J. Atmos. Sci.*, **21**, 361-385.

Platt, C.M.R., 1973: Lidar and radiometric observations of cirrus clouds. *J. Atmos. Sci.*, **30**, 1191-1204.

Revercomb, H.E., Buijs, H., Howell, H.B., LaPorte, D.D., Smith, W.L. and L.A. Sromovsky, 1988: Radiometric calibration of IR Fourier transform spectrometers: solution to a problem with the high-resolution interferometer sounder. *Applied Optics*, **15**, 3210-3218.

Revercomb, H.E., Smith, W.L., Sromovsky, L.A., Knuteson, R.O., Buijs, H., LaPorte, D.D. and H.B. Howell, 1989: Radiometrically accurate FTS for atmospheric emission observations. The 7th International Conference on Fourier Transform Spectroscopy, Farifax, VA, June 19-23, 1989. Society of Photo-optical Instrumentation Engineers, 1989, 70-79.

Smith, W.L., Woolf, H.M., Howell, H.B., Huang, H.L. and H.E. Revercomb, 1987: The simultaneous retrieval of atmospheric temperature and water vapor profiles - application to measurements with the high spectral resolution interferometer sounder (HIS). *RSRM 87, Advances in Remote Sensing Retrieval Methods*, Deepak 189-202.

Smith, W.L., Woolf, H.M., Howell, H.B., Revercomb, H.E. and H.L. Huang, 1988: High Resolution Interferometer Sounder - The Retrieval of Atmospheric Temperature and Water Vapor Profiles. 3rd Conference on Satellite Meteorology and Oceanography, Anaheim, California, February 1-5, 1988.

Smith, W.L., Ma, X.L., Ackerman, S.A., Revercomb, H.E. and R.O. Knuteson, 1993: Remote Sensing Cloud Properties from High Spectral Resolution Infrared Observations. *J. Atmos. Sci.*, **50**, 1708-1720.

Stephens, G.L. and P.J. Webster, 1979: Sensitivity of radiative forcing to variable cloud and moisture. *J. Atmos. Sci.*, **36**, 1542-1556.

Stephens, G.L., 1980: Radiative Properties of Cirrus Clouds in the Infrared Region. *J. Atmos. Sci.*, **37**, 435-446.

Stephens, G.L., 1984: The Parameterization of Radiation for Numerical Weather Prediction and Climate Models. *Monthly Weather Review*, **112**, 826-867.

Wallace, J.M. and P.V. Hobbs, 1977: Atmospheric Science: An Introductory Survey. *Academic Press*, 467 pgs.

Yamamoto, G., Tanaka, M. and S. Asano, 1970: Radiative Transfer in water clouds in the infrared region. *Journal of the Atmospheric Sciences*, **27**, 282-292.

APPENDIX A

INSTRUMENTATION

A.1. Description of Infrared Interferometer

The instrument used for this study was a dual port emission interferometer manufactured by Bomem, Inc. It has an adjustable resolution which ranges from 1 cm^{-1} to 128 cm^{-1}. All of the FIRE data used for this study were taken with the interferometer at the 1 cm^{-1} resolution setting. The interferometer's MCT (mercury cadmium telluride) detector has a useful range from 500 cm^{-1} to 2000 cm^{-1}. The detector was liquid nitrogen cooled during the acquisition of the data in Parsons, Kansas and was cryogenically cooled during the Porto Santo field deployment phase. The instrument has a 2 degree field of view.

Facing the target port of the interferometer is a rotatable gold-plated mirror mounted at a 45 degree angle with respect to the axis of the entering optical path. The position of this mirror is maintained by a computer controlled DC servo motor and control circuit. Mounted on the side and sitting underneath the mirror are two blackbody sources which are necessary for the calibration procedure that is described in the next section. The rotatable mirror enables the interferometer to sequentially view the two blackbody sources and to scan the atmosphere at various user-specified zenith angles.

Attached directly outside the second interferometer port is a reference blackbody protected by a desiccant container. The reference blackbody is a grooved copper disk which is coated to improve the emissivity. It is thermoelectrically-heated and its temperature is monitored by a small thermocouple which is located within ten one-thousandths of an inch beneath the surface of the coated side. The temperature of the reference blackbody is maintained to within 0.1 C by a simple toggling and monitoring control loop circuit on the thermoelectric element.

The interferometer receives radiation from the atmosphere following reflection from the rotatable gold-plated mirror. Both the atmospheric emission and the reference blackbody beams enter a Michelson interferometer through KBr (thallium bromide) windows in their respective ports. The atmospheric beam experiences an even number of reflections in the Michelson interferometer while the beam from the reference blackbody experiences an odd number of reflections. As a consequence, these two beams are 180 degrees out of phase when they reach the detector. This results in the generation of a difference interferogram between the target and the reference blackbody. This interferogram represents the raw data product from the interferometer. The following sections describe the steps taken to convert the raw interferogram into useful spectral data.

A.2. Blackbody Sources

Two blackbody sources are used to calibrate the interferometer. One is a warm blackbody source and the other is a cold blackbody source because it is preferable that the two sources bracket the emission temperature of the atmospheric signal. The cold blackbody source located beneath the rotatable mirror is a dewer of liquid nitrogen which is known to be at 77 Kelvin. The warm blackbody source mounted to the side is a cylindrical copper cavity which is at the ambient air temperature. This copper blackbody is 7 inches long, has an outside diameter of 3 inches and an inside diameter of about 1 1/2 inches. Its large thermal mass prevents it from having rapid changes in temperature. There are two small thermocouples located near the inner walls of the copper blackbody used to monitor its temperature. The blackbody cavity is grooved and coated to insure a high emittance. Interferograms representing the emission at each wavenumber from each of the two blackbody sources are collected for use in the calibration of the instrument.

The mirror position, and thus the target viewed by the interferometer, is controlled by PC software. During the Parsons, Kansas field deployment and during the first part of the Porto Santo field deployment, the interferometer viewed the liquid nitrogen followed by the copper blackbody and then the atmosphere in sequence. For the latter part of the Porto Santo field deployment, this sequence was reversed so that the interferometer viewed the atmosphere at the beginning of the scan sequence. This is advantageous because it allows for better coordinated observation of sky cover and radiometrical data. Before this reversal, when the interferometer viewed the atmosphere at the end of the sequence, there was more time for a stray low level cloud to travel across the field of view of the instrument or for the cirrus thickness to change dramatically. Both of these types of events occurred during the acquisition of the data sets used for this study.

A.3. Data Collection and Storage

One complete data collection cycle consists of sequentially viewing the two blackbody sources and the atmosphere. In the FIRE experiment each cycle typically consisted of 20 scans of the movable mirror in the Michelson interferometer for each target. The sets of 20 scans are then co-added to reduce the noise of the measurement. This yields three interferograms. The temperatures of the reference blackbody, the warm and the cold blackbody sources, and the ambient air were measured every 0.2 seconds. Every 100 temperature measurements were averaged and then recorded at 20 second intervals on a CR21X Campbell datalogger. Each cycle took slightly less than two minutes to complete, resulting in five temperature readings per interferogram. The temperature data were then downloaded to the PC which operates the interferometer to form a merged data set.

A.4. Calibration Procedure

Inside the Michelson interferometer, there is a stationary mirror and a movable mirror that scans back and forth. If the scanning mirror is moved at a constant velocity, the signal at the detector will vary sinusoidally. Whenever the two beams are in phase with each other there will be a maximum in the interferogram. Therefore, one can obtain a spectrum from an interferogram by employing one-half of a cosine Fourier transform pair that may be written as follows:

$$F(x) = \frac{1}{2}\int_{-\infty}^{\infty} C_\nu \exp[i\phi(\nu)]\exp[i2\pi\nu x]\,d\nu . \tag{A.1}$$

The uncalibrated magnitude spectrum for a given target in terms of radiances may be written as:

$$C_\nu = |\tilde{F}| = r_\nu(L_\nu + L_\nu^o) , \tag{A.2}$$

where $|\tilde{F}|$ is the complex Fourier transform, r_ν is the responsivity of the instrument, L_ν is the spectral emission and L_ν^o is the emission offset of the instrument. This equation states that there is a linear relationship between the uncalibrated spectrum (C_ν) and the spectral emission.

The offset and the response of the detector are two unknowns that are derived from the calibration procedure which involves observing the cold and hot blackbody sources. The responsivity may be written as:

$$r_\nu = \frac{(C_{h\nu} - C_{c\nu})}{[B_\nu(T_h) - B_\nu(T_c)]} , \tag{A.3}$$

where $(C_{h\nu}-C_{c\nu})$ represents the difference between the uncalibrated spectra of the hot and cold blackbodies respectively and $[B_\nu(T_h)-B_\nu(T_c)]$ the difference between their Planck functions. Recall that the interferograms are actually difference interferograms and so the first term on the right-hand side could be fully written as $[(C_{h\nu}-C_{r\nu})-(C_{c\nu}-C_{r\nu})]$ where $C_{r\nu}$ would represent the spectra from the reference blackbody source in the secondary port. However, for this set of equations the terms $C_{h\nu}$ and $C_{c\nu}$ will represent the uncalibrated spectra derived from the difference interferograms. The offset required may be found with the following relation:

$$L_\nu^o = \left(\frac{C_{h\nu}}{r_\nu}\right) - B_\nu(T_h)\,. \tag{A.4}$$

Now, with the known detector response (r_ν) and offset (L_ν^o) required, the atmospheric emission can be found by re-arranging equation (1.2) and may be written as:

$$L_\nu = \left(\frac{C_\nu}{r_\nu}\right) - L_\nu^o\,. \tag{A.5}$$

Laboratory tests comparing the observed cavity blackbody spectra to the correlating theoretical Planck function curve have shown that the calibration of the interferometer is within 2% for the useful range of the detector.

APPENDIX B

DETAILED SEMI-EMPIRICAL TECHNIQUE

The first iterative set determines values for both the transmittance and the effective Planck radiance of the cirrus cloud layer. After convergence, the effective Planck radiance for the cirrus layer is passed from the first iterative set to the second and is used to determine the emittance and reflectance which is found by the second iterative equation set. After the solutions for the second set converge, the reflectance is then passed from the second iterative set back to the first where new values for the transmittance and effective Planck radiance are determined once again. The new value of the effective Planck radiance is passed back to the second iterative set, and this process of passing information between iterative sets continues until the change in the value of the effective Planck radiance becomes very small.

The transmittance of the cirrus cloud layer may be written as:

$$T_{cld} = 1 - R_{cld} - E_{cld}, \tag{B.1}$$

where T_{cld} is the transmittance, R_{cld} is the reflectance and E_{cld} is the emittance. Using the relation $N_{cld}=E_{cld}B_{cld}$, equation (2.18) can rewritten as:

$$T_{cld} = 1 - R_{cld} - \frac{N_{cld}}{B_{cld}}. \tag{B.2}$$

By rearranging equation (A.7) and then substituting for N_{cld} we obtain:

$$T_{cld} = 1 - R_{cld} - \frac{(N_{cldlayer} - F_{cld})}{B_{cld}}. \tag{B.3}$$

And by rearranging equation (2.12) and substituting for $N_{cldlayer}$ in the previous equation yields:

$$T_{cld} = 1 - R_{cld} - \frac{\left(\frac{N_{meascld} - N_{adjmeasclr}}{T_1}\right) - F_{cld}}{B_{cld}}. \tag{B.4}$$

This is the equation which is used to determine the transmittance of the cirrus cloud layer (T_{cld}) in the first of the two nested iterative sets.

Assuming that the emission is linear in optical depth throughout the layer, the integrated Planck radiance for the cirrus layer is stated as follows:

$$\int_{cldtop}^{cldbase} B_{cld}(z) \frac{dT}{dz} dz = B_{cldbase} - B_{cldtop} T_{cld} + \frac{(T_{cld} - 1)(B_{cldtop} - B_{cldbase})}{\ln T_{cld}}. \tag{B.5}$$

$B_{cldbase}$ and B_{cldtop} are the Planck functions for the cloudbase and cloudtop temperatures, respectively. Using the mean value theorem, a mean Planck radiance for the cirrus layer may be found:

$$B_{cld} = \frac{\int_{cldtop}^{cldbase} B_{cld}(z)\,\frac{dT}{dz}\,dz}{(1 - T_{cld})}\,. \tag{B.6}$$

The inference of the effective Planck radiance for the cirrus cloud layer, B_{cld}, is necessary for the second iterative set. The second set yields the emittance of the cirrus cloud layer, the reflectance of the cirrus cloud layer, the magnitude of the radiance emitted by the cirrus cloud and the magnitude of the surface and sub-cloud radiance that is reflected by the cirrus cloud. The radiance which is emitted by the cirrus layer is found by equation (A.7) which is restated here for convenience:

$$N_{cld} = N_{cldlayer} - F_{cld}\,. \tag{B.7}$$

The emittance of the cirrus cloud layer is fairly straightforward and is given in the following equation:

$$E_{cld} = \frac{N_{cld}}{B_{cld}}\,. \tag{B.8}$$

The reflectance of the cirrus cloud layer is based on an emittance-reflectance relation that is found in Yamamoto (1970). Unfortunately, the relation is for water clouds; however, a literature search has not resulted in information of this type for ice clouds. In a study by Hunt (1973), the reflectance for ice clouds was found to be about 1.75 times the reflectance for water clouds at 11 microns. The relationship between the emittance and the reflectance is a nearly second-order type of relation. A plot of the ratio of the emittance to the reflectance versus the emittance yields a nearly straight line for each wavenumber; each wavenumber has its own slope and y-intercept. Figure B.1 shows the reflectivity values across the atmospheric window associated with emittances ranging from 0.1 to 0.8.

R_{cld} is the unknown in this equation and so in the iterative equation set it is written as:

$$R_{cld} = \frac{E_{cld}}{m\,E_{cld} + b}\,. \tag{B.9}$$

Where the values for *m* and *b* are spectrally dependant. The radiance emitted from the sub-cirrus layer and surface that is reflected by the cirrus cloud layer as seen from the bottom of the cloud layer looking upward is found by equation (B.10).

$$F_{cld} = R_{cld}\,N_{adjupwardl} \tag{B.10}$$

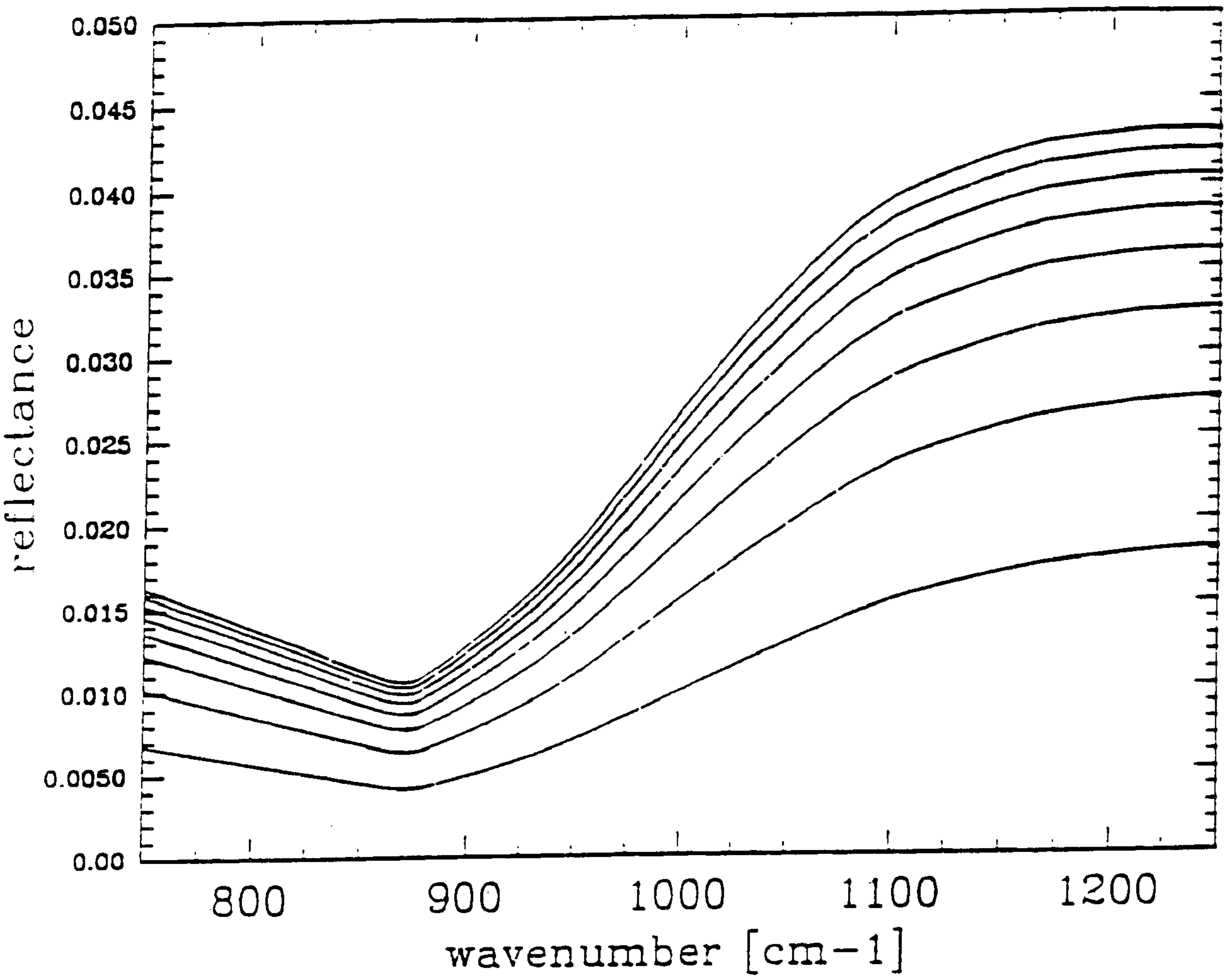

Figure B.1. Reflectance relation to emittance in ascending order from bottom to top for emittances between 0.1 and 0.8 in increments of 0.1.

APPENDIX C

DATA TABLES

All of the results presented here are derived from spectral radiance measurements in the 760 cm^{-1} to 1240 cm^{-1} wavenumber range and all of the listed radiances have units of [Wm^{-2}sr^{-1}]. Table C.1 shows the conditions for the data used in this study. Given are the case location and assigned number, the spectrum date and time, the vertical extent of the cirrus layer (km), the cloudbase and effective cloud layer emission temperatures (K), the lapse rate for the cirrus layer (K km^{-1}), the surface temperature (K) and the atmospheric precipitable water content (cm). Table C.2 shows integrated cirrus layer emittances, transmittances and reflectances (as seen at the bottom of the cirrus layer). Table C.3 shows integrated values for emitted radiances and reflected radiances and also it also lists the percentage of reflected radiance to the total radiance emerging from the cirrus layer.

		$Z_{cldlayer}$	$T_{cldbase}$	T_{cldeff}	$\gamma_{cldlayer}$	T_{sfc}	$H_2O_{precipitable}$
Parsons1 - 11/21/91							
#90 clear	2110Z						1.01
#06 sparse ci	2250Z	9.0-10.0	232	228	8.2	286	1.12
#30 sparse ci	2250Z	9.0-10.0	232	228	8.2	286	1.12
#48 thin ci	0215Z	8.0-10.0	240	232	8.4	283	1.08
#60 thin ci	0215Z	8.0-10.0	240	232	8.4	283	1.08
Parsons2 - 11/26/91							
#12 clear	1600Z						1.21
#42 cirrus	1800Z	9.0-10.0	226	222	9.1	285	1.30
#60 cirrus	1900Z	8.0-10.0	234	227	8.8	285	1.30
#75 ci cu	2000Z	6.5-10.0	245	234	8.2	286	1.43
#90 thick ci	2030Z	5.5-9.8	254	240	8.4	286	1.43
#06 thick ci	2140Z	5.8-9.0	251	243	8.2	286	1.43
Parsons3 - 12/5-6/91							
#51 cirrus	1708Z	11.0-12.0	220	217	8.0	282	1.11
#75 cirrus	1932Z	10.0-12.0	227	220	7.6	284	1.18
#93 cirrus	2113Z	9.6-12.2	230	221	7.9	284	1.11
#09 mult-layer	0114Z	8.5-12.0	237	226	7.4	277	1.18
#33 2-layer ci	0758Z	7.2-9.4	247	241	5.4	273	1.14
#45 faint ci	0930Z	@9.0	236	236	-	274	1.10
#30 clear	1956Z						1.68
Portsan1 - 6/10-11/92							
#03 cirrus	0853Z	9.7-10.0	234	233	8.7	290	2.06
#06 mod-thn ci	0859Z	10.5-11.0	226	224	9.8	290	2.06
#15 cirrus	0921Z	9.3-10.0	236	234	8.7	290	2.06
#18 cirrus	0921Z	9.3-10.0	236	234	8.7	290	2.06
#33 cirrus	1245Z	7.5-9.0	250	245	7.2	293	2.24
#06 clear	1120Z						1.99
Portsan2 - 6/23/92							
#39 thick ci	1250Z	6.0-9.0	257	252	7.0	290	2.10
#45 thick ci	1307Z	6.0-8.0	257	252	6.3	290	2.10
#75 thning ci	1642Z	8.0-8.3	243	242	7.3	292	1.94
#84 clear	2046Z						2.00
Portsan3 - 6/27/92							
#27 thin ci	1306Z	6.8-7.2	258	257	6.5	295	3.36
#33 thick ci	1330Z	7.0-9.5	257	251	7.8	295	3.36
#45 mod ci	1356Z	7.5-9.5	253	247	8.0	295	3.36
#51 clear	1418Z						3.36

Table C.1. Basic parameters for all of the cirrus events that were considered for this study.

		emit	tran	refl
Parsons1	#06	.006	.994	.001
	#30	.015	.985	.001
	#48	.078	.916	.007
	#60	.072	.922	.007
Parsons2	#42	.032	.968	.002
	#60	.380	.601	.019
	#75	.406	.574	.020
	#90	.342	.639	.018
	#06	.749	.227	.024
Parsons3	#51	.092	.909	.005
	#75	.120	.884	.009
	#93	.236	.749	.014
	#09	.068	.922	.006
	#33	.112	.879	.009
	#45	.027	.970	.002
Portsan1	#03	.139	.859	.009
	#06	.029	.967	.002
	#15	.050	.949	.003
	#18	.106	.892	.007
	#33	.648	.330	.023
Portsan2	#39	.926	.058	.026
	#45	.665	.312	.024
	#75	.095	.895	.010
Portsan3	#27	.041	.954	.005
	#33	.821	.157	.025
	#45	.466	.514	.021

Table C.2. Fractional emittances, transmittances and reflectances corresponding to the data listed in Table C.1.

		emit	refl	reflrad%
Parsons1	#06	.05	.02	.332
	#30	.14	.05	.315
	#48	.88	.30	.258
	#60	.82	.28	.263
Parsons2	#42	.27	.10	.291
	#60	3.79	.75	.162
	#75	4.68	.78	.141
	#90	4.59	.73	.135
	#06	10.44	.96	.082
Parsons3	#51	.66	.24	.285
	#75	.99	.36	.302
	#93	2.05	.64	.232
	#09	.67	.25	.270
	#33	1.58	.34	.173
	#45	.37	.11	.221
Portsan1	#03	1.61	.54	.264
	#06	.28	.14	.328
	#15	.62	.21	.268
	#18	1.26	.41	.261
	#33	9.72	1.32	.117
Portsan2	#39	16.04	1.33	.075
	#45	11.48	1.22	.094
	#75	1.27	.50	.284
Portsan3	#27	.68	.22	.245
	#33	13.93	1.21	.078
	#45	7.27	1.02	.121

Table C.3. Values of the emitted radiance, reflected radiance and the reflected radiance fraction of the total radiance corresponding to the data listed in Table C.1.

'45